SANDIA REPORT
SAND2019-12890
Printed September 2019

Sandia National Laboratories

Benchmarking 3D-MHD simulations of electrothermal instability growth by studying z-pinches with engineered defects

Thomas J. Awe, Edmund P. Yu, Trevor M. Hutchinson, Bruno S. Bauer, K. Tomlinson, Brian T. Hutsel, Gabriel A. Shipley, Jamin R. Pillars, Deanna M. Jaramillo, Diego J. Lucero, William D. Tatum, Bonnie B. McKenzie, W. Graham Yelton, Maren W. Hatch, David Benney, David A. Yager-Elorriaga, Aidan W. Klemmer, Mark A. Gilmore, Adam J. York, Derek C. Lamppa, Larry M. Lucero

Prepared by
Sandia National Laboratories
Albuquerque, New Mexico
87185 and Livermore,
California 94550

Issued by Sandia National Laboratories, operated for the United States Department of Energy by National Technology & Engineering Solutions of Sandia, LLC.

Available to DOE and DOE contractors from
U.S. Department of Energy
Office of Scientific and Technical Information
P.O. Box 62
Oak Ridge, TN 37831

Telephone: (865) 576-8401
Facsimile: (865) 576-5728
E-Mail: reports@osti.gov
Online ordering: http://www.osti.gov/scitech

Available to the public from
U.S. Department of Commerce
National Technical Information Service
5301 Shawnee Rd
Alexandria, VA 22312

Telephone: (800) 553-6847
Facsimile: (703) 605-6900
E-Mail: orders@ntis.gov
Online order: https://classic.ntis.gov/help/order-methods/

ABSTRACT

The electrothermal instability (ETI) is driven by Joule heating and arises from the dependence of resistivity on temperature. ETI may drive azimuthally correlated surface density variations which seed magneto Rayleigh-Taylor (MRT) instability growth. Liner implosion studies suggest that dielectric surface coatings reduce the amplitude of ETI driven perturbations. Furthermore, previous fundamental physics studies suggest that non-metallic inclusions within the metal can seed ETI growth. In this project, we aimed to (1) determine how dielectric coatings modify ETI growth by varying the coating thickness and the surface structure of the underlying metal, and (2) study overheating from engineered defects—designed lattices of micron-scale pits. Engineered pits divert current density and drive local overheating in a way that can be compared with 3D-MHD simulations. All experiments were executed on the Sandia Mykonos Facility. Facility and diagnostic investments enabled high quality data to be gathered in support of project deliverables.

ACKNOWLEDGEMENTS

Supported in part by the LDRD Program at Sandia National Laboratories (Projects 178661/200269). Sandia National Laboratories is a multi-mission laboratory managed and operated by National Technology and Engineering Solutions of Sandia, LLC., a wholly owned subsidiary of Honeywell International, Inc., for the U.S. Department of Energy's National Nuclear Security Administration under Contract No. DE-NA-0003525.

CONTENTS

LIST OF FIGURES

LIST OF TABLES

This page left blank

ACRONYMS AND DEFINITIONS

Abbreviation	Definition
ETI	electrothermal instability
ICCD	intensified charge coupled device
ICF	inertial confinement fusion
LCA	laser control area
LDRD	laboratory directed research and development
LOS	Line of sight
MDI	magnetically driven implosion
MHD	magnetohydrodynamic
MITL	magnetically insulated transmission line
MRT	magneto Rayleigh-Taylor
METI	Mykonos electrothermal instability—Campaign name
PDV	photonic Doppler velocimetry
STS	slow tool servo
SVS	streaked visible spectroscopy

1. INTRODUCTION

The magneto-Rayleigh-Taylor (MRT) instability [i,ii] generates implosion asymmetries that limit the performance of the magnetically accelerated z-pinch liners (tubes) used to compress high-energy-density plasmas for inertial confinement fusion (ICF) studies [iii,iv,v,vi,vii]. Azimuthally correlated liner-surface roughness (generated by lathe-based machining) was considered the dominant seed for MRT, and techniques were developed to minimize this surface perturbation. However, implosion studies on the Z Facility showed that liners with 10-30 nm initial roughness develop MRT which is both more azimuthally correlated and of larger amplitude than expected [viii,ix,x]. Computational studies showed that an azimuthally-correlated electrothermal instability (ETI) may grow on the liner's surface early in the current pulse to an amplitude of several microns [xi,xii] (~100X the initial roughness). ETI is driven by Joule heating and arises from the dependence of electrical resistivity (η) on temperature (T) [xiii,xiv,xv,xvi,xvii,xviii,xix,xx]. Prior to plasma formation metals with $\partial\eta/\partial T>0$ are expected to form hot and cold bands, or azimuthally correlated "strata." After plasma forms, $\partial\eta/\partial T<0$, and axially oriented overheated "filaments" are expected. Simulations suggest that after a condensed metal ($\partial\eta/\partial T>0$) melts and loses strength, temperature and pressure variations drive expansion along strata, providing a relatively large amplitude seed for MRT growth.

The fundamental equation governing linear ETI growth is given in (1). Here, γ is the linear growth rate, ρ is mass density, p is the pressure, η is electrical resistivity, c_v is specific heat capacity, κ is thermal conductivity, k_z is the axial wavenumber, T is temperature, and T* is a material specific temperature that depends on pressure and density through a simplified equation of state (uniform current density is assumed).

$$\gamma = \frac{j^2 \frac{\partial \eta}{\partial T} + \frac{\rho}{T^*}\left(c_v \frac{\partial T}{\partial t} - j^2 \frac{\partial \eta}{\partial \rho}\right) - k_z^2 \kappa}{\rho c_v + \frac{p}{T^*}} \qquad (1)$$

When ohmically heated, condensed metal (solid, liquid, vapor) is destabilized by the effects of increasing resistivity with temperature, (1st term), material heating (2nd term), and increased resistivity with decreased density (3rd term). Thermal conduction stabilizes short wavelengths modes (4th term). In general, prior to plasma formation, the striation form of ETI (**k** in z-direction) grows rapidly with decreasing density and increasing temperature.

Within the Z-ICF program, an effort was initiated to understand, and ideally mitigate the growth of ETI perturbations. Simulations by Peterson et al. [xxi] showed that the amplitude of the ETI perturbation on the liner's outer surface may be limited by the addition of a dielectric coating which serves as an ablation tamper. The presence of the tamper reduces ETI growth associated with non-uniform expansion of the liner's outer boundary, and the seed amplitude for subsequent MRT growth is reduced.

Z experiments demonstrated the dramatic stabilizing effect of dielectric coatings when applied to rapidly-accelerated magnetically-driven rods and imploding liners. For Al-liner experiments, due to Al's relatively high opacity, the Al-dielectric interface remains obvious in radiographs, allowing straightforward evaluation of the metal's outer surface; a 10X reduction of cumulative MRT growth is demonstrated when compared to MRT growth from uncoated, but otherwise similar

liners. For Be-liner experiments, due to the comparable opacity of Be and Epon, locating the Be-dielectric interface is challenging. However, the low opacity of the Be enables characterization of the instability structure, and diagnosis of the liner's inner wall. Data from these experiments are shown in Figs. 1-1 and 1-2, and demonstrate the dramatic stabilizing effect of dielectric coatings, which were designed to mitigate ETI growth.

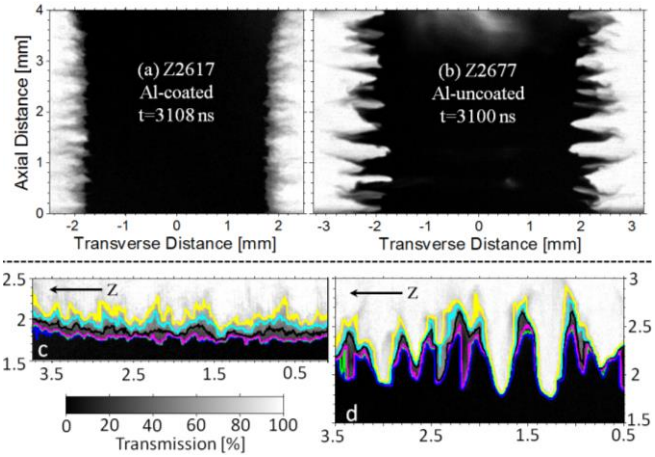

Figure 1-1. Figure (above) and caption (below) copied from [T.J. Awe, *et al*., PRL, 2016]

Figure 2. Radiographs of AR=8.94 Al liners ($R_{in,0}$=3.082 mm, and $R_{out,0}$=3.47 mm). (a) Dielectric coated. (b) Uncoated. (c), and (d) Transmission contours of the right-hand side surfaces of the radiographs in (a) and (b), respectively. Transmission contours are (percentage–color): (10%–blue), (15%–green), (20%–magenta), (40%–black), (60%–cyan), and (80%–yellow). The grayscale applies to (a-d).

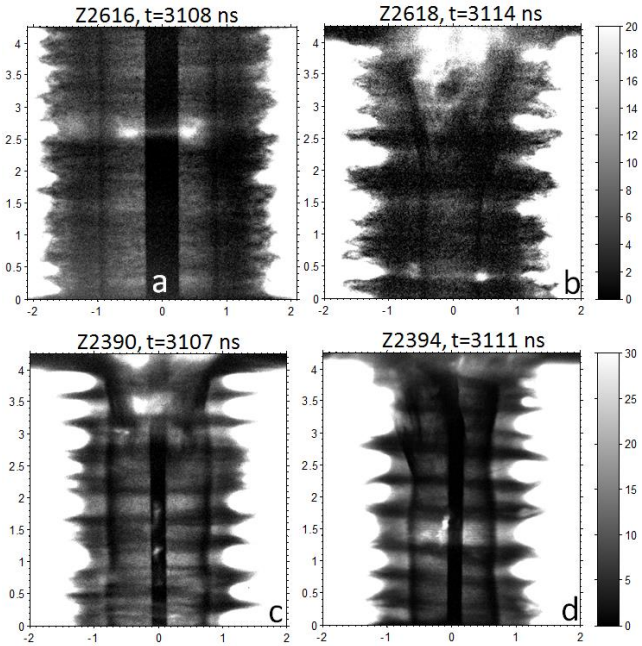

Figure 1-2. Figure (above) and caption (below) copied from [T.J. Awe, *et al*., PRL, 2016]
Figure 3. Radiographs of imploding Be liners with AR=6, $R_{in,0}$=2.89 mm, and $R_{out,0}$=3.47 mm. Axes in [mm]. Transmission scales in [%]. (a)-(b) Dielectric coated. (c)-(d) Uncoated liner experiments previously reported in [20]. Rods are placed on axis in select experiments (black vertical strips in the center of radiographs a, c, and d) to limit the time-integrated self-emission that is sometimes generated at stagnation, and can obscure radiographs. To accentuate the high-opacity coatings on the liner's inner wall, the grayscale ranges were limited to 0-30% transmission in (a), (c), and (d) (0%=black, 30%=white), and 0-20% transmission in (b). Therefore, much of the Be and Epon mass in the limb regions of the radiographs has been omitted in this representation of the data.

While the simulations and experiments in support of the Z ICF program discussed above give credence to the hypothesis that ETI seeds MRT, direct observations of ETI had not yet been made. A direct observation of ETI was vital to ensure our simulation tools are accurately representing the seed of the MRT instability. Addressing the outstanding and important fundamental physics questions surrounding ETI initiation and evolution was the goal of a Late Start LDRD (Project 178661, FY14-15).

The emphasis of Late Start LDRD Project 178661, entitled "Direct observation of electrothermal instability structures in the skin layer of an intensely Ohmically heated conductor" was to directly observe variations in the intensity of self-emission from a thick z-pinch's metal surface. These data would be analyzed to determine whether the observed non-uniformities were a result of ETI. Experiments were designed to directly measure overheating structures formed on Ohmically heated thick conductors using a high resolution, high sensitivity, near-IR/visible framing camera. Prerequisite experimental conditions included the fabrication of extremely smooth targets with well-characterized metallic structure and surface preparation in order to differentiate physical mechanisms that may drive ETI (e.g. non-metallic inclusions and/or machining imperfections), load hardware that avoided high-voltage breakdown phenomena (that would create non-thermal plasmas which would preclude the possibility of observing the low-level emission associated with

ETI), and a high spatial and temporal resolution gated imaging system capable of observing small-scale and low-emission overheat structures on the metal's surface.

In experiments executed on the University of Nevada, Reno Zebra Facility, non-uniform Ohmic heating was directly observed from 1.0-mm-diameter solid aluminum rods pulsed to 1 MA in 100 ns. Bare and dielectric coated rods were studied, and two important observations were made for the two classes of loads. First, for dielectric coated rods, the first direct observation of the stratified electrothermal instability on the surface of thick metal was made. Aluminum rods were coated with 70 μm Parylene-N, and the dielectric coating suppressed plasma formation, enabling persistent observation of discrete azimuthally correlated stratified thermal perturbations perpendicular to the current. Wave numbers, k, were observed to grow exponentially with rate $\gamma(k) = 0.06\ \mathrm{ns}^{-1} - (0.4\ \mathrm{ns}^{-1}\ \mu\mathrm{m2}\ \mathrm{rad}^{-2})\ k^2$ in ~1 g/cm3, ~7000 K aluminum [xxii]. Second, for uncoated rods, we observed for the first time the evolution from discrete, micron-scale temperature inhomogeneity, to global (>100 micron scale) overheated strata on a thick metal z-pinch [xxiii]. Al 6061 was studied, and this alloy contains distributed micron-scale resistive inclusions (similar inclusions exist in the S65 beryllium liners used for MagLIF and other experiments on Z, which motivated the study of Al 6061). Data suggest that the inclusions were a likely seed for the local overheating as supported by comparing the surface density of micron scale resistive inclusions to the surface density of hot spots observed in experimental ICCD images.

The compelling observations made in the late start LDRD facilitated support of a follow on LDRD, the results of which are reported here. This LDRD, emphasized two areas of study. First, we studied loads with prescribed and deliberately machined engineered defects. Second, we executed a scan of loads with varying dielectric coating thickness, and varied machining structure on the underlying metal.

Engineered defect studies

To unravel the physics of ETI and other Joule-heating driven instabilities, experiments were designed to provide data that can be directly compared with simulation. We executed a plan that will greatly enhance our ability to interpret experimental results by employing the following innovative practices: (1) We used state of the art simulation tools (primarily 3D ALEGRA [xxiv]) to design z-pinch rods with engineered defect lattices to test various hypotheses on ETI evolution. (2) We developed a novel method for fabricating targets with engineered defects. Rod surfaces are diamond turned to extreme smoothness, and then further machined to include carefully characterized "engineered" defects—designed lattices of micron-scale pits in patterns informed by detailed simulation. Highly reproducible pit fabrication has been achieved using a 5-axis diamond turning lathe in slow tool servo mode. Engineered pits will divert current density and drive local overheating. Defects are thoroughly and precisely characterized so that actual defect parameters can be used in simulations. (3) We advanced our world class diagnostic capability to add imaging frames to provide data of unmatched precision, reliability, and completeness, for benchmarking simulation and theory.

Dielectric coating parameter scan

Coated rods were acknowledged as a suitable platform for future ETI studies, primarily because of the extended observation window afforded by the coating's tendency to suppress plasma formation. In this LDRD, we pursued a variety of open questions, including:

1. How does the wavelength and amplitude of ETI grow with time?
2. Does the initial surface perturbation from machining influence ETI evolution?
3. How does the coating thickness impact the evolution of ETI?
4. How does the coating thickness impact the expansion velocity of the metallic surface?
5. How does the coating thickness impact plasma formation?

In this report, we provide a detailed overview of ETI-relevant experiments executed on the Mykonos Facility. We first discuss infrastructure improvements made to the Mykonos Facility to enable detailed studies of ETI physics. Topics include facility investments (e.g., a laser safety enclosure, a new vacuum chamber, new powerflow hardware, etc.), diagnostic development activities, and the addition of a cryogenic cooling capability. We then discuss physics results, first addressing those experiments designed to study the impact of varying dielectric surface coatings on ETI evolution, followed by an overview of engineered defect research. The engineered defect section will discuss both modeling efforts, and initial experiments.

2. ANALYSIS OF PREVIOUS ZEBRA DATA

LDRD 200269 leveraged promising results from an earlier late-start LDRD (Project 178661), entitled "Direct observation of electrothermal instability structures in the skin layer of an intensely Ohmically heated conductor." Select data from the Late Start LDRD had not yet been properly analyzed or published. In year 1 of the follow-on LDRD, much effort was required to build the requisite infrastructure in the Mykonos Facility to support ETI experiments. During that time, in parallel, significant effort was put into analyzing the existing Zebra-Facility dataset. This resulted in 2 separate publications. Here, we provide a high-level overview of each publication, and provide a reference to the peer-reviewed articles that are now available in the literature.

Paper 1 citation:

T. J. Awe, E. P. Yu, K. C. Yates, W. G. Yelton, B. S. Bauer, T. M. Hutchinson, S. Fuelling, and B. B. Mckenzie. *On the Evolution from Micrometer-Scale Inhomogeneity to Global Overheated Structure During the Intense Joule Heating of a z-Pinch Rod*. IEEE Trans. Plasma Sci., **45**, 584 (2017).

Overview:

A two-frame ultrafast optical microscopy system with 3-micron-spatial and 2-ns-temporal resolution was used to image the surface of metallic rods pulsed with extreme current to generate megagauss level surface magnetic fields. Non-uniform emissions were observed as the metallic surface melted, vaporized and transitioned to plasma (Fig. 2-1). Earliest observed emissions were in the form of discrete, ~10-micron-scale sub-eV spots. Experiments studying 6061 alloy aluminum were studied in great detail. Al-6061 contains volumetrically distributed micron-scale nonmetallic resistive inclusions, and it was shown that the number density (per mm surface area) of micron scale inclusions (as determined by pre-shot SEM images) was well matched to the number density of self-emission spots. For high purity 5N aluminum, the number of self emission spots was greatly reduced. Furthermore, for 6061 Al, the spots evolved as the surface was further heated; the spots were observed to stretch azimuthally, and eventually connect to form elongated stratified structures, supporting select hypotheses regarding electrothermal instability formation and evolution. This work provided the motivation for future experiments studying targets with engineered defects, as the extreme complexity of the inherent inhomogeneity of the Al 6061 rods made it difficult to make definitive conclusions regarding what was fundamentally seeding the observed heating nonuniformity.

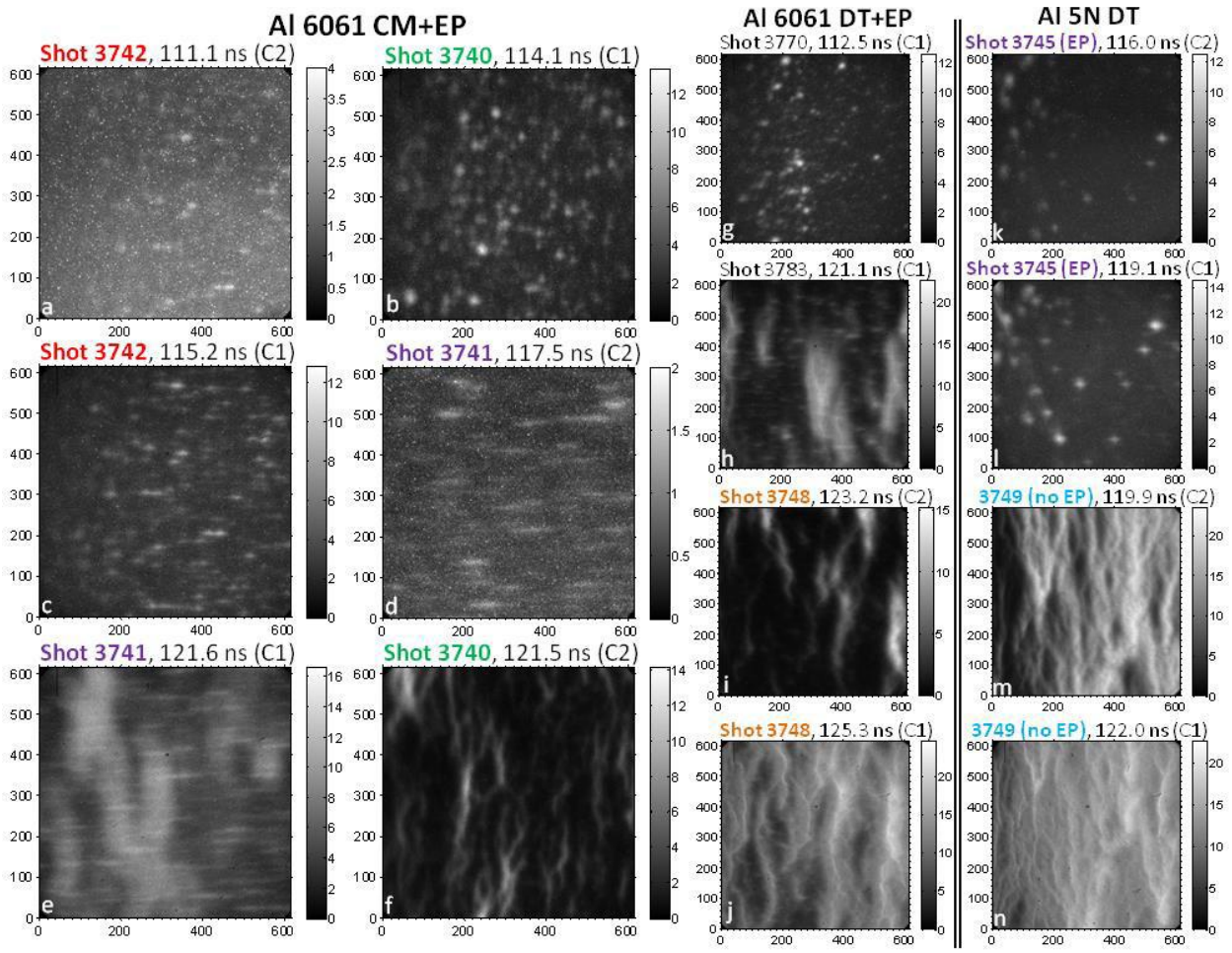

Figure 2-1. Self emission from barbell surfaces for different alloys and preparation.

Paper 2 citation:

T. M. Hutchinson, T. J. Awe, B. S. Bauer, K. C. Yates, E. P. Yu, W. G. Yelton, and S. Fuelling. *Experimental observation of the stratified electrothermal instability on aluminum with thickness greater than a skin depth*. Phys. Rev. E **97**, 053208 (2018).

Overview:

The experimental work was inspired by rod [xxv] and liner [xxvi] studies on Z, showing a reduction magneto-Rayleigh Taylor instability (MRT) amplitudes on coated metal. This reduction is attributed to the coating's inertial tamping of the low-density matter that admits the largest electrothermal instability (ETI) growth rate. Reduced time-integrated ETI growth means the density perturbations which form the initial conditions for the MRT instability are smaller, and therefore at any time are smaller than they would be without coatings.

To study the early evolution of ETI, 70 μm of a Parylene-N, a transparent dielectric, was deposited on 1-mm-diameter metal rods which were then pulsed with 1 MA of current in 100 ns. Using intensified charge coupled devices (ICCD), ultra-high temporal ($2-3$ ns) and spatial (3 μm) resolution images were captured. Absolute calibration of the ICCD images required

understanding the spectral response of every optical element in each camera's path. This can be understood with the following equation:

$$R(\lambda,T) = SR(\lambda,T) \cdot\ P(\lambda) \cdot\ N_f(\lambda) \cdot Q_E(\lambda) \cdot\ S_A\ \cdot E_A\ \cdot r \cdot g_a \cdot g_t \cdot p_t \cdot O_{ldm}(\lambda) \cdot N_B(\lambda)/P_n$$

where λ is wavelength (in nm) , $SR(\lambda,T)$ is the Planckian spectral radiance of a blackbody, given in $\mathrm{W}/(\mathrm{m}^2 \cdot \mathrm{sr} \cdot \mathrm{nm})$, $P(\lambda)$ is the fractional transmission through a beamsplitter used to route light to the two ICCDs used in each experiment , $N_f(\lambda)$ is the fractional transmission through a spectral filter designed to remove the potentially damaging 532 nm diagnostic laser light from reaching the sensor, $Q_E(\lambda)$ is the quantum efficiency (manufacturer specified, in A/W) of the ICCD photocathode, S_A is the solid angle of the collection optics, E_A is the emitter area imaged by the optics on the sensor, r is a loss due to reflections at the glass interfaces (for example, the chamber window and debris shield), g_a is the electronic gain setting of the MCP together with the digitizer after the CCD (in $\mathrm{counts/electron}$) , g_t is the gate width of each image, p_t is the fractional transmission through the Parylene-N dielectric, $O_{ldm}(\lambda)$ is the transmission through the collection optics, $N_B(\lambda)$ is the transmission through a secondary lens behind the primary collection optics, P_n is the number of pixels on each sensor, and finally $R(\lambda,T)$ is the expected number of counts per pixel per wavelength over a given duration image of a given temperature blackbody, T. The algorithm is computed for each image to account for shot- and camera-dependent quantities like gate width, gain setting, spectral responsivity, etc.

The intensifier head on the ICCD cameras deposit an image onto a phosphor screen, which is then imaged by the CCD on slower timescales. An additional factor associated with the lifetime of the Terbium-doped Gadolinium Oxysulfide ($Gd_2O_2S{:}Tb$, also known as a type P43) phosphor, which carries an exponential decay constant of ~ 650 us, needed to be taken into account – the CCD shutter was variably set during experiments, and therefore each image had to be scaled by the fraction of light that was recorded during the CCD shutter, relative to a CCD shutter open for the entire decay of the P43 phosphor.

Integrating $R(\lambda,T)$ over the system bandwidth ($300-900$ nm) yields a curve of expected counts vs temperature, $C(T) = \int_{300}^{900} R(\lambda,T)\, d\lambda$. By inverting this curve and getting $T(C)$ in integer steps from zero counts (technically, only those above the noise floor matter) up to the bit depth of the camera, we interrogate each pixel and ask: given how many counts it recorded, what temperature blackbody would have emitted sufficient light that, when attenuated the right amount at each wavelength through the optical system, would have yielded that many counts. With this analysis algorithm in place, and after appropriate background subtraction, ICCD images of thermal emissions of metal surfaces were converted to temperature maps.

ICCD images at different times, once converted to thermal maps, are suitable for time-dependent Fourier analysis. More specifically, axial Fourier mode amplitudes from patches 60 μm in azimuthal and 300 μm in axial extent were computed. Then, to the logarithm of the scatterplot of a given modal amplitude vs time, a root-mean-square linear fit coefficient is computed. Each coefficient denotes the exponential growth rate of thermal perturbations at wavenumber specific to that Fourier mode. Plotting growth coefficients vs wavenumber, $\gamma(k_z)$, and fitting the data, we determine that $\gamma(k_z) \sim 0.06\ \mathrm{ns}^{-1} - (0.4\ ns^{-1} \cdot \mu\mathrm{m}^2 \cdot \mathrm{rad}^{-2})k_z^2$. That $\gamma(k_z)$ carries a quadratic

dependence agrees with theoretical estimates. In addition, the computed long wavelength ETI growth rates are within an order of magnitude of theoretical predictions.

The data indicate that there is an electrically driven thermal instability in dense metal driven by intense pulsed current – more details can be found in the publication based on this analysis (see citation at the start of this section).

3. INFRASTRUCTURE AND DIAGNOSTIC INVESTMENTS

Experiments associated with this project were executed on Sandia's Mykonos Facility. Mykonos has historically been used for powerflow studies, which used electrical and fiber-based diagnostics routed within the vacuum vessel. Diagnostics located outside of the vessel were minimal. By contrast, the ETI experiments fielded gated optical imaging, spectroscopy, radiometry, laser imaging, PDV, and holography. All diagnostic systems have critical hardware outside of the vacuum chamber, much of which must be carefully aligned and rigidly mounted. Furthermore, ETI initiation occurs at sub-eV temperatures, when the intensity of self-emission is low. This motivated the need for a new small radius vacuum chamber with large optical viewport, to optimize light collection. In this section, we discuss infrastructure and diagnostic investments made to the Mykonos Facility in support of ETI physics studies.

3.1. Infrastructure Investments

Small radius target vacuum chamber with large optical viewports

Motivation: Nonuniform ohmic heating of condensed metal and vapor initiate at low (sub-eV) temperature. At such low temperatures, the low intensity self-emission from the z-pinch makes radiometric and self-emission measurements challenging (low signal levels). By moving the diagnostics closer to the physics load, a larger solid-angle is captured, signal levels are higher, and lower temperature emissions can be measured.

Execution/Implementation: A new vacuum chamber was designed and fabricated. The radius of the chamber was minimized to reduce the distance between the target and diagnostics. As most diagnostics are sensitive to visible light, the chamber includes 7 optical viewports. 3 have 2.5" diameter clear glass openings (larger than the 2.3" long distance microscope opening, a workhorse optic for these experiments) and 4 have 2" diameter clear glass openings. Microscope slide "debris shields" are placed between the load and the windows to protect the windows from debris. Debris shields are replaced after every experiment and vacuum windows are not damaged. Four 2.75" SMA feedthroughs are also included in the chamber. The chamber OD is 10". The center of the load (and the center of the viewports) are in a plane 4" beyond the plane of the outward facing surface of the optical breadboard of the diagnostics framework (discussed later in this section). Th one oversized port shown in the right-hand image of Fig. 3-1 is for vacuum pumping. This port was fit with a cross, enabling simultaneous vacuum pumping, and optical diagnostic access. This modification was made to enable simultaneous self-emission imaging and laser imaging, about perpendicular lines of sight (laser imaging is discussed later in this section).

The inner wall of the chamber has 4 rings of tapped ¼-20 holes which can be used for mounting hardware. An additional ring of ¼-20 tapped holes are included near the chamber wall. There are 16 1" 3X2 patterns aligned to and half way between the 8 LOSs

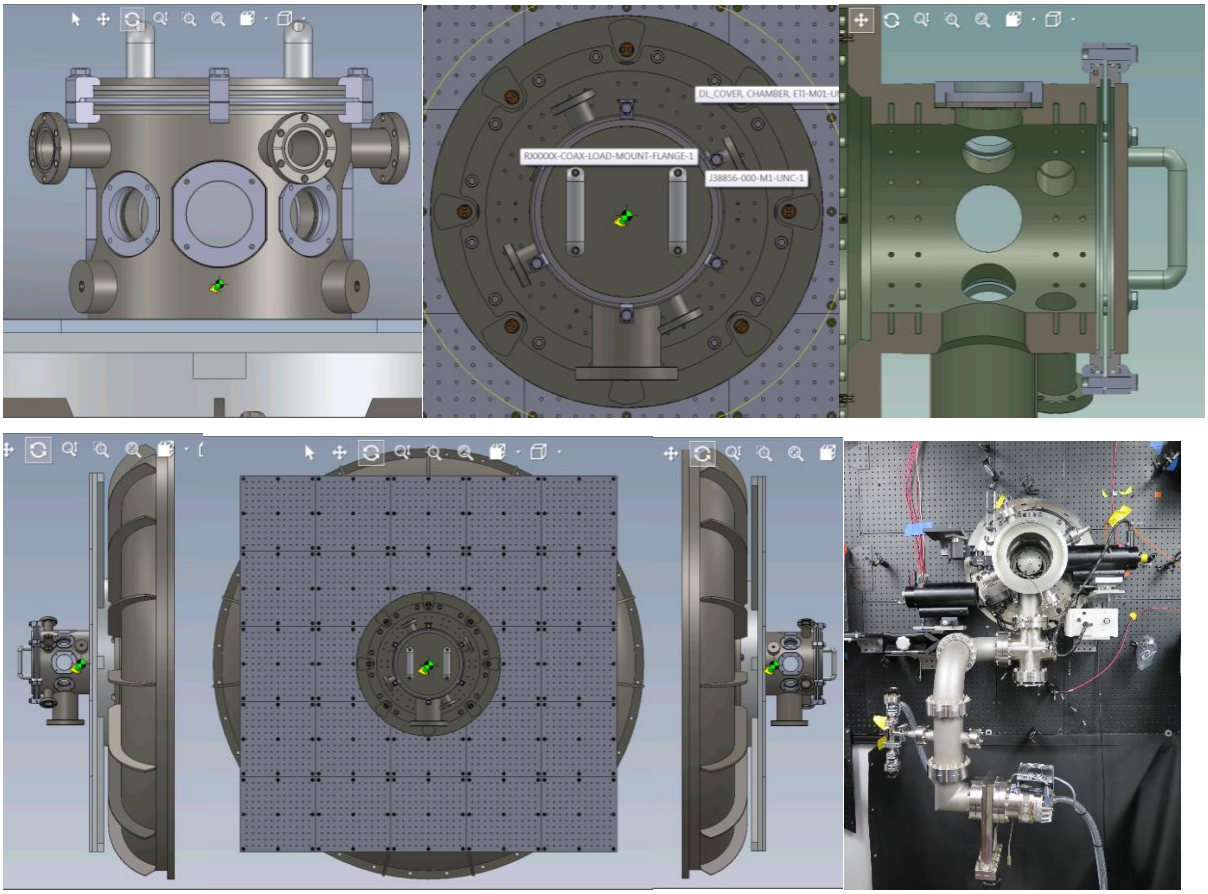

Figure 3-1. Various views of the diagnostic chamber and diagnostic framework added to the Mykonos Facility as part of this LDRD.

Powerflow hardware

Motivation: The physics load must be positioned to align to the diagnostic windows. Hardware must not limit viewport access to the load.

Execution/Implementation: Anode and cathode extensions were designed to position a barbell load at the center of diagnostic viewports. A nine-post return current can was designed with large-aperture opening maintaining mostly unobstructed diagnostic access. The anode and cathode buttons (shown in red and blue) were tapered, again to limit any obstruction of diagnostic access.

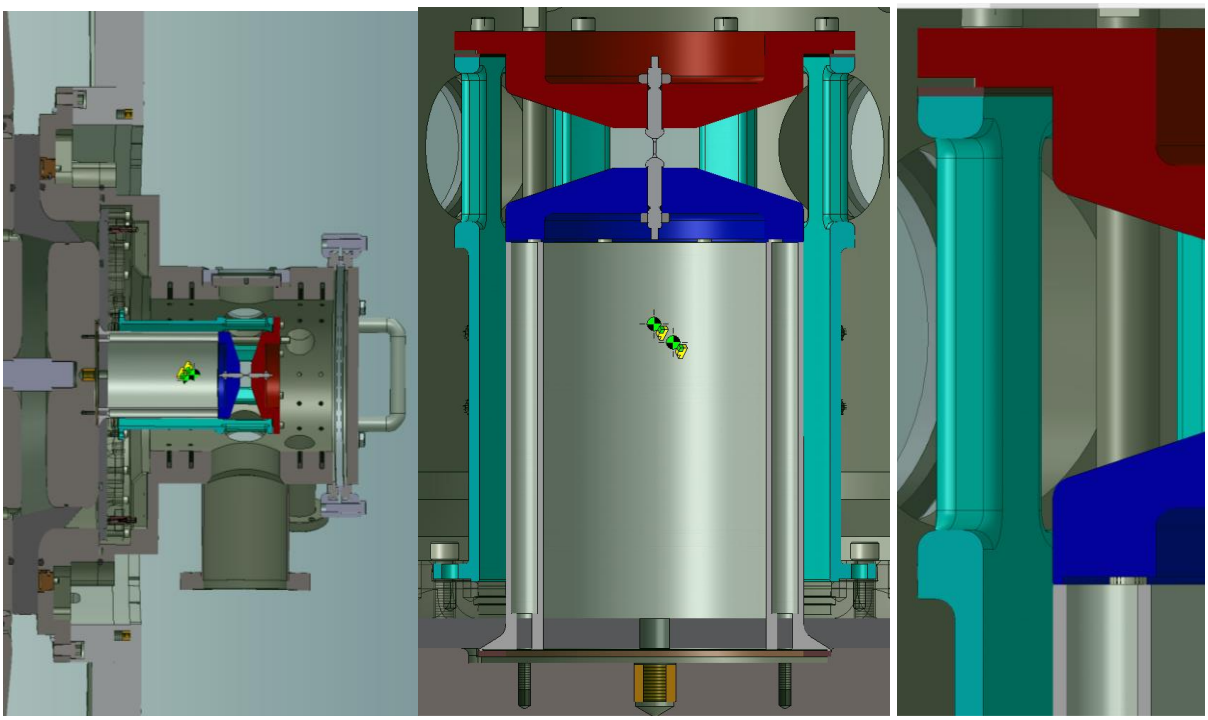

Figure 3-2. Various views of the new powerflow hardware, designed to locate the ETI physics load in the center plane of the diagnsotic windows in the target vacuum chamber. Care was taken to compress electrical contacts on the current carrying surafce of all powerflow hardware.

Diagnostic Framework

Motivation: Mykonos had historically been used for powerflow studies, which used electrical and fiber based diagnostics that were often located within the vacuum vessel. Diagnostics located outside of the vessel were minimal. By contrast, the ETI experiments fielded gated optical imaging, spectroscopy, radiometry, laser imaging, PDV, and holography. All diagnostic systems have hardware residing outside of the vacuum chamber, much of which must be carefully aligned and rigidly mounted.

Execution/Implementation: A 5'X5' optical breadboard was designed for incorporation near the Mykonos vacuum vessel. The breadboard was composed of many smaller breadboards, which were secured to Mykonos using a large Aluminum sub-structure (see left image of Fig. 3-3). The substructure was first attached to the Mykonos accelerator, with the optical breadboards later secured. In concept, breadboards could be removed, and diagnostics staged at a different location, and then later craned to the chamber. This concept of operations was never deployed. The diagnostic framework is compatible with the larger vacuum chamber typically used for powerflow measurements and also the new vacuum vessel used in ETI experiments. The optical breadboard was eventually expanded to 5' tall by 8' wide as part of the laser imaging diagnostics installation (discussed later in this section).

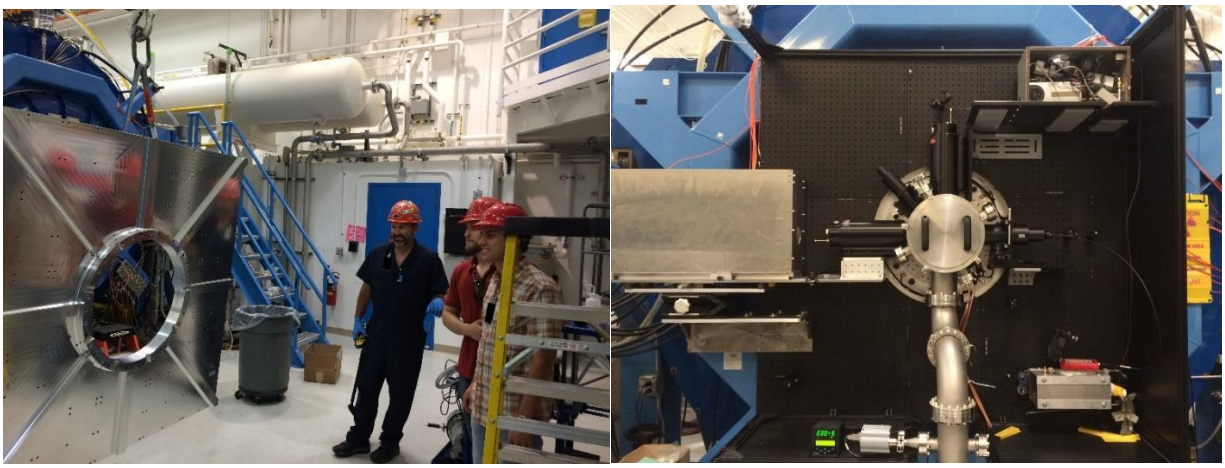

Figure 3-3. 5'X5' diagnostic framework designed for ETI experiments on Mykonos.

Development of the capability to cryogenically cool targets on Mykonos

Motivation: Data show that the evolution of electrothermal and other Z pinch instabilities are dramatically altered by the addition of a 10s-of-microns-thick plastic surface coating. The coating serves as a mass tamper, reducing instability amplitude. Many Z targets are cryogenically cooled, and in the process, microns of contaminant (mostly water) ice is gettered onto the surface of the target (the target serves as a cryo pump). We seek to understand whether this ice layer is an effective tamper of the electrothermal instability. A cryogenic capability has been developed for the Mykonos Facility. Z pinch rods will be cooled to 100 K or less to grow water ice layers of various thickness *in situ*. The existing suite of imaging and radiometric diagnostics will be used to determine at what (if any) thickness, the ice layer mitigates ETI-related expansion, and whether plasma formation can be delayed or inhibited.

Furthermore, a new concept, first tested on Z in August of 2019, uses cryogenically cooled convolute hardware to reduce the pressure in the inner MITL and target region. The intent is to reduce impurities in current carrying surfaces downstream by enabling more rapid outgassing due to reduced vacuum pressure. But, as the convolute hardware is Ohmically heated during the experiment, the evolution of the ice accumulation on convolute surfaces, which may be 100s of microns thick, is uncertain. Mykonos experiments also intend to examine the evolution of very thick layers of water ice, to aid in better understanding any undesirable impacts of this new differential pumping scheme.

We propose Mykonos experiments to study how thin layers of water ice evolve after the underlying metal is pulsed to extreme current density. We will study metallic barbell loads. The barbells will be cooled through connection to a cold head (no Dewars needed). A vacuum-chamber extension spool along with all hardware needed to thermally couple the cold head to the target have been designed, procured, and fit checked. A 480 V outlet was installed in Mykonos to power the cryocooler.

To estimate the rate of ice accumulation, the Hertz-Knudsen equation [xxvii] is applied, which expresses the concentration of molecules that stick to a surface as a function of partial pressure (p), molecular weight (m), and temperature (T). For the temperatures of interest, saturated vapor

pressures are extremely low (10^{-13} Torr [xxviii]), and the Hertz-Knudsen equation takes the simplified form shown in Eqn. 1, where δ_{ice} and ρ_{ice} are the thickness and density of the ice layer, respectively, and k_B is the Boltzmann constant.

$$\frac{d\delta_{ice}}{dt} = \frac{\alpha p m^{1/2}}{\sqrt{2\pi k_B T}} \cdot \frac{1}{\rho_{ice}} \qquad (1)$$

Residual gas analyzer (RGA) data from the Z vacuum chamber show that water vapor at 18 amu (with OH and O "fragment ions" at 16 and 17 amu) dominates the partial pressure of the chamber at the time of experiments (after pumping for 2 or more hours). Therefore, to emulate the Z environment, we will provide an artificial source of water to the Mykonos vacuum chamber. It has already been demonstrated that the water pressure can be precisely controlled and stabilized using serial "bleeder" valves, which allow the saturated vapor from an external reservoir of deionized water to slowly enter the vacuum vessel. By assuming that the accumulating water molecules form ice with a density of 1 g/cm^3, the ice thickness growth rate is readily estimated for different base pressures and temperatures. Taking nominal conditions of 1e-5 Torr and 50 K, an ice growth rate of 3.5 nm/second or ~200 nm/min is found. Table 3-1 includes estimates for a variety of pertinent temperatures and pressures. Prior to fielding z-pinch experiments, a variety of measurements will be made using high resolution imaging systems to determine if growth rates match expectation.

	25 K	50 K	75 K
1e-6 Torr	30	21	17
5e-6 Torr	149	105	86
1e-5 Torr	298	210	172
5e-5 Torr	1488	1052	859

Table 3-1. Estimated ice growth rates in nm/min for a variety of temperature pertinent to cryogenically-cooled MagLIF targets, and a variety of pressures pertinent to the Z vacuum chamber.

Experiments will study the evolution of ice layers of varying thicknesses ranging from <1 micron to ~100 microns. Experiments used to determine the evolution of the ice layer when the underlying metal is intensely Ohmically heated with incorporate diagnostics similar to those used on ETI experiments, including gated imaging, radiometry, and laser backlighting. An experimental goal will be to determine if/when the ice layer "blows off" from the heated surface. One hypothesis to be explored is whether the ice layer can be used to provide a dielectric surface layer to mitigate non-uniform expansion associated with the electrothermal instability. Similar experiments with varying layers of plastic surface coatings display markedly different behavior between bare loads, load with thin coatings, and loads with thick coatings (see Introduction). Whether water-ice layers behave similarly is a fundamental question to be answered by these studies.

Execution: To meet the needs of implementing cryogenic capabilities on Mykonos, new components were designed around an existing cryopump/cold head system. Modifications were made to the anode/cathode hardware commonly used in ETI experiments on Mykonos. Designing these parts required thorough consideration of thermal coupling, electrical performance, and structural loadings to avoid component failure and to ensure workforce safety.

In the subsections to follow, we will discuss hardware fitment, the procedure for assembly, and structural analysis.

Hardware Fitment:

Mating a cold head onto the Mykonos assembly was necessary. The lid of the vacuum chamber was large enough to accommodate the cold heat. After retrieving the drawings from the manufacturer of the cold head, structural components to house the head were designed. Due to the low temperatures achieved by the cryopump as well as the desire to avoid thermal loses, the cryopump needed to be mounted in vacuum. To do so, an extension spool was created around a cryopump stand-in model created from the drawings such that this design requirement could be met. The important dimensions can be seen in **Error! Reference source not found.**.

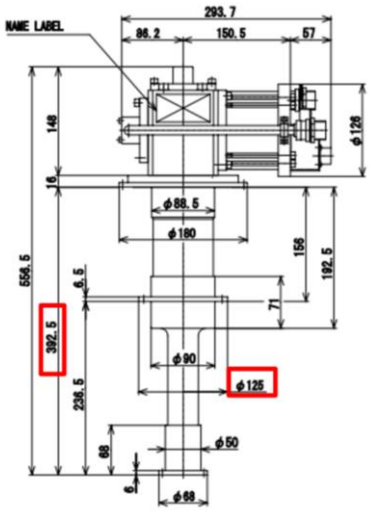

Figure 3-4. CAD model of extension spool (left) and cold head dimensions (right).

To couple the cold head to the target, a clam shell mount was designed. The clamshell first closes around and compresses the target, providing a good thermal connection. The clamshell/target assembly is then bolted to the anode, positioning the target in the experimental AK gap. The existing anode design was minimally modified adding a counterbore to the backside of the anode to located and secure the clam shell assembly. After making these modifications and modeling a cryostat, the final important detail was creating a path for heat transfer between the cryopump and the cryostat. This was simply done through taking two copper rods that would be fastened together. Piecing these components together, cryogenics for Mykonos was completed (see red box in **Error! Reference source not found.**-5).

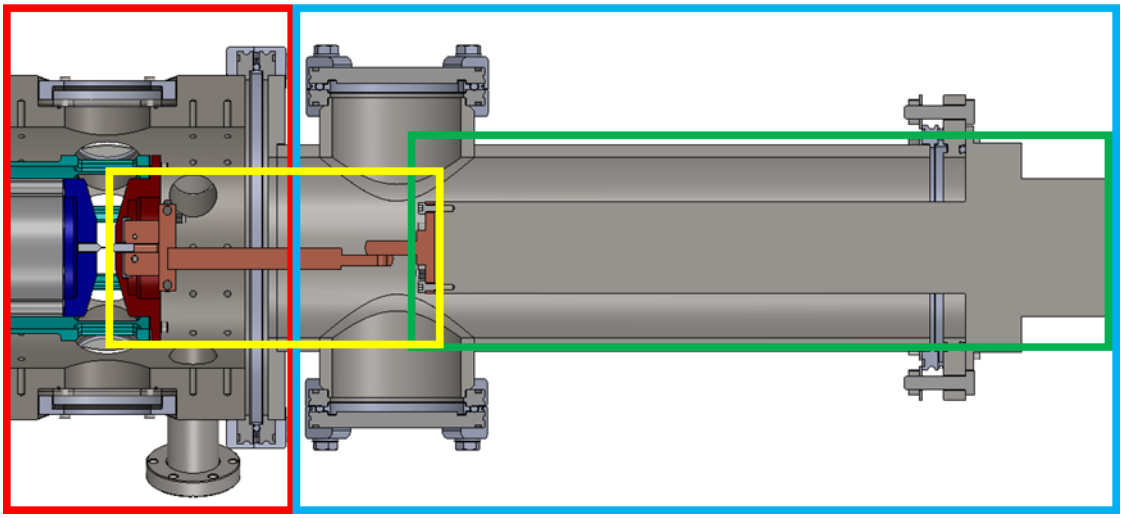
Figure 3-5. Mating the cold head to the target.

The different colored boxes in Figure 3-5 display the new cryogenic components. The red box outlines the original vacuum chamber. The light blue box outlines the new extension spool that was designed to accommodate the cold head. The green box outlines the cold head stand-in part modeled directly from the drawings provided by the manufacturer. Finally, the yellow box outlines the copper assembly that will be utilized to connect the target to the cold head.

Assembly Procedure:

1. Assemble load hardware on the machine including the cryostat hardware.
2. Next the extension spool and the cryopump will be mated together. On the tip of the cryopump, the copper piece that mates with the cryostat will be loosely connected such that location and placement can be finalized later. The two vertically oriented ports in 3-5 are access ports which allow the experimenter to complete the thermal connection after the extension spool is flown into place and secured.
3. The whole extension spool assembly will then be craned over to the Mykonos main assembly and attached through use of the claw clamps.
4. The copper piece on the end of the cryopump was not drilled due to tolerancing uncertainty so at this point, it is suggested that a mark is made through the access port to match up the through-hole drilled into the cryostat rod.
5. At this point, the extension spool assembly shall be removed and the copper piece from the end of the cryopump will be drilled.
6. Once this is completed the extension spool assembly will again be placed onto the machine this time using the access ports to fasten the two connecting rods between the cryostat and the cryopump together.
7. At this point experiments can take place. Once an experiment concludes, the extension spool assembly must be completely removed such that a new load can be inserted.

Structural Analysis:

A structure analysis was completed to ensure no components would fail. Thee access port plates, the extension spool, the lid where the cryopump mounts were evaluated, with the additional

weight added to the vacuum spool considered in calculations. Due to the portion of weight that is cantilevered off the main face of Mykonos as well as the pressure loading from vacuum, concern for the structural strength of both the extension spool and original vacuum chamber required exploration. Both the access port plate and the cryopump lid were of low concern (and won't be shown here) but the simulations were completed for insurance and resulted in FOS values much greater than 3 (the required value). The results of the analysis are as follows.
The extension spool assembly (which was the largest concern) resulted in a maximum stress of 7788 psi putting the assembly at a FOS of 3.85 to yield (shown in **Error! Reference source not found.**). This simulation was completed with a minor delta r between the main tube and the flange with which it is welded to simulate reality and therefore the stresses will be larger at the interface (aka the maximum value). When changing the model to not have this feature and re-running the simulation the stresses reduced by a factor of 4.

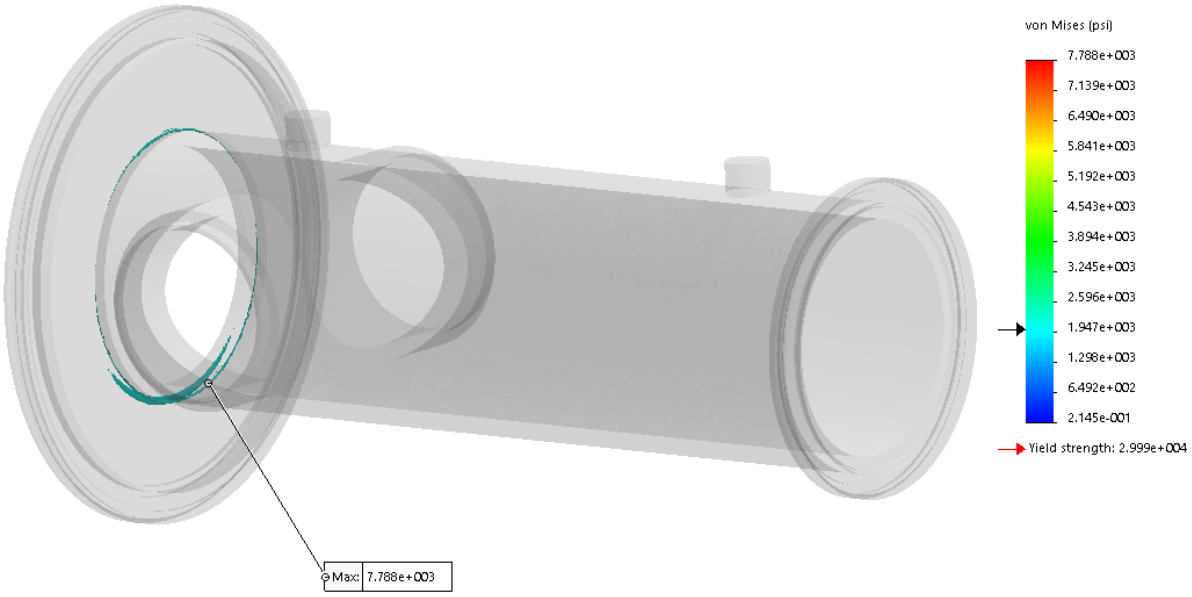

Figure 3-6. Results of FEA simulation of Extension Spool

The original vacuum chamber assembly had already had an FEA simulation for operating conditions and therefor was copied and modified to include the cantilever weight on the end of the spool. Upon running the simulation, the results were a max stress value of 7322 psi which is a FOS of 4.1 to yield (show in Figure).

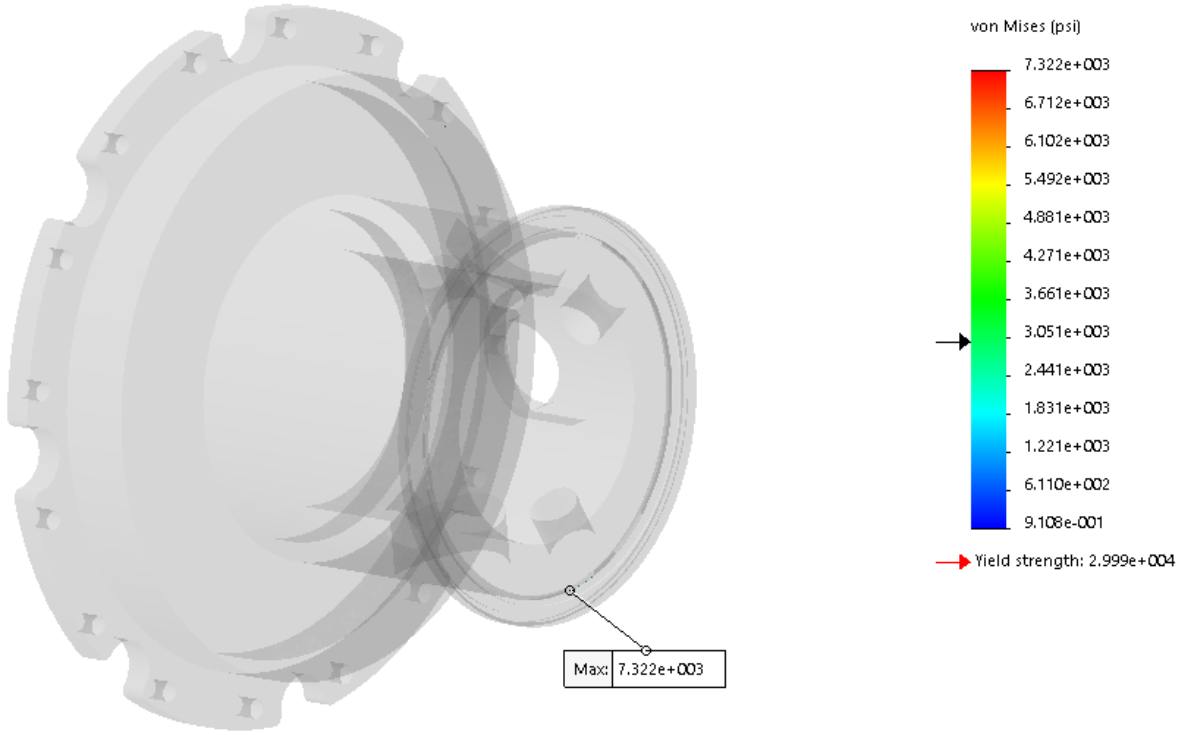

Figure 3-7. Results of FEA simulation of Original Vacuum Chamber with cantilever loading

In addition to these analyses, concern was brought up about the claw clamps that are utilized for the COTs flanges. Since the clamps are aluminum the concern was that they would be insufficient to hold the weight that will be cantilevered off the original vacuum chamber (the new extension spool and cold head). Since the moment generated by the weight of the extension spool is known, a simple model was made to determine what the force loading at the top of the flange would be to keep the system in static equilibrium (which turned out to be 155 lb). After discussing with the manufacturers, it was noted that 4 clamps at the top most point of the circumference plus another four equally distributed along the remainder of the circumference would be sufficient to hold the load up.

Laser Control Area (LCA)

Motivation: A new laser capability has been installed in Mykonos and will enable diagnosis of plasma plume generation and evolution from engineered defects. The laser is an Nd:YAG Ekspla system consisting of a 170 ps pulse length with 1064 nm (500 mJ), 532 nm (240 mJ), 355 nm (140 mJ), and 266 nm (80 mJ) harmonics. The 532 nm harmonic will initially be used for laser imaging, including shadowgraphy, interferometry, and Faraday Rotation imaging, and the 355 and 266 nm harmonics will initially be used for UV breakdown experiments used to develop the AutoMag concept (AutoMag was initially supported through an Exploratory Express LDRD, but is now supported by the ICF program).

Execution/Implementation: The laser system, all associated optics and optical tables, and the Mykonos target chamber, are currently housed in a laser-controlled area (LCA) consisting of a light-tight cleanroom with a single interlocked entrance. The interlocked entrance ensures safe

operations of enclosed laser systems, including the Ekspla laser, and the fiber coupled PDV laser. The room includes a roof-mounted HEPA filter to protect the laser and external optics from contaminants including dust and oil vapor. The Ekspla laser resides on a 3'X5' optics table, with "receive" optics (e.g. CCD cameras) located on a similar optical table located on the opposite side of the LCA. The LCA includes a removeable laser curtain, which generally closes the roof, but can be opened/removed to allow crane access inside of the LCA. Crane access is required to remove the vacuum vessel for change out or insulator stack refurbishment.

Figure 3-8. Images of the new LCA installed in the Mykonos Facility.

3.2. Diagnostic Investments

Laser Shadowgraphy implementation on Mykonos

Laser shadowgraphy is a type of laser imaging that can be used to observe the boundary of a plasma. In its simplest conception, laser light is incident upon a target whose properties prevent the laser light from reaching a detector, leaving behind a "shadow" of the target via three effects—mass attenuation (e.g. absorption), diffraction, and refraction. When the target is in the plasma state, strong gradients in the electron density produce gradients in the index of refraction which can refract (deflect) light outside of the optical system. Technically, this is considered a type of circular aperture Schlieren, and is very useful for identifying the boundary of the plasma. For reference, the true shadowgraphy effect is related to the second derivative of the index of refraction. This can be understood as follows. Consider laser light traveling through an object with a constant gradient in the index of refraction. This light will be deflected by some angle and will uniformly illuminate a detector (so long as the deflection is sufficiently small so that the light can be collected by the optical system). Variations in the first derivative of the index of refraction (i.e. second derivative) will then produce bright and dark regions of light depending on how the rays of deflected light overlap at the detector—this is the true shadowgraphy effect. In practice, it is much simpler to interpret plasma boundaries that are produced by the first derivative; however, one may typically find bright and dark regions of light surrounding features such as plasma jets that are due to this second derivative effect.

In CY19 we commissioned an Ekspla brand Nd:Yag Class IV laser for imaging the metallic barbells pulsed to high currents. Implementation of this diagnostic required new infrastructure including a laser-controlled area, optical tables, and an interlock system. Many months of safety reviews were conducted to ensure best practices when operating this new system. The LCA also serves as a cleanroom with a HEPA filter designed to reduce dust and limit hydrocarbons from the Z machine.

Figure 3-9. A new laser controlled area (LCA) was established (white structure, left) to confine the laser beam within a light-tight structure. The LCA was populated with an additional four optical tables that house the laser, optics and cameras (two are shown on right with laser).

The laser has the capability to produce four wavelengths of light including 1064 nm (500 mJ), 532 nm (240 mJ), 355 nm (140 mJ) and 266 nm (80 mJ), where the energies in parenthesis are the maximum energy the laser can produce for that wavelength. The pulse length of the laser is 170 picoseconds, which sets the time resolution of the diagnostic. The laser is typically coupled to a time-integrated camera with a long exposure (~ 1 second), which collects the time-integrated self-emission (TISE) of the target throughout the entire Mykonos pulse. In practice, neutral density (ND) filters are applied which limit both the TISE and laser light. When ND is implemented, the laser has sufficient energy to overwhelm the TISE, which is required to successfully observe the dynamics of the target.

For initial commissioning of this diagnostic, we designed an optical path using the 532 nm harmonic. We created two frames by splitting the beam into two spatially superimposed beams of orthogonal polarity that are temporally delayed by 10 ns. These beams travel the same beam-path through the target and are split using a polarizing beam splitter and directed towards two separate cameras. Early testing showed leakage of one frame onto the other (about ~20%), which we deemed unacceptable for the first campaign. Thus, the first campaign consisted of shots with one frame of laser shadowgraphy data. A simple upgrade that is planned is to add a linear polarizer to each camera to eliminate the leakage of light from the other frame of orthogonally polarized light.

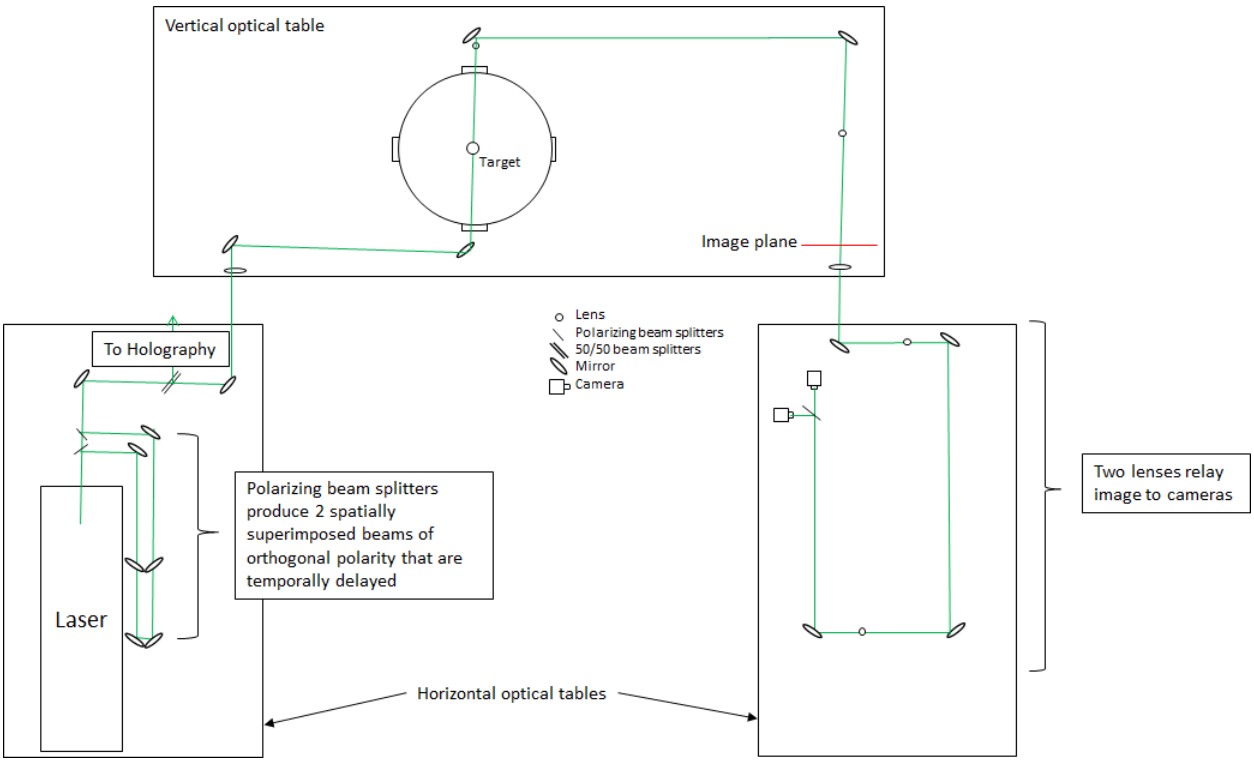

Figure 3-10. Layout of optics within LCA.

We characterized the resolution of the optical system using a USAF1951 resolution target. Using this target, the 5-6 line pair was clearly resolvable, indicating our system is capable of resolving features down to 8.77 microns (the lines and spacings are 8.77 microns for the 5-6 lines). The image shown in Figure 3-11 was taken with the CW alignment laser. Using the Ekspla laser, we have been able to resolve features down to 4.92 microns (although making this latter claim is more subjective as there is some interpretation as to what lines can be "clearly" distinguished).

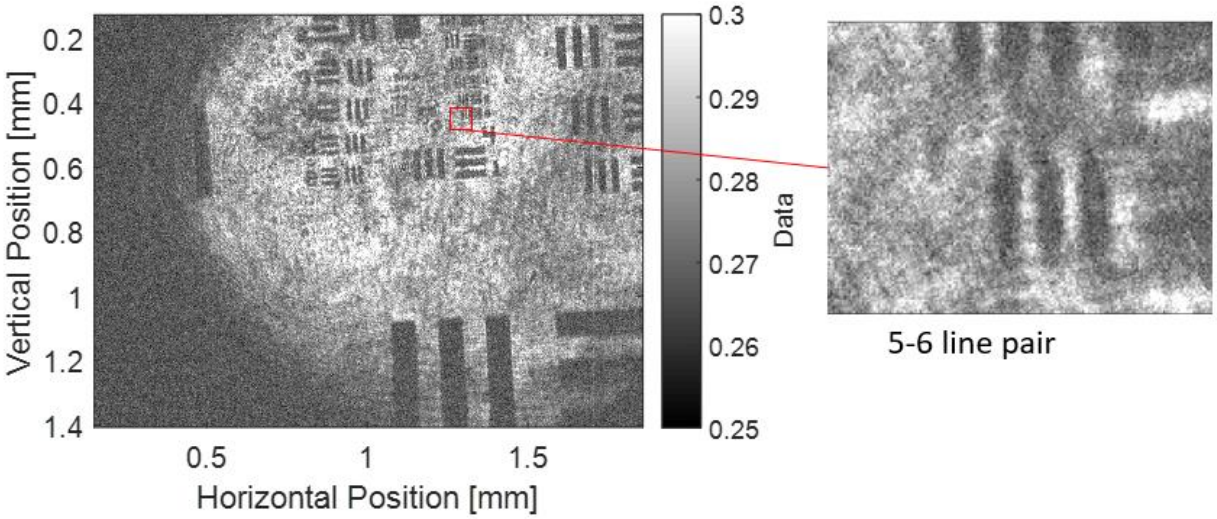

Figure 3-11. Shadowgraph of USAF1951 used to determine the optical resolution of the system.

The specific intent for this diagnostic was to image the first instability bumps that appeared following the initiation of plasma on the surface of the barbell. The striation stage of ETI leads to overheated azimuthal bands that are hypothesized to ablate and form density perturbations that seed the subsequent magneto-hydrodynamic instability development. The formation and subsequent evolution of these larger-scale instabilities can be observed using laser imaging. The first shadowgraph ever taken on Mykonos is shown in Figure 3-12.b (the preshot image of the rod is shown in Figure 3-12.a). The image shows small instability bumps (~10-40 microns in wavelength and amplitude) develop on the surface of the target. The image also shows TISE throughout the image, which is particularly evident in the rod region. The neutral density filtration was increased from ND2 to ND3 for the following shots, which successfully reduced the TISE, as shown in Figure 3-12.c.

An enlarged region focusing on a set of instability bumps is shown in Figure 3-13. The first image in Figure 3-13.a shows a set of bright and dark fringes at a radius slightly larger than the dark region of the plasma. For this image, the laser light was incident upon the camera at an angle of ~5-10 degrees. Subsequent images reduced this to zero, which consequently reduced or eliminated these fringes. The reason why these fringes disappeared is still unclear.

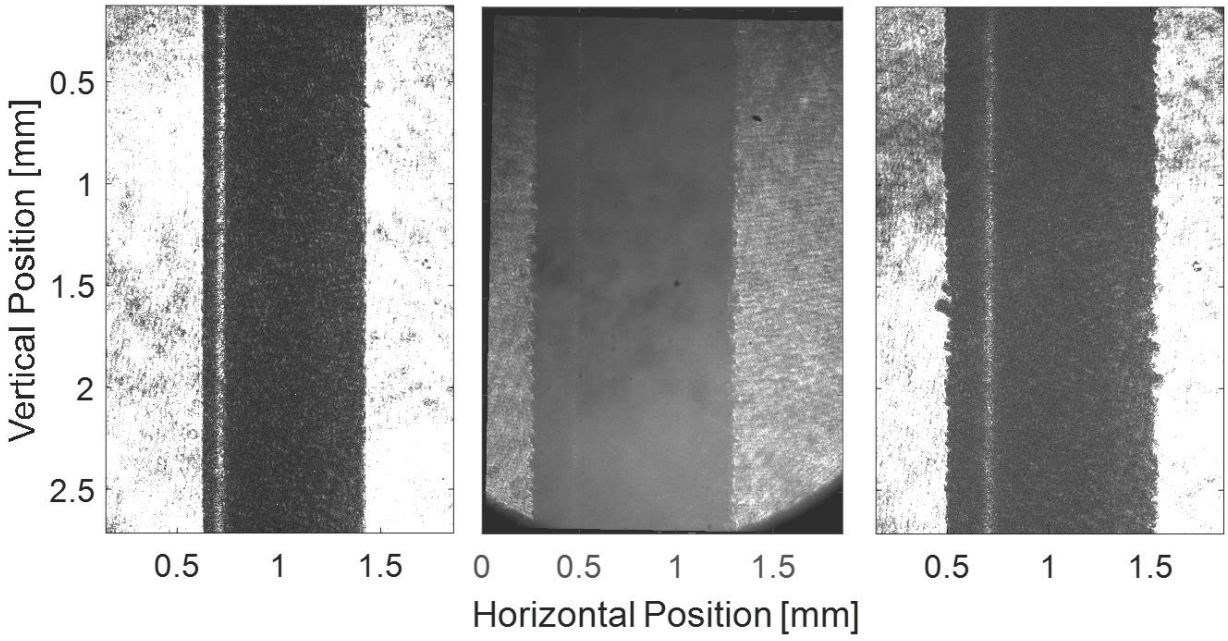

Figure 3-12. Shadowgraphs of preshot of rod (left) and shot (center image has ND = 2, right image has ND = 3 with increased laser energy).

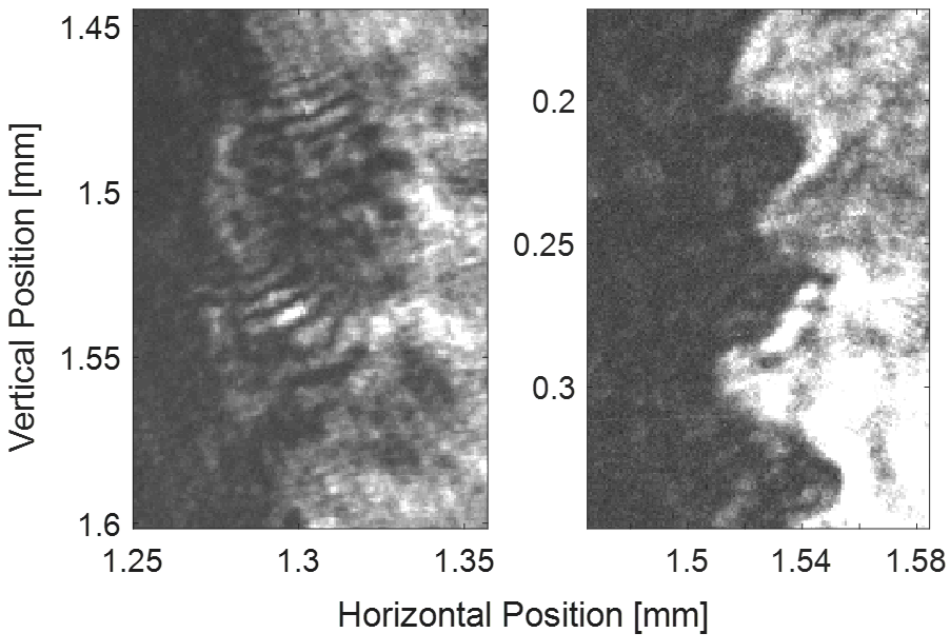

Figure 3-13. Enlarged regions of shadowgraphs from Figure 3-12. Image on left was taken using an angle of incidence on the camera of ~5-10 degrees, and shows bright/dark fringes in the instability bumps. These fringes were eliminated/reduced when reducing the angle of incidence to ~0 degrees.

Future upgrades to the imaging system are planned for FY20. These include additional beam paths for the various wavelengths (e.g. 1064 nm, 355 nm and 266 nm), implementing more complex imaging diagnostics (e.g. interferometry and Faraday rotation imaging) along with improvements to the beam quality (e.g. spatial filtering). Laser imaging is being requested for many of the campaigns currently proposed for Mykonos in CY20, including the ETI (Awe), AutoMag (Shipley), plasma cleaning (Lamppa), active dopant spectroscopy (Patel), and IDTL (Myers) campaigns.

Dual view, four frame imaging system development

Low intensity emissions, a likely result from overheated inclusions in alloyed aluminum, drive ETI in Z pinch targets. One objective of ETI research is to experimentally study the evolution of ETI from targets with well-understood and well-characterized engineered defects for comparison with simulations (see Section 6 for a full discussion).

Defect patterns will include 2 pairs of defects, separated by 180 degrees on a ~1 mm diameter metallic barbell target. The development of a multi-camera splitter system will be used to simultaneously image these scaled defect patterns, allowing for concurrent observation of overheating evolution on the two sides at multiple points in time.

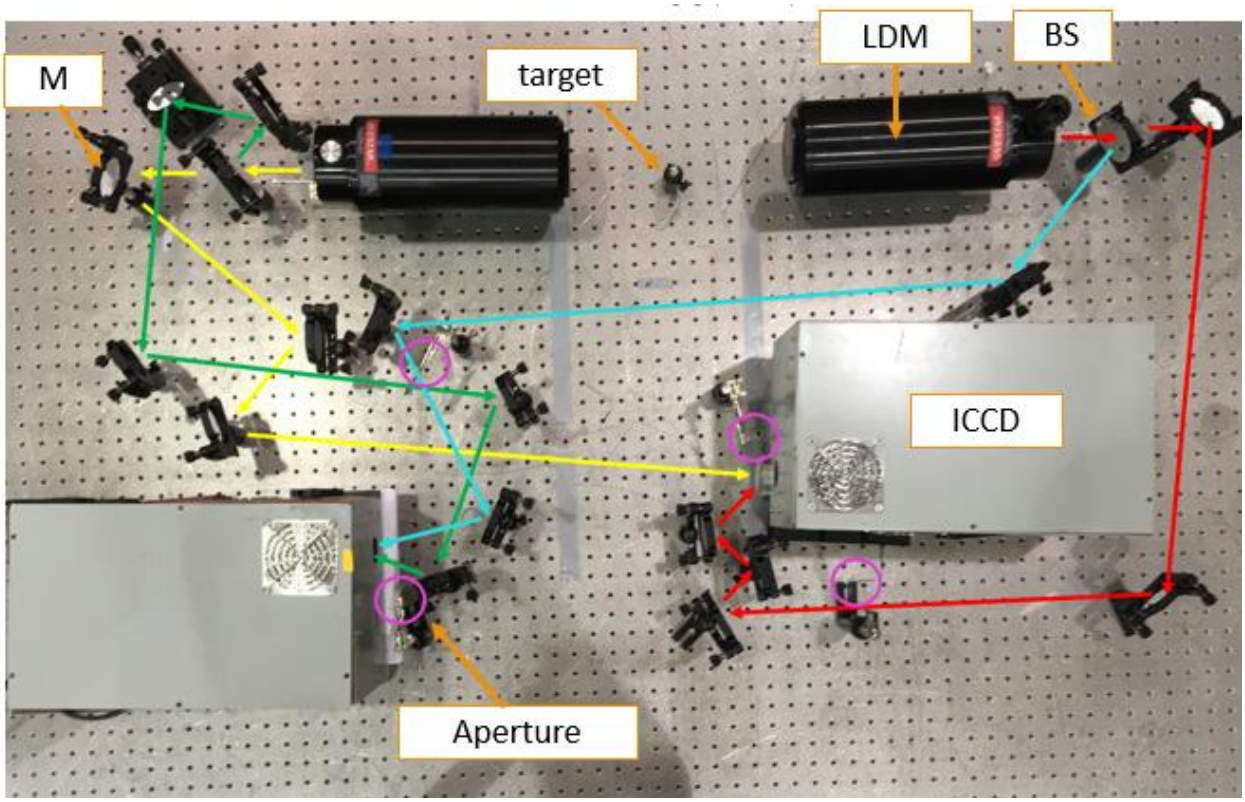

Figure 3-14. Schematic of double-sided imaging optical setup.

Two Questar QM 100 photo-visual long-distance microscopes will each be aimed at one set of defects on either side of the target to magnify the image. Cameras with 2-5 ns gated exposures are required to resolve the rapid evolution of ETI-driven temperature nonuniformities. This experimental setup uses Andor iStar 334 and 340T time-resolved ICCDs. Both optical paths measure 60 inches, with a magnification of approximately $M = 31.25$. The resolution of the system will be characterized by a USAF1951 resolution target. Apertures will be implemented to block half of each final image, allowing for two images side-by-side on the camera sensor.

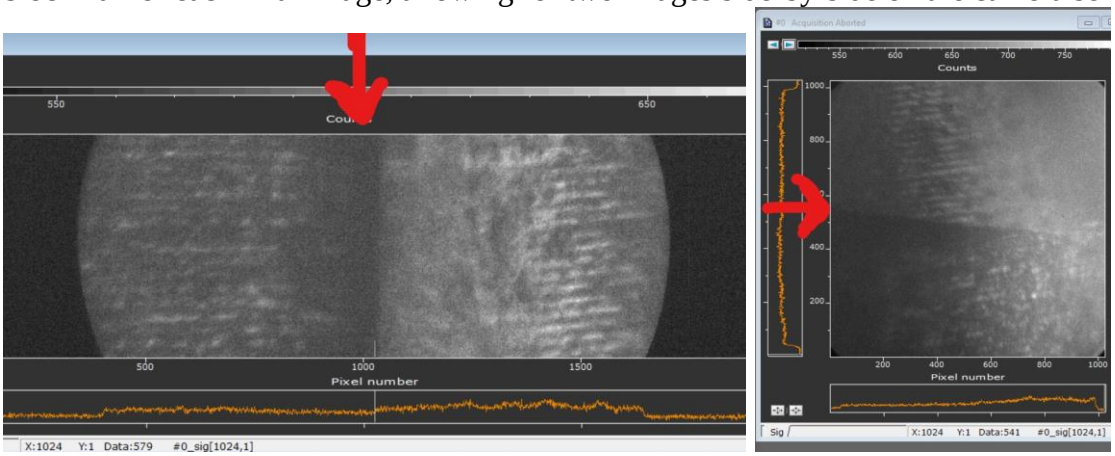

Figure 3-15. Images of the front and back of a test barbell. Images on the sensors of the Andor 340 (left) and 334 (right) were separated as indicated by the red arrows.

The capability to have two simultaneously imaged defect patterns will demonstrate how engineered defect overheating evolution differs with varying defect parameters (depth, diameter, and distance between defects). The timing between the two cameras can be adjusted to provide information on this evolution at different times in the experiment. Future adjustments to the system will aim to shorten the path length for smaller magnification of the image.

Holography:

Digital holographic microscopy is a form of interferometry that can provide 3D information about small objects using coherent light. It may be used either for semi-transparent or reflective objects, and may be fielded in-line, or off-axis configurations. In-line holography is better when multiple exposures can be taken, and off-axis holography better is when only a single exposure is possible. When the off-axis, reflective techniques are used, holography can provide topographical information about a reflective surface with time-resolution limited by the smaller of the laser pulse duration, or CCD shutter duration. Using a 170 ps, 532 nm laser, the topographical structure of conductor 'surfaces' exploding on ns timescales can be mapped.

The basic idea behind holography is to interfere light directly from a laser (with planar phasefronts), with light that has reflected off a bumpy surface (with phasefronts initially conforming to, but diffractively evolving from the bumpy surface), and to record interference fringes at a distance. These fringes form a pseudo-topographical-map of the surface (after having accounted for the equidistant fringes due to the bulk angle between object and reference wavefields, $\left\|\overrightarrow{k_{E_0}} - \overrightarrow{k_{E_r}}\right\| = \theta$). A measurement of the superposition of an object laser field $E_0(x,y)$ and reference laser field $E_0(x,y)$ will yield an recorded intensity $I(x,y)$. x and y denote dimensions mutually orthogonal to the laser propagation axis, at the sensor plane (coordinates left off the right part of the equation for clarity):

$$I(x,y) = |E_0(x,y) + E_r(x,y)|^2 = |E_0|^2 + |E_r|^2 + E_0^* E_r + E_0 E_r^*$$

The first two terms on the right-most equation are called the DC terms and are not of primary interest – they may be subtracted from the intensity image, provided suitable pre-shot images are taken. One of the cross terms is arbitrarily called the hologram term, and the other the twin term. They may be distinguished in an image in that they are complex conjugates of each other and may be separated via angular filtering techniques [xxix]. Once the hologram is obtained, application of the Rayleigh-Sommerfeld diffraction integral yields the phase fronts propagated back to the object plane. The effect of a lens system may be accounted for by optic matrix calculations [xxx], and corrections due to the phase front curvature error introduced by lenses may be subtracted off. The pre-shot reference and object fields (i.e., DC terms) may also be subtracted off.

The designed layout of optics is shown in Fig 3-16. The target is a 1-mm diameter Aluminum 6061 barbell. The curvature of the barbell indicates only a very narrow angular width of the barbell would be suitable for reflecting light (related to the $f/\#$ of the collection optics and range of incident angular wavenumbers $\vec{k}$ carried by the incoming laser beam). To account for this, a flat surface was milled into the barbell along the barbell axis. The width of this flat face was variable, but typically ranged from $100 - 300\ \mu m$, and the length was along the entire barbell length, ~ 7 mm.

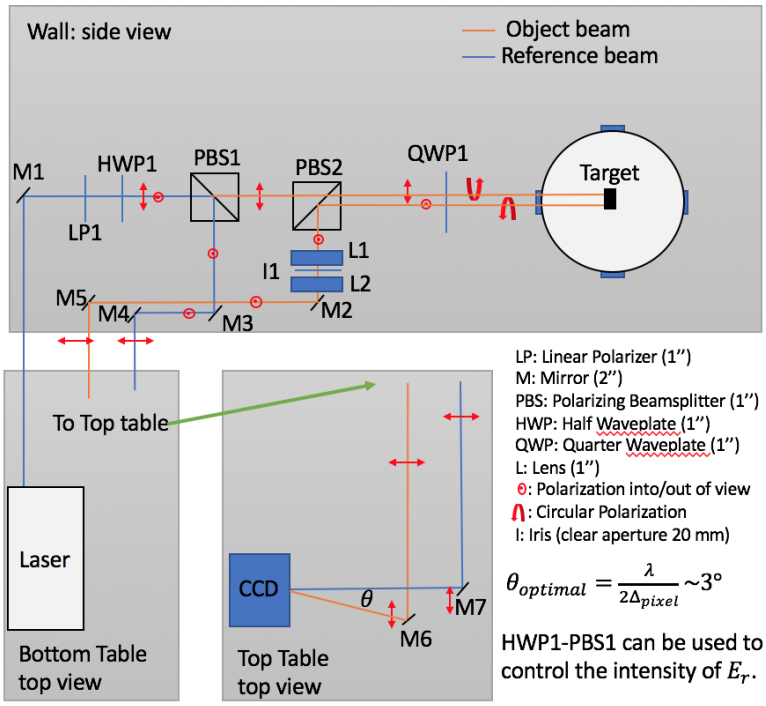

Fig. 3-16. A representative schematic of the 3D layout of optics for holography experiments. HWP1 was used to control the amount of Ekspla light split between the reference and object beams. The QWP1 was used to route retro-reflected light into a new beampath, towards L1. Lenses L1 and L2 are lenses with focal lengths 206 mm and 3000 mm respectively. L1 is approximately 200 mm from the target, and L2 is approximately 3000 mm from the CCD. The path lengths of the object and reference arms were matched to better than a mm. M4 and M5 turn the beam normal to the wall, and parallel to the tables. In the experimental realization, the distance between M6 or M7 and the CCD was small enough, and the mirrors large enough that an acceptably small θ couldn't be achieved without using a non-polarizing beamsplitter to recombine E_0 and E_r beams, which was, in fact, what was required.

Optical layout was evaluated in design space with Zemax and Solidworks (see Fig. 3-17). Calculations indicated nearly diffraction limited performance, with an expected resolution of approximately 10 µm (corresponding to a diffraction limited $f/8$ system using 532 nm light), and a Magnification of 15. The camera was a ML8300 Finger Lakes Instruments CCD, containing 3448 x 2574, 5.4 μm pixels and a 16-bit A/D converter.

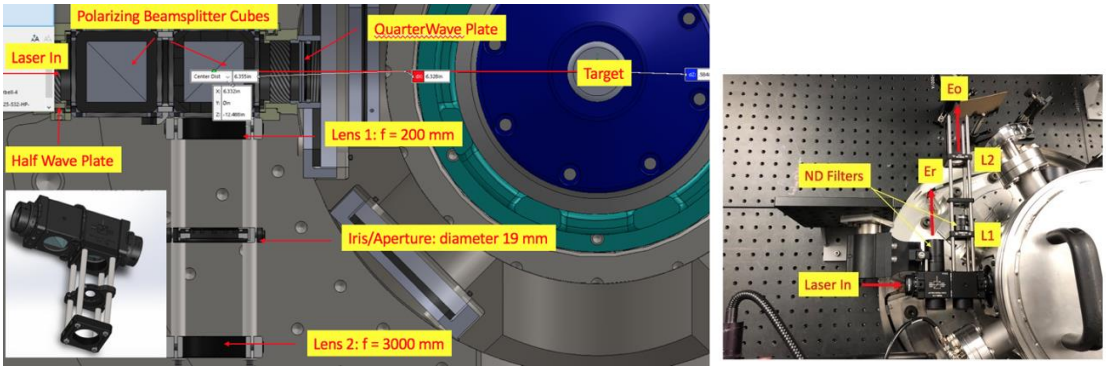

Figure 3-17. a) Solidworks drawing (section cut perpendicular to rod axis halfway between target extremes) of load-facing holography optics and b) experimental realization of the design. The word 'Target' in the image correspond to the location of the barbell at target chamber center (TCC).

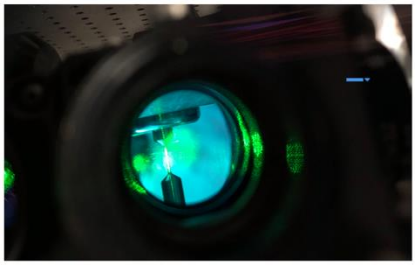
Fig 3-18. View looking back down the vacuum port through the imaging optics. The bright central part of the barbell is visible, together with the cathode at the top of the image.

The laser bandwidth is $\Delta\lambda = 2.83$ pm (0.1 cm^{-1}), which corresponds to a coherence length of $L_{coh} = \lambda^2/(n\Delta\lambda)$, or 10 cm. This is longer than the laser pulse length, 5.1 cm, so the laser pulse is expected to be coherent through its entire duration. A co-alignment diode laser was used for setup and alignment, with a 1 nm bandwidth (equivalent to a coherence length of 300 μm). To find interference fringes without Ekspla, the path lengths needed to be matched to sub-mm accuracy. This was achieved by mounting 2-delay mirrors to a precision micrometer stage such that the reference laser direction/alignment would be unperturbed, but the reference laser path length could be modified by moving the stage. The stage was then scanned, at 250 μm intervals, until interference fringes appeared for the alignment diode laser. By this technique, the path difference between object and reference beams was matched to within the coherence length of the diode laser, aka sub-mm accuracy. This guaranteed maximal contrast when switching to the Ekspla laser.

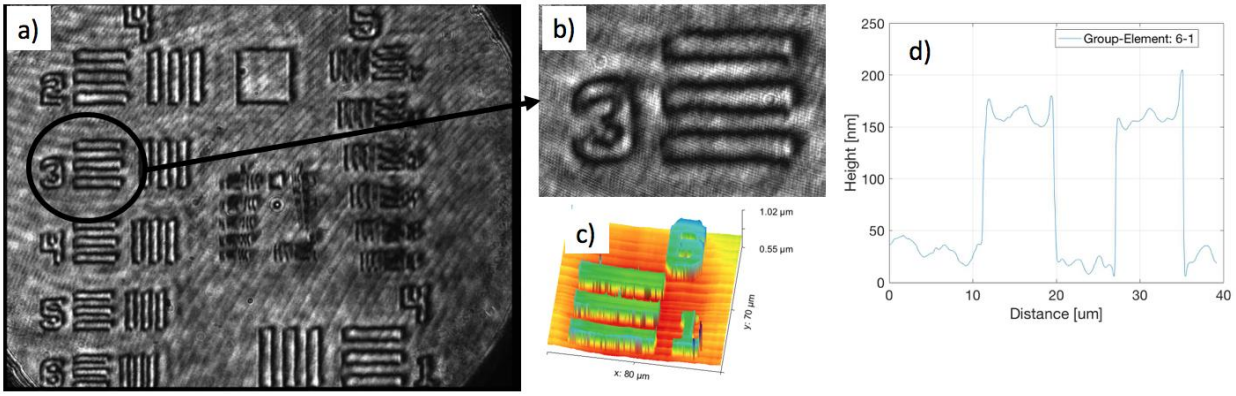

Fig 3-19. A) An intensity image representing DC, hologram, and twin terms corresponding to a USAF 1951 reticle at TCC, sputter coated with ~ 10 nm of a 50/50 Gold/Palladium mixture, b) an expanded thumbnail from a), demonstrating interference fringes whose perpendicular is ~ 30 degrees clockwise from vertical, c) confocal microscope data of the same reticle representing the surface height of the reticle lettering and d) a lineout along the 6-1 element of the confocal data in c), demonstrating the lettering is 128 nm taller than the background (approximately consistent with the mfgr. specified 120 nm measurement).

Fig. 3-19 demonstrates that the experimentally realized magnification was M = 14. In addition, naïve inspection indicates group 5 element 6 is resolved, corresponding to a lateral resolution of approximately 10 µm, although some astigmatism is present. Confocal data lineouts (Fig 3-19.d) show the lettering is 128 nm above its background, indicating there should be a discontinuity across the lettering of the reticle of approximate size 128 nm / 266 nm ~ 0.5 a fringe shift, while very coarse inspection of Fig 3-19.b indicates a fringe shift of 0.7, or a 190 nm height, approximately consistent with the confocal data. A correct evaluation of the lateral and longitudinal resolution will depend on computation of the full Rayleigh-Sommerfeld diffraction integral, angular filtering, and curvature subtraction techniques, which are left for future analysis.

Consider a metal surface moving with velocity $1\ \mathrm{km/s}$ – during the 170 ps laser pulse width, the surface is expected to move 170 nm. Therefore, what started as a bright band becomes a dark band at the end of the pulse (a little more, since 170/266 is more than 50% of a fringe shift), and the time-integrated response corresponds to a reduction in contrast. Therefore, the window in which holography has best contrast is restricted to portions of the experiment in which the exploding metal is slowly moving, or, relying on PDV data (see Appendix A), between a surface magnetic field 85 T (when surfaces melt) and 200 T (approximately when the surface velocity is $1\ \mathrm{km/s}$). Although better time resolution can be obtained by temporally delaying either the object or reference beam with respect to the other (so the overlap in beams is of shorter duration), there will still be a reduction in contrast due to extra intensity in the DC terms. This can be resolved by using a laser with pulse length duration over which the surface moves slowly enough to insignificantly shift the fringes. Fringe shifts of flat-faced targets in chamber are shown in Fig. 3-20.

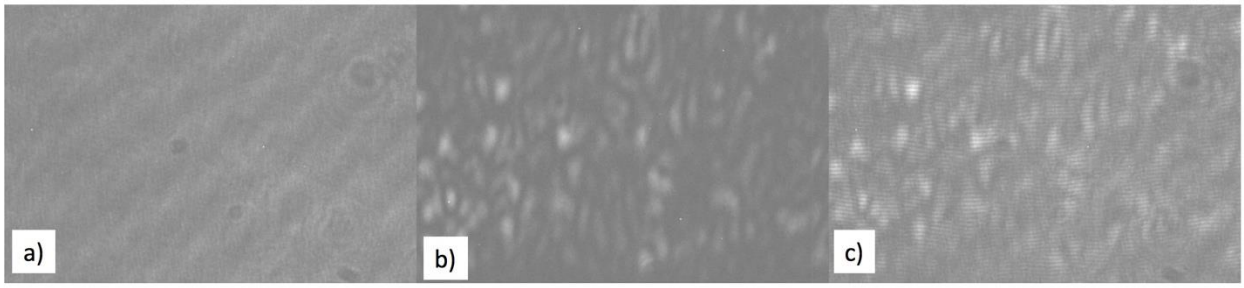

Figure 3-20. a)$|E_r|^2$, b) $|E_0|^2$, $|E_0 + E_r|^2$ images, taken by sequentially blocking the object, reference, and no beam respectively – the object in these images was the flat face of a barbell. Note the fringes that appear in c) are not in either of the individual, non-interfered beams. Fringe spacing is ~ 4 pixels, corresponding to an angle between incident reference and object wavefields of approximately 18 °, much larger than the suggested optimal angle of 3 °. It is not clear that this will negatively affect the total diagnostic returns.

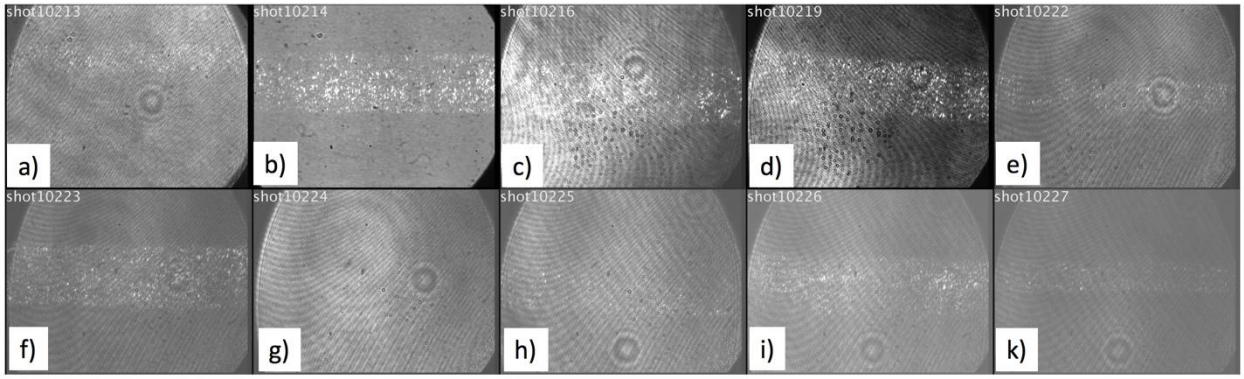

Figure 3-21. Raw recorded intensities corresponding to 10 shots. b) and g) were taken having accidentally neglected removing a beam block in front of E_r and E_0 respectively, and fringes appear for the remaining 8 shots. The horizontal band of variable width across each other frame corresponds to E_0, and the large oval to E_r. The bright background in b) is due to TISE – subsequent shots had sufficient neutral density filters (and increased laser energy) to bypass this problem.

Fig. 3-21 shows recorded intensities denoting $I(x, y)$ from ten Mykonos shots. Each has a slightly different timing of the laser so the frames span the window in which holography is suitable. Tentative inspection reveals the latest holograms have the worst contrast, in agreement with the descriptions above.

Streaked Visible Spectroscopy:

Streaked visible spectroscopy was fielded for the first time in the Mykonos facility. A 200-um-core fiber relays emissions from a target to the spectrometer ~ 100 m away. The spectrometer is an imaging spectrometer with a 200-um-slit, and 150 lines per mm grating, which disperses an approximately 400-nm-wide spectral band onto a streak camera. The diagnostic was fielded on three campaigns. For the first campaign, the collection optics relied a simple broadband fiber-optic collimator (Thorlabs part # RC12SMA-F01).

This yielded the data in Fig. 3-22. The oscillatory behavior in Fig. 3-22.a-d is due to electron self-bunching in the streak tube electron optics, and is therefore an artifact of the instrument response.

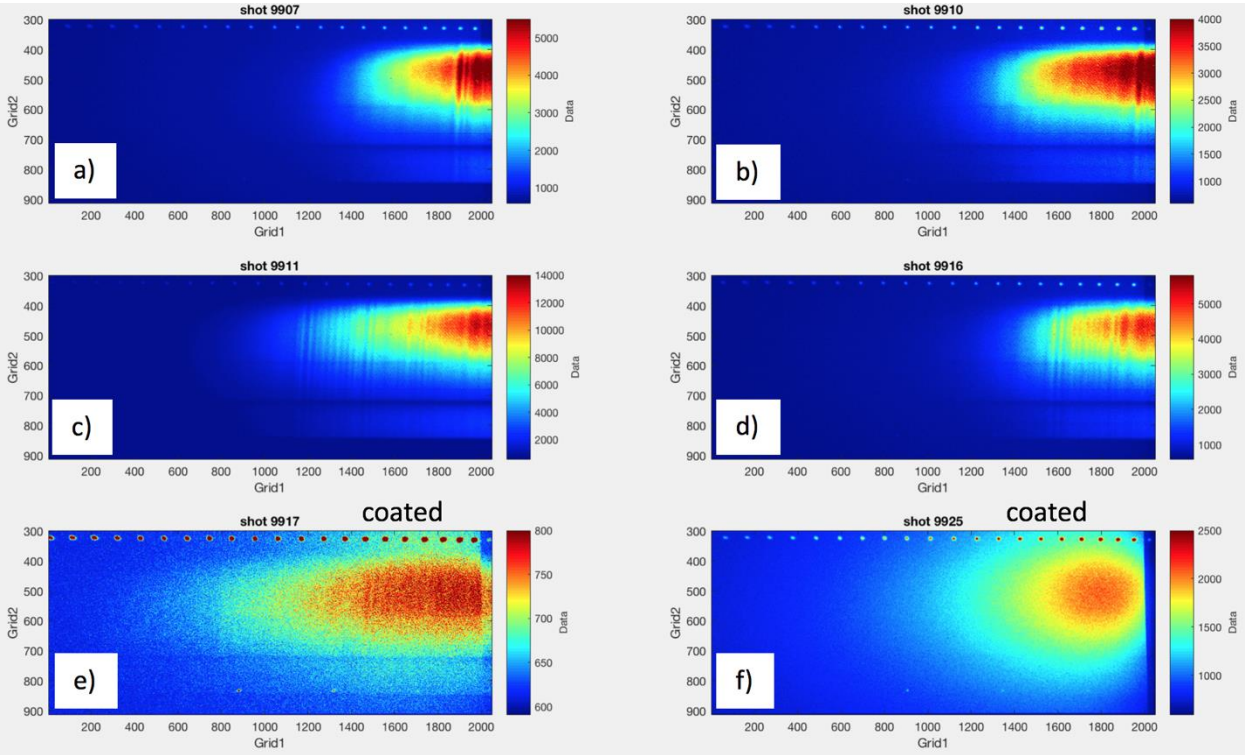

Figure 3-22. Streaked visible spectrograms corresponding the uncoated (a-d) and coated (e-f) 800 um aluminum wires driven by the Mykonos LTD. Grid 2 is in wavelength (nm), and Grid 1 is time. The time axis spans 100 ns. Work to calibrate time axes was not performed as numerous serious issues were identified in the diagnostic implementation, ranging from a lack of absolute calibration, inconsistent collection amplitudes, and improper spectrometer alignment (f). Color denotes counts, time increases to the right.

Given that the light emitted from a target is not collimated, new collection optics were designed. An $f/1.7$ optical assembly, with unity magnification, was custom designed to image light from rod surfaces into a $200-\mu m$-diameter fiber (see Fig. 3-23). This indicates that derived spectra correspond to spatial averages over the imaged $200-\mu m$-diameter patch of a barbell surface.

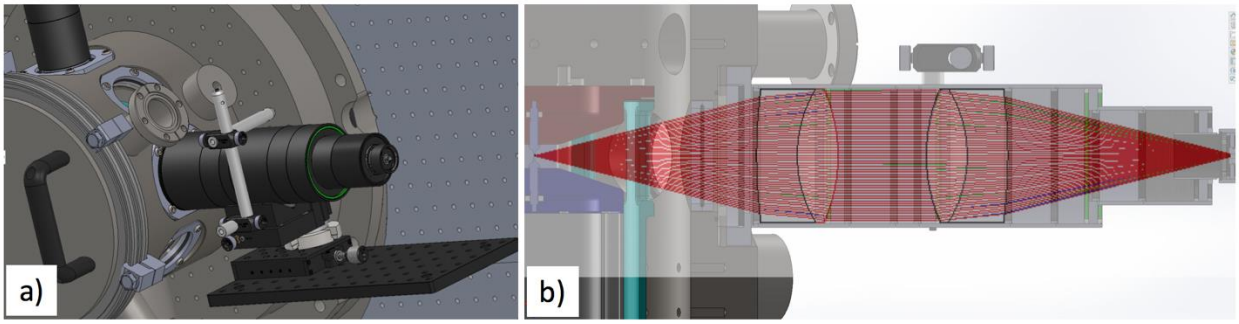

Figure 3-23. a) A 3D CAD model of the SVS optics assembly, on a kinematic alignment stage and b) A polychromatic Zemax calculation overlaid on a 3D CAD model, representing the final SVS optical assembly layout. The calculation relied on the exact lenses used in the system, and couples to a fiber on the right side of b). The fiber is hundreds of feet long, and relays the light to the spectrometer. An $f/1.7$ system is essentially the sharpest collection optics possible without bringing optics into the vacuum chamber, and the system was designed to collect as much light as possible.

Three issues were identified on campaign 2, identified as the 'haze', shutter, and calibration issues. For the first issue, there was an unexplained, variable background count on SVS frames. It appeared at ~300 nm, and therefore wasn't coming through the fiber. The haze issue was a variable background spanning the whole image (even pixels which should denote 200 nm light, so not light from the fiber). In the SVS room, there are multiple, nominally identical spectrometers coupled to streak tubes and an imaging system, identified as SVS 1-5. Due to the haze, we switch from SVS 5 to SVS 4, and the haze issue disappeared. The streak tube from SVS 5 was sent back to the manufacturer for repair.

The second issue is related to the shutter. The SVS systems require a trigger ~ 100 ms early to open mechanical shutters allowing light through the spectrometer. For this campaign, there was no available trigger from Mykonos with sufficiently low jitter to open the shutters, and a technician was required to manually open them during the LTD charge sequence. This admitted many seconds of integrated room lights, whether through the fiber or in the SVS room. This left a residual signature in the data that was difficult to subtract, given its variability. We learned after a few shots that all room lights had to be off.

The third issue was a calibration issue. A genuine 1100K blackbody oven was used to absolutely calibrate the diagnostic, with an identical optical configuration as during an experiment. It was discovered after data was collected that this blackbody carries very little spectral power < 500 nm, and therefore couldn't be used to calibrate the full 400-700 nm spectral range, but only 600-700 nm. In addition, the blackbody was taken with room lights on. The results of analysis are shown in Fig 3-24, where the comparatively bad blackbody fit (blue) first cued an error in the calibration.

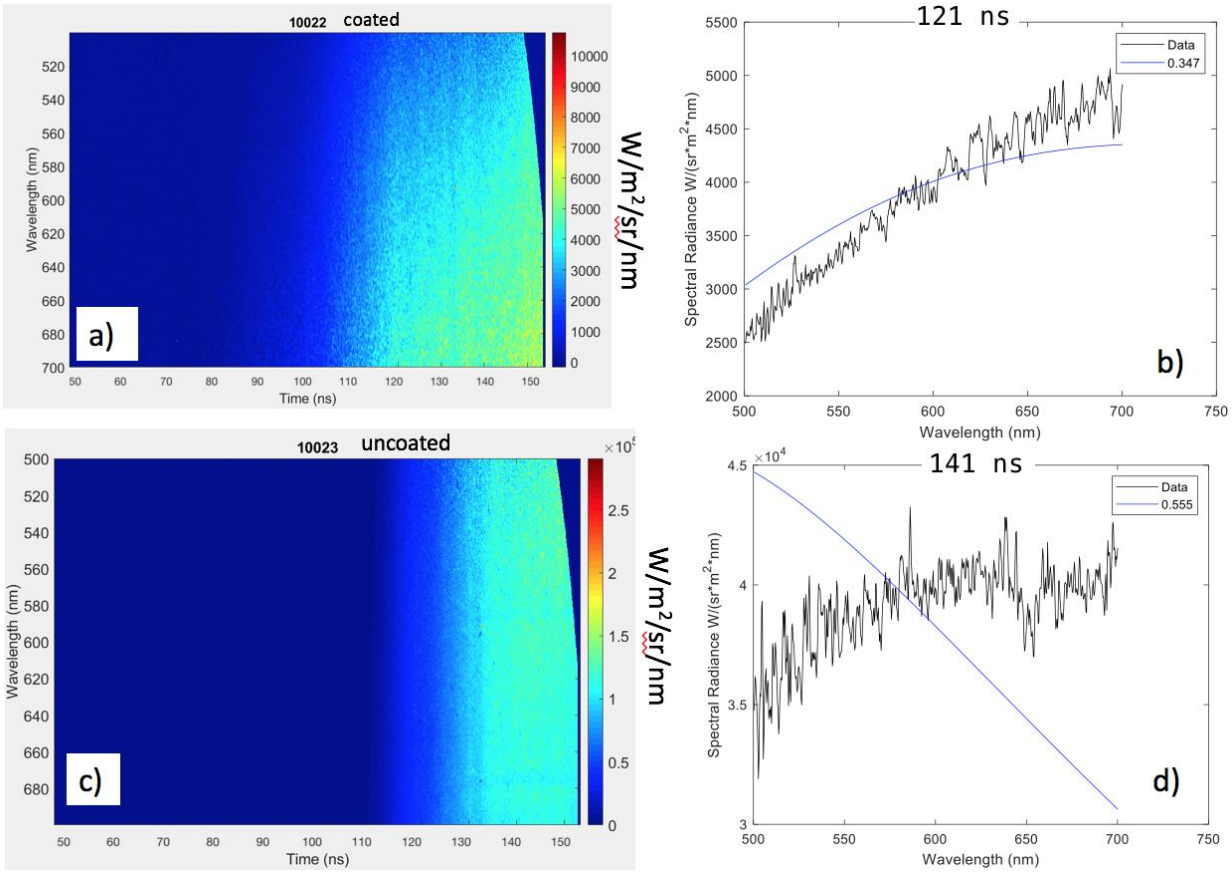

Figure 3-24. Absolutely calibrated spectra from coated a) and uncoated c) surfaces, together with lineouts at two different times b) and d), from a) and c) respectively, denoting the spectrum. Blue lines are blackbody fits to the data, with best temperature estimated in eV in the legend. The data has been dispersion compensated, accounting for the multiple ns dispersion delay associated with the multi-hundred-ns fiber optic cable carrying data from Mykonos to the SVS room – this explains the null-count curved band in the top right of a) and c). The bad fit in d) signals an issue, believed to be related to unblocked room lights. There are no clear spectral signatures associated with absorption or emission lines.

To address the three identified problems, SVS 4 was used, a new digital delay generator was acquired to provide a sufficiently early trigger to open the mechanical shutters, and a broader band calibration source was acquired. This calibration source is a Gooch & Housego calibration standard which emulates the color temperature of a 3000K blackbody, but with an emissivity of 1.2% – that is, the relative proportions of different colors are preserved, but the curve is shifted vertically so only 3 $W/(m^2 \cdot nm \cdot sr)$ of 700 nm, rather than the 250 $W/(m^2 \cdot nm \cdot sr)$ of a true blackbody is emitted. The provides for sufficient power in the < 500 nm range so data may reliably be calibrated, relative to a true 1100K blackbody. Finally, the LCA door was kept closed, and all lights within it off during the calibration portion of the experiment.

The new delay generator has ~80 ns of jitter with respect to the current pulse. It was first thought that we could use the 200 ns sweep and center the data we expect, so as to capture it despite the

jitter, but this was often unreliable, and the plasma that forms after peak current compromised the data (see Fig. 3-25, below).

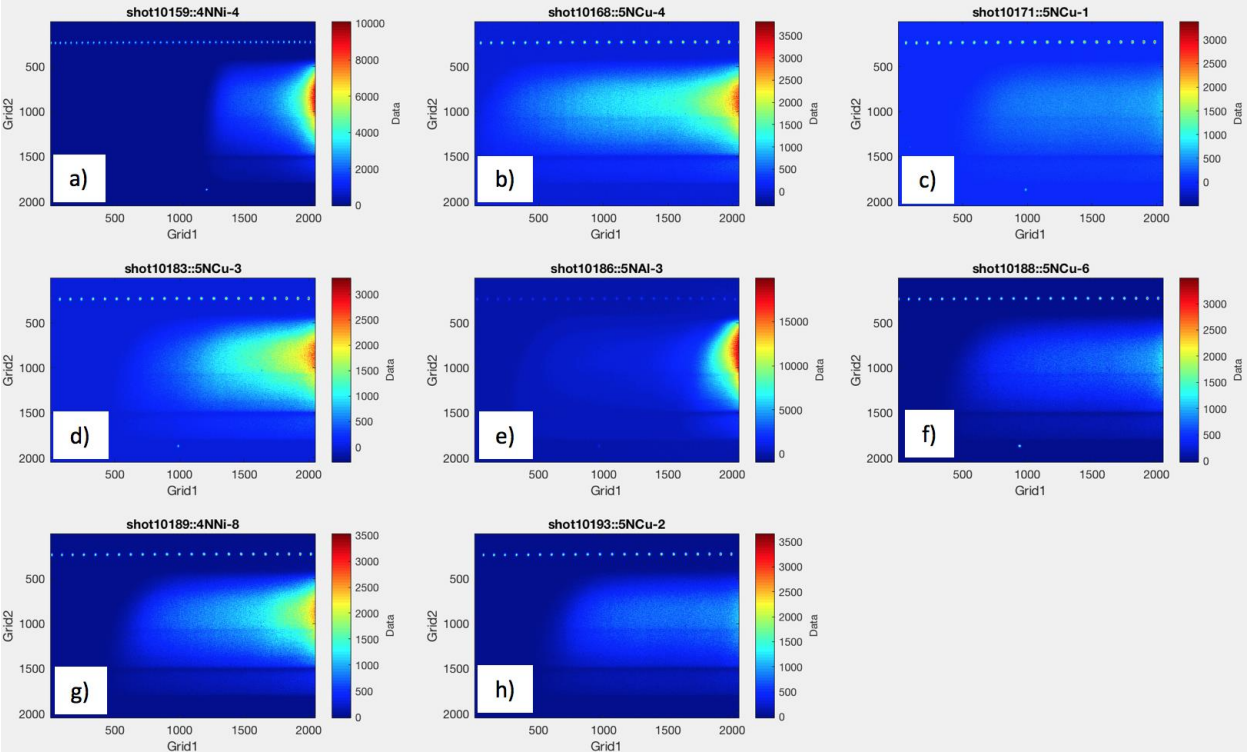

Figure 3-25. Streaked spectra from various coated ~800 um rods driven by Mykonos current, with titles corresponding to shot number and metal composition. These represent loads which did not form plasma. The streak width is 100 ns. The bright dot that appears at the bottom of the image (at Grid1 ~ 1000, and Grid2 ~ 1900) corresponds to a timing fiducial pulse used to cross-correlate the spectra to the Mykonos current. The 200 MHz comb at the top of the image corroborates the temporal scale. These spectra are expected to be fully analyzable. The dark band at Grid2 ~ 1500 denotes the separation between 1st and 2nd orders, and the dark band at Grid2~1100 is expected to be an absorption line in the silica fiber, further evidenced by its persistence when varying metal types.

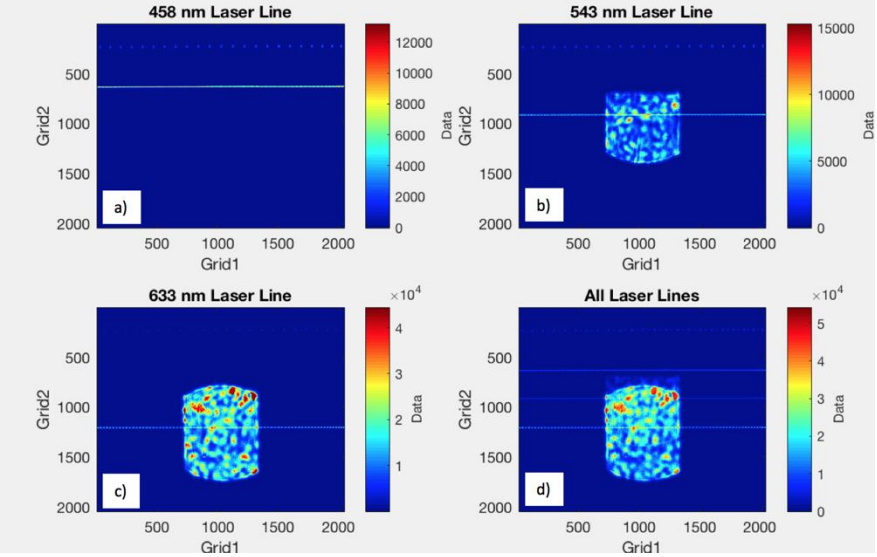

Figure 3-26. Spectral calibration images for SVS. In between Mykonos SVS shots, the system is used for other experiments on PECOS, and the spectrometer grating may be rotated or have fewer lines per mm, so these laser line streaks are taken for every shot. These images permit calculation of the spectral resolution.

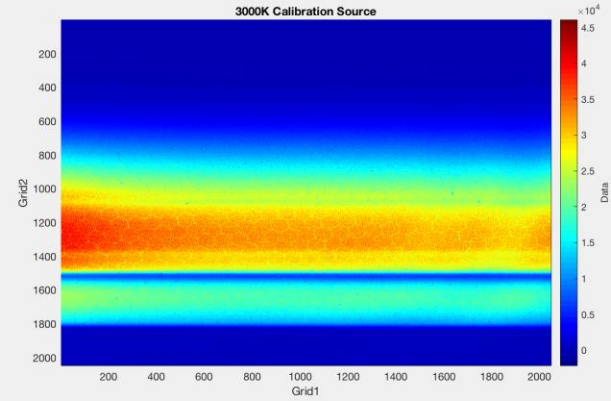

Figure 3-27. Streaked spectrogram of 3000K tungsten lamp calibration source, over 8 seconds, to absolutely calibrate the spectral throughput. The calibration source was set up so the collection optics image the plane of the opening to the integrating sphere attached to the tungsten lamp, determined by backlighting with a laser. The integrating sphere simulates a Lambertian source, and the room lights were off, so the optical target emulates a known spectrum and absolute intensity in a manner robust to defocusing. The window and debris shield were not in the calibration setup, and therefore will have to be removed from the data manually. It is not clear why time-variation exists across the 8 second window.

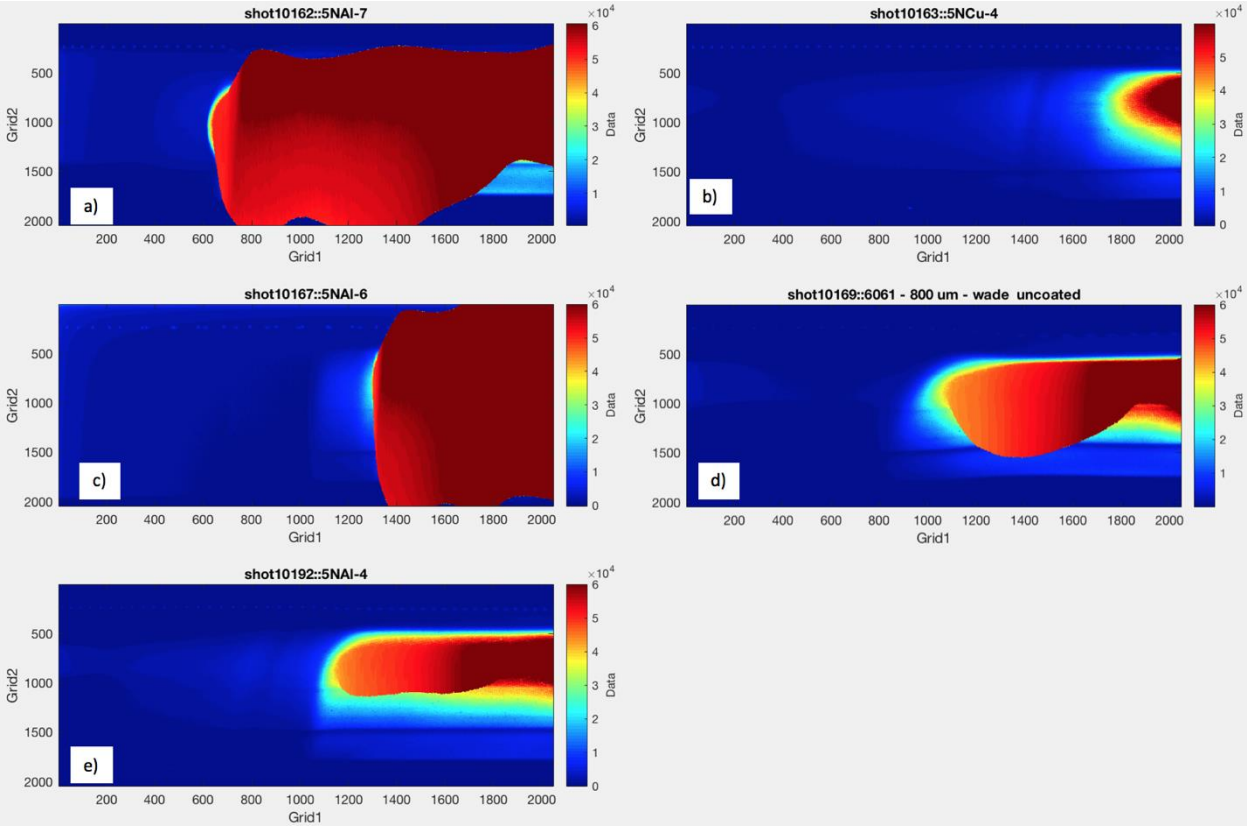

Figure 3-28. Supplemental streaked spectra demonstrating electron optics warping. a)-e) are 200 ns. If too bright (approximately when the CCD saturates) a source is incident on the photocathode, the resulting electric field from the burst of photoelectrons is sufficient to perturb the electron optics, the resulting electron trajectories, and therefore the streaked spectra, in a non-correctable manner. This can be seen best in a) and c), where the 200 MHz fiducial comb at the top of the image is distorted. Saturated counts typically spill over into nearby pixels, and the image unusable.

If the source it too bright late in time, the non-linearity in the electron optics yields counts distributed over the entire sensor, compromising the data at early time. The surplus brightness typically occurs when plasma forms for one of two reasons: after peak current the barbell typically forms plasma. The second case is if the barbells forms plasma. Due to pure Aluminum's extreme softness, fabrication tolerances landed very widely, plasma often formed, and few successful spectra of aluminum were obtained. Another step to resolve the warping involved abandoning the 200 ns window and setting the streak timing so peak current is after the streak terminates.

Although significant analysis remains, it is already apparent that the spectra produced in these experiments is continuous, and therefore the metal remains optically dense for the visible spectral range. Further modelling remains, but it is likely the inference of a continuous emission spectrum will stand. It is further anticipated that given the spatial heterogeneity of the metal evolution in the 200 μm spot size (based on ICCD imaging), a single blackbody temperature will inadequate model the obtained spectra.

Load Bdots:

Inspection of the anode ‘castle’ (teal object in Fig. 3-29) and cathode ‘stalk’ (central, hollow grey below blue cathode in Fig. 3-29) after refurbishments yielded evidence of arcing at the bottom of the castle to the cathode. This arc would parasitize current from the load, and at a location where which existing bdots would not measure any reduction in current. Therefore, new bdots were designed. They were as close to the load as possible.

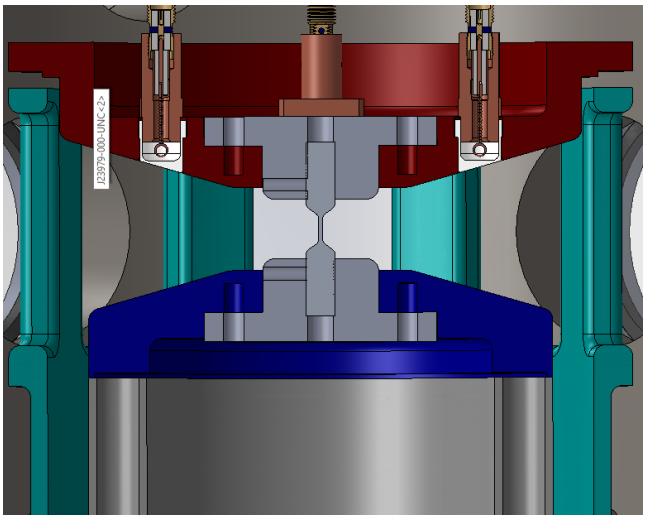

Figure 3-29. Solidworks model of the load hardware, showing the load bdots recessed behind the white PEEK ‘caps’ (to protect from load debris). There were 4 bdots.

For the first two campaigns, approximately 10-20% of shots were compromised due to surface flashover. With the use of these new ‘buttons’, that number fell to < 5%.

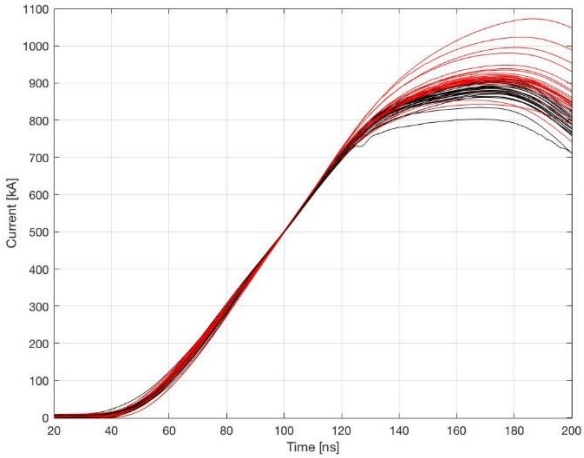

Figure 3-30. Currents inferred from bdot measurements over 27 shots immediately after the insulator (black) and at the load (red), all at the same azimuthal location. Time have been shifted so 500 kA occurs at 100 ns.

Traces in Fig. 3-30 indicate the currents inferred from load bdots are not lower than those from bdots at the insulator. In fact, they are often higher, suggesting a source of noise on the bdots.

This is likely common-mode noise on the load bdots, removable by averaging over oppositely wound bdot polarities. The most accurate determination of current will rely on azimuthal averaging as well. Fig 3-30 suggests that the arcing inferred from debris on electrodes in the transmission line is due to arcing that occurs after peak current, and therefore that the current inferred to have gone through the load by bdots back at the insulator did, in fact, go through the load.

4. PDV DIAGNOSIS OF SURFACE EXPANSION

Overview of PDV paper & PDV diagnostic:

Historical determination of thick conductor dimensions throughout an electrical explosion has relied on shadowgraphy, streaked shadowgraphy, and streaked self-emission. The data is typically coarsely resolved, with > 15 μm spatial and temporal resolution ranging from $1 - 2\ ns$ (streaked) to worse than $5\ ns$ (single frame shadowgraphy). To improve on this, a new diagnostic was designed – photonic Doppler velocimetry. This diagnostic relies on evaluating the frequency of light reflected from the metal surface while it explodes, and determining the frequency shift due to the Doppler effect. It can diagnose velocities down to $\sim 10\ \mathrm{m/s}$ with better than ns precision, and requires only a small fraction of light reflected from the metal surface.

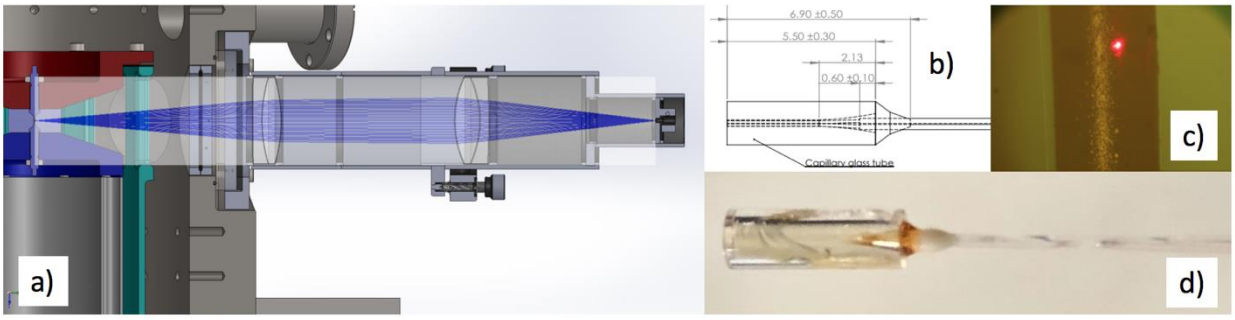

Figure 4-1. a) Zemax calculation overlaid on a Solidworks model of the Mykonos vacuum chamber, demonstrating a simple achromatic 2-lens system with unity magnification that maps the surface light to a fiber optic assembly (b & d). The blue lines represent ray optic calculations at 1550 nm and NA = 014 (matching single mode fiber), relying on lenses that are also able to focus 633 nm light as well. b) CAD drawing of the glass capillary tube (dimensions in mm) that contains fiber optics and couples to right side of a), c) an image of the minimum achievable 633 nm spot size on an $800 -$ μm rod in chamber and d), an optical image of a glass capillary tube, with a polished left face and three fiber optic leads exiting on the right side of the tube, which in principle allows for multiple channels of data to improve noise statistics.

A set of 36 $800 -$ μm $-$diameter aluminum rods was decomposed into sub-sets of 6, each of which was given a different surface finish treatments and/or dielectric coating thickness. Each rod was then pulsed with Mykonos, and the surface velocity was diagnosed using PDV.

The results (a draft manuscript is attached in Appendix A) demonstrate the PDV diagnostic can provide a continuous time-record of the surface velocity. This permits evaluation of when the surface metal melts and enters the vapor dome, together with information of how much time-integrated expansion has occurred. The disappearance of the reflected light is correlated with the formation of plasma on rod surfaces, and therefore the diagnostic may also be used to infer plasma formation time.

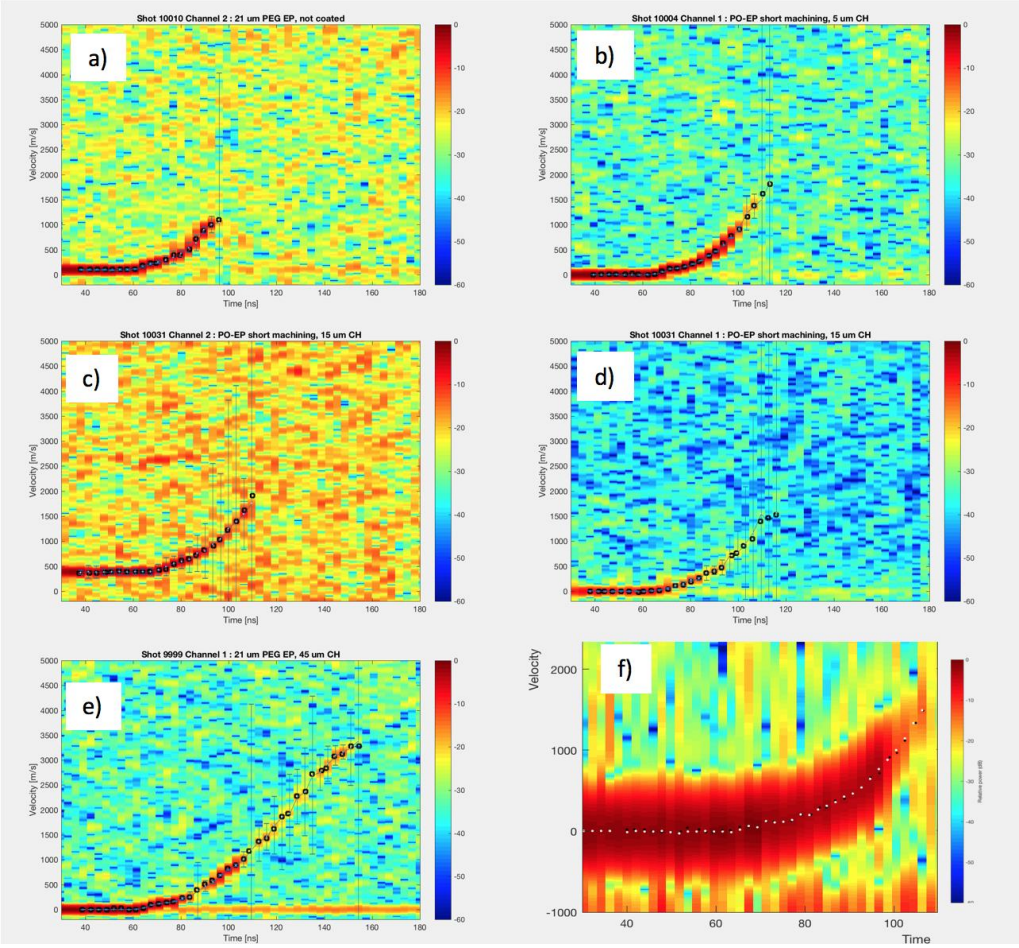

Figure 4-2. Example spectrograms from campaign 1 from uncoated (a), 5-um-coated (b), 15-um-coated (c,d) and 45-um-coated (e) 800-um aluminum rods. (a-e) were processed with 9.6 ns Fourier windows reported into 3.2 ns columns, while f) corresponds to 1.6 ns Fourier windows in 1.6 ns windows of the same underlying data as b). The noise floor is $\sim 10\ dB$ higher, and the frequency uncertainty many factors larger in f), demonstrating that choices of window size affect spectral noise characteristics and spectral width. The black circles (or dots, in f)) represent the maximum as selected by eye, and the white circles (in a-f, but most visible in f) denote the local maxima within 20 frequency bins. This process was used in the appended draft publication, due to window reflections. The error bars in (a-e) are a measure of the velocity uncertainty intra-column, given as a FHWM of a Gaussian with breadth determined by the number of standard deviations out of the noise of the maxima selected by the above process.

A second implementation of the diagnostic was fielded. The principle change was a dramatic increase in the power of the probe laser, from 35 mW used to collect the data in the appended paper, to 200 mW for second round of experiments. Safety controls were implemented, and are incorporated in an approved Safe Work Plan. Data returns were significantly improved, as seen in Fig. 4-3.

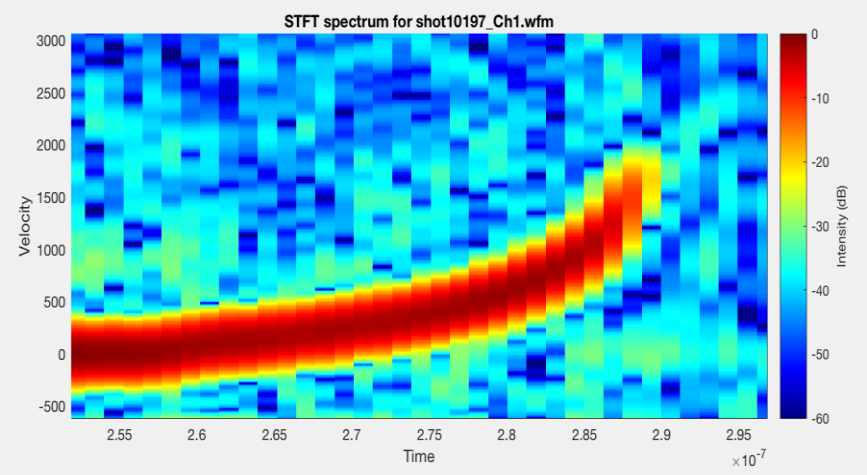

Figure 4-3. Example spectrogram from bare diamond-turned aluminum rods with diameter 800 μm and ~10 nm surface roughness. The vertical axis is in m/s, the horizontal in seconds, and although the time has not been shifted to a physically meaningful one, the appended draft suggests the first non-zero velocities appear for a load of this type when the Mykonos current pulse reaches 200 kA. The data are consistent with a quasi-linear ramp, then an increase in acceleration beginning $\sim$20 ns after first motion. New behavior apparent in this better-quality data are non-linear structure during 'liftoff' (256 – 262 ns) and a spectral broadening of the signal before cutout (~285 ns). Further analysis may quantify these and allow attributing them to physical phenomena. For example, the latter phenomenon suggests a broadening of the velocity distribution carried by reflective matter within the PDV spot size.

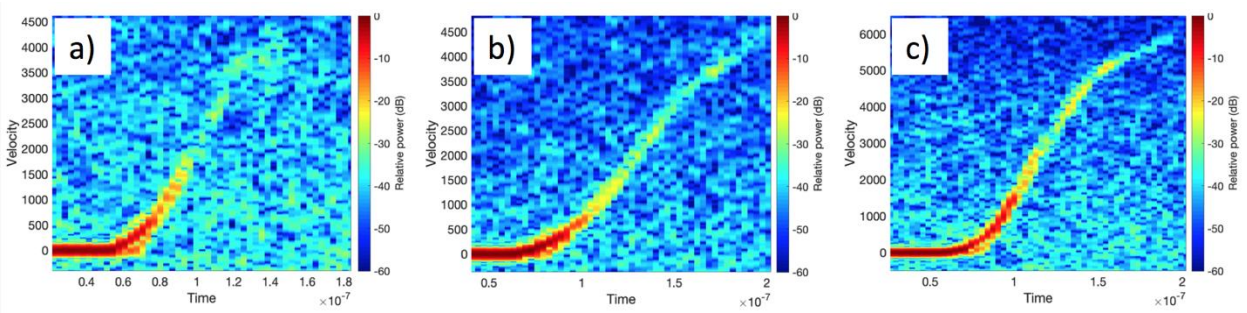

Figure 4-4. Spectrograms of approximately 800 μm aluminum (a), copper (b), and nickel (c) barbells, coated with 45 μm of dielectric and driven by the Mykonos current pulse. Time is in seconds, and the axis has been shifted so 100 ns occurs when the rod is carrying 500 kA. The vertical axis is in m/s. Note the similarity of the copper and aluminum trajectories, but the significantly faster nickel trajectory.

The persistence of PDV signals in Fig. 4-3 relative to Fig. 4-4 is likely due to the ultra-smooth surface. For future implementations, the best quality PDV signals occur for ultra-smooth surfaces and large incident powers ~ 200 mW, together with $\sim f/4$ optics. Alignment occurs first with a visible fiber-coupled laser diode (to ensure optics are focused on the rod), then with a low-power ($\sim 1\ mW$) 1550 nm laser and photodiode on the receive channels of the fiber optics. With this diagnostic, there is a fundamental tradeoff (technically, an uncertainty relation) between frequency

and time resolution that is mediated (in small and subtle ways) by analysis choices relating to FFT window duration, zero padding, and windowing functions. Although interpolation and fitting techniques may recover lost resolution due to bad analysis choices, the Gabor limit of harmonic analysis $4\pi\ \Delta f \Delta t > 1$ cannot be beaten.

5. EXPERIMENTS STUDYING DIELECTRIC COATED RODS

Campaign 1 -- METI 1:

Preliminary experiments in this campaign focused on confirming that the Mykonos platform could reproduce experimental results seen on the Zebra generator. Targets were uncoated aluminum 6061 rods, and coated aluminum 6061 rods. Since Mykonos was expected to produce 4/5 the peak current, rod radii were decreased to 4/5 that from previous Zebra targets (which were 1 mm in diameter). Previous data indicated that dielectric coatings improve the ability to diagnose thermal perturbations.

Since the ETI is believed to couple strongly to surface topography and metal composition, careful attention was paid to metal surface preparation and characterization. All rods in campaign "METI 1" (where METI is shorthand for Mykonos ETI) were subject to an electrochemical surface preparation procedure called pulse anodizing. This process removes very little bulk aluminum, but preferentially removes resistive inclusions [xxxi]. Images of a $100\,\mu m \times 100\,\mu m$ patch of the barbell's surface before and after pulse anodizing are shown in Fig. 5-1, taken with a white light interferometer. Inspection of the statistical metrics of the surface indicate it is rougher after the pulse anodizing procedure, despite a visually smoother appearance.

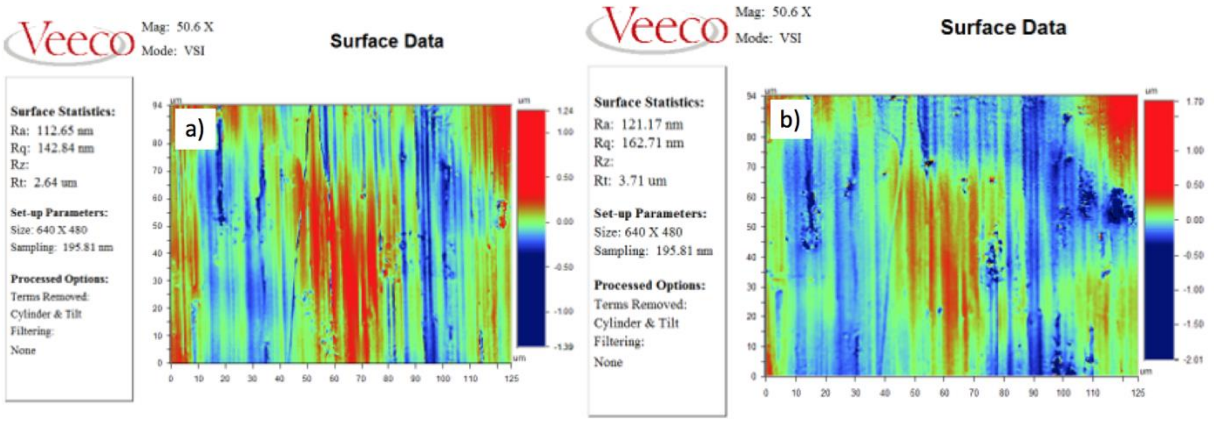

Figure 5-1. a) Pre-electropolished surface of an aluminum 6061 barbell and b) post-electropolished surface of the exact same region of the same barbell.

Numerous non-metallic, resistive imperfections are apparent in Fig. 5-1. These have been identified through energy dispersive spectroscopy as oxides of Silicon, Magnesium, Calcium, Iron, and Manganese. Since these are the elements which form the specific aluminum-6061 alloy, these imperfections (called inclusions) are suspected to be precipitates of the super-saturated liquid aluminum that is formed into raw stock. They are preferentially removed by the electropolishing procedure.

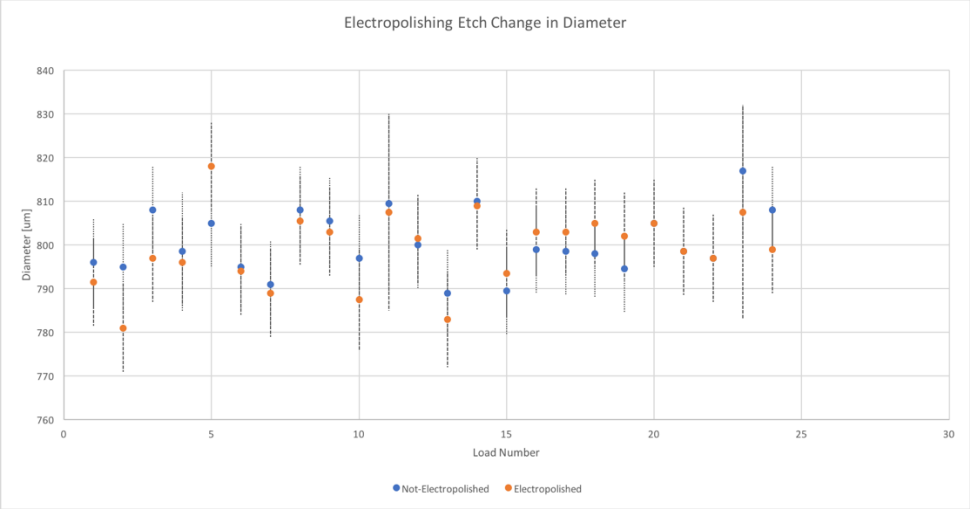

Figure 5-2. Diameters of rods before and after electropolishing.

Differences between optical images of electropolished rods and non-electropolished rods do not sufficiently exceed intrinsic uncertainties in the diameter-measuring-procedure to determine the amount of matter removed (if smaller than ~ 20 μm). Therefore, the amount of matter removed from the radius by pulse-anodizing was ultimately inferred from electropolishing parameters like voltage, duty cycle, and ON time as 600 nm.

An example target is shown in Fig. 5-3, where the Parylene-N coating is shown on the central 800 um diameter portion of the rod. Initial specification was for 70 ± 5 μm of dielectric (to match historical experiments), but measurements indicate the thickness was closer to 45 ± 5 μm of dielectric. For continuity, all dielectric coating thicknesses were specified to this, new, thickness. Follow on measurements, on subsequent batches of dielectric-coated rods, were consistent with the 45 ± 5 μm specification. The Parylene-N is repeatable across multiple barbells (Fig. 5-3.b-d).

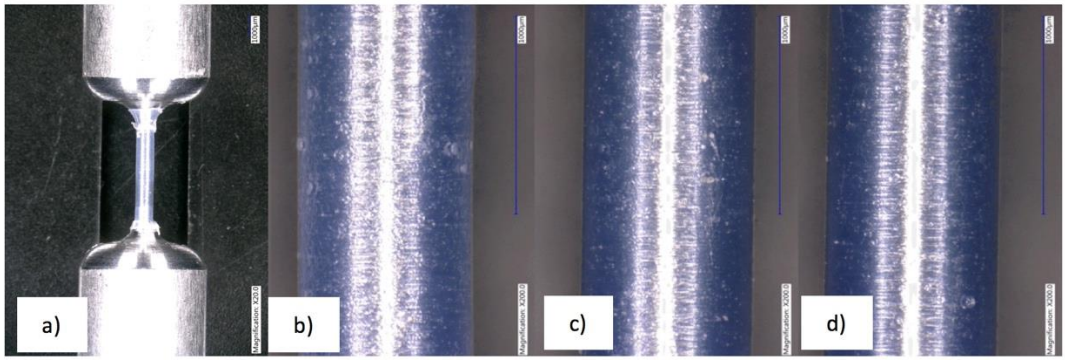

Figure 5-3. Example optical microscope image of targets, after Parylene-N coating. a) A low magnification image where the central, thin portion of the rod in the image is 800 μm in diameter and coated in Parylene-N, and the wide portion is $1/4''$ in diameter and slip-fits inside the electrode bores. b-d) Optical microscope images of only the central 800-um-diameter portion of different barbell, after having been Parylene-N coated – note the machining structure is visible through the dielectric coating.

These targets were coupled to the Mykonos LTD. ICCD images from this first round of experiments are shown in Figs. 5.4 (uncoated), Fig. 5-5 (coated), and Fig. 5-6 (coated). Data indicated thermal overheating of the rods consistent with Zebra results, confirming that the Mykonos facility could fulfill necessary conditions for ETI experiments.

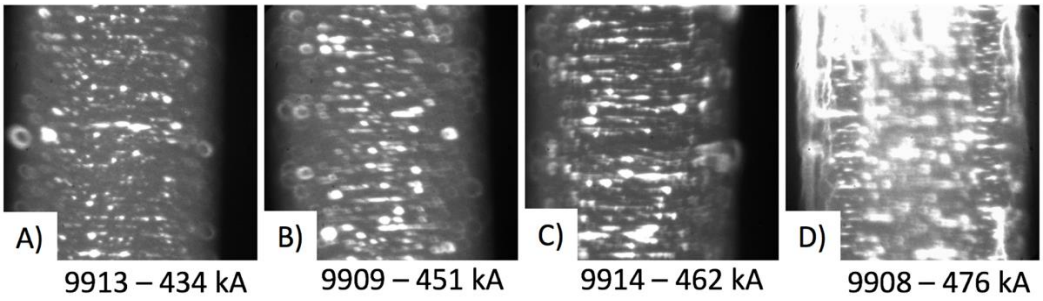

Figure 5-4. Images of different uncoated $800-\mu m$-diameter Aluminum-6061 rods. 2-ns gate. Note the apparent anode-cathode asymmetry of filamentation, a phenomenon which has repeatedly occurred but not been explained.

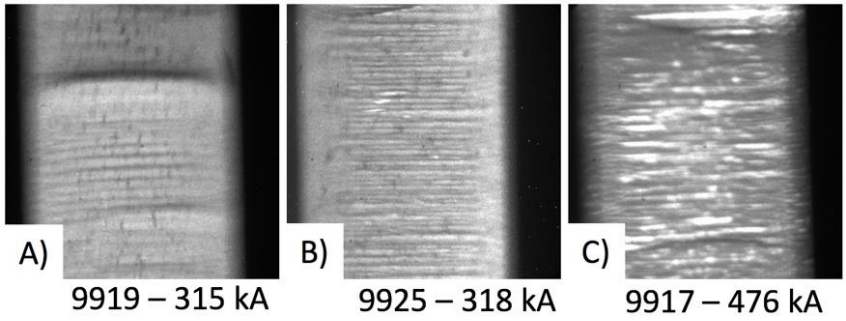

Figure 5-5. DH 334 Images of 800-um rods carrying current, under 45 μm of Parylene-N coating. Images contrast has been normalized for presentation purposes, and absolute differences in emission cannot be determined without absolute calibration.

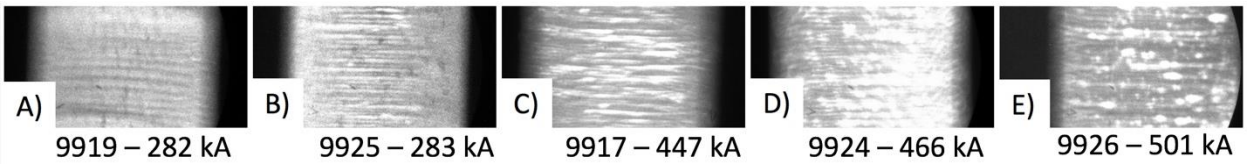

Figure 5-6. DH 340 images of coated loads, under 45 μm of Parylene-N coating. Images contrast has been normalized for presentation purposes, and absolute differences in emission cannot be determined without absolute calibration.

Images taken with the ICCD diagnostic on this campaign had a magnification of M~10, and 3-5 um spatial resolution. Two Andor-manufactured ICCDs were used, with model numbers DH334T-18U-73 and DH340T-18F-E3. Images demonstrate azimuthally-correlated thermal perturbations on rods carrying $200-500$ kA. These perturbations are more azimuthally correlated (but smaller amplitude) under dielectric coatings than for bare metal surfaces.

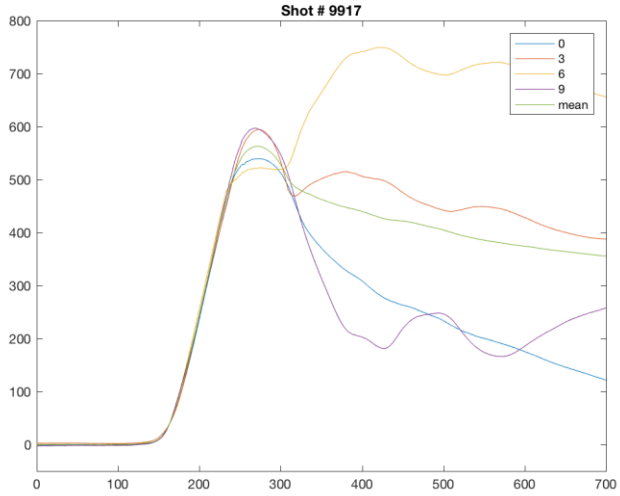

Figure 5-7. Inferred electrical current delivered to the load for shot 9917. The y-axis is in kA, and the x-axis in nanoseconds.

Circuit calculations indicated that given the load inductance, a peak current closer to 900 kA should have been delivered to the load, but a typical current from the first campaign (seen in Fig. 5-7) suggested a smaller 550 kA was delivered to the load. This was achieved with a 60 kV charge voltage, the highest achievable without pre-fires. Post-campaign refurbishment of the LTD cavities revealed bad charge resistors, which were likely responsible for the comparatively low achievable charge voltage.

Campaign 2 -- METI 2:

After validating that the Mykonos LTD could supply a sufficient current pulse to investigate ETI, a second campaign was designed to focus on the effects of surface topography on the growth rate and terminal amplitude of perturbations driven by ETI, under coatings. New diagnostics included SVS, PDV, a 12-frame imager, and a single diode element to observe time-resolved visible emissions. The campaign consisted of approximately 40 targets, 36 of which were coated with 45 ± 5 μm of Parylene-N.

The LTD cavities were charged to 80 kV for this campaign and the salinity of the water resistor was increased, lowering the resistance of the load. These changes allowed a significantly higher peak current (seen in Fig. 5-8) to be achieved. The inductance associated with changes in target dimensions does not noticeably affect the delivered current to a target.

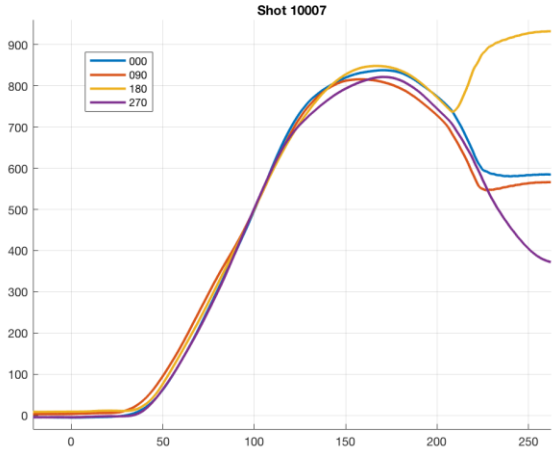

Figure 5-8. Bdot traces corresponding to 4 azimuthal locations 14'' upstream from target chamber center. The vertical axis is in kA, and the horizontal in nanoseconds. The blue trace denotes the current at the 12 o'clock position, and the red trace at the 3 o'clock position. This was a typical current trace for this campaign. Note that the signals deviate appreciably around 210 ns, when the insulator flashes over, the load is crowbarred, and the voltage changes rapidly – the signals are not reliable after this occurs.

To control the surface finishes of the metal, numerous strategies were implemented. The feed rate of the lathe was specified so the axial pitch of the cutting bit with respect to the barbell axis was controlled. This provided for two classes of surface finishes, identified as short wavelength machining and long wavelength machining, as seen in confocal microscopy in Figs. 5-9 and 5-10 respectively. Confocal images are of a curved surface, with concomitant loss of data as the barbell surface falls recedes from the confocal objective (presumably because the scattering amplitude of confocal light off a metal surface is peaked at π radians and falls off rapidly for the non-retroreflected light). This can be partially compensated for by fitting and subtracting a cylinder from the data ([xxxii]), but confocal data from far the rod axis is clearly of a different quality than that along the axis.

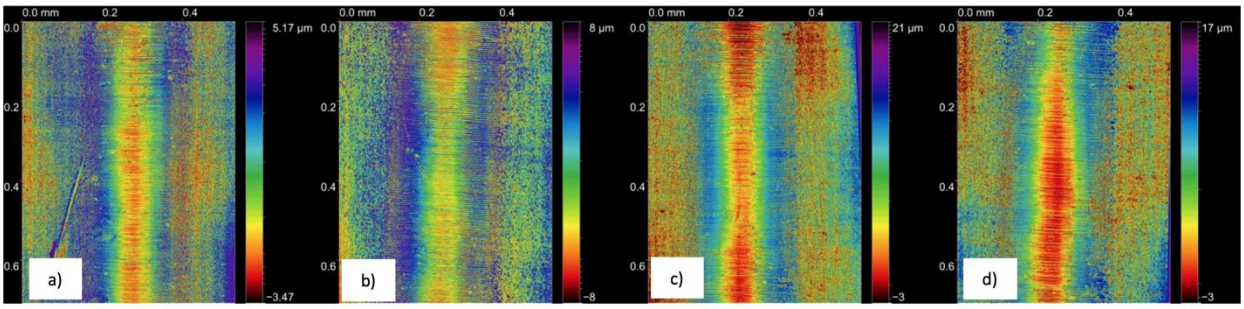

Figure 5-9. A representative set of 4 barbells in the short machining class, fabricated using a 5 µm on the lathe. The vertical direction is parallel with the rod axis. Fourier analysis indicates the dominant mode is in-fact 5 µm, consistent with the pitch of the lathe. This indicates that the surface topography can indeed be controlled by the machining parameters, even without pre-programming of the machining.

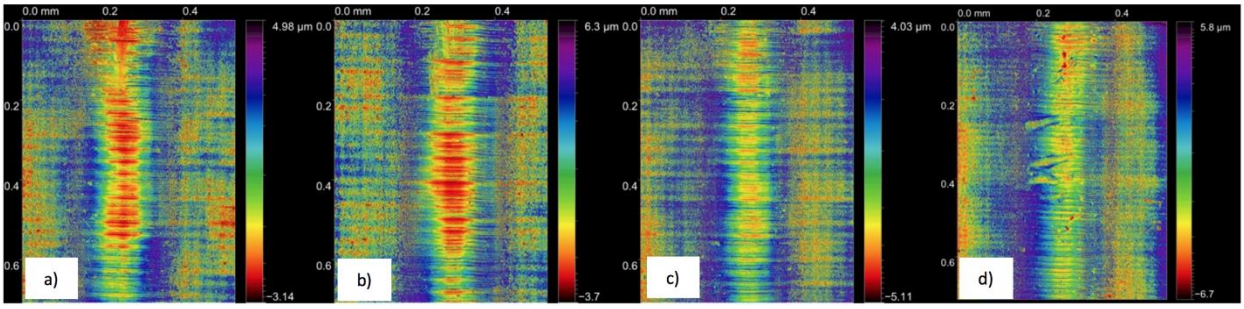

Figure 5-10. Barbells in the long machining class, fabricated using a 30 μm pitch on the lathe. The vertical direction is parallel with the rod axis. Data have already been subtracted from a cylindrical fit, and color axes denote ~ 10 um.

Rods were also subjected to various electrochemical polishing techniques. These are described in detail in Appendix A, but are breifely described here. Pulse-anodizing, or Pulsed-Oxide Electropolishing (PO-EP) removes ~ 600 nm of material, and preferentially non-metallic imperfections in the surface. It's effects can be seen in the third panel of Figs. 5-11 and 5-12. Higher magnification SEM images of the results of PO-EP can be seen in Fig. 5-13.a-b where sub-micron scale etching is visible. The variety of surface finishes for what should have been identically processed barbells demonstrates either that the processes were not identical, or electropolishing itself is not a repeatable process.

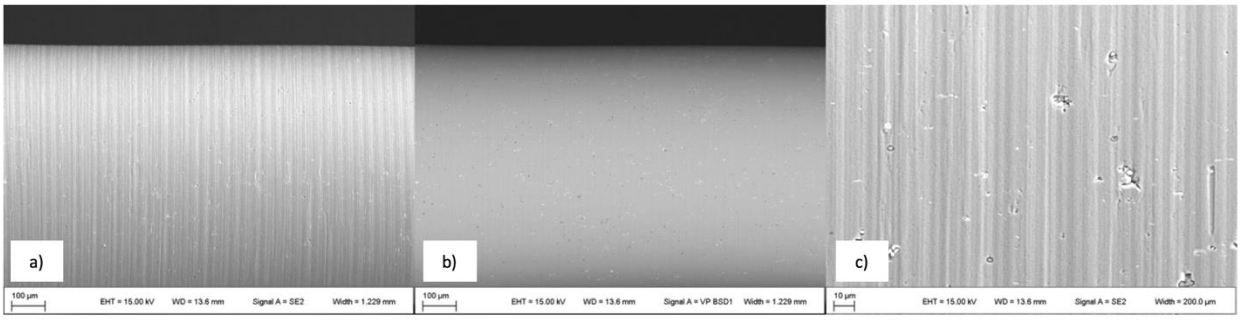

Figure 5-11. SEM images of a rod with 5-um machining. The highest-magnification image shows the result of pulse-anodizing the surface – where inclusions have been preferentially removed but the surface topography is comparatively unmodified. The first panel was taken using an SEM in secondary electron (SE) collection mode, the second in backscattered electron (BSD) mode, and the third in secondary electron mode. SE and BSD are sensitive to topography and electron density respectively. BSD images indicate where metallurgical defects reside, an important factor that may influence ETI growth.

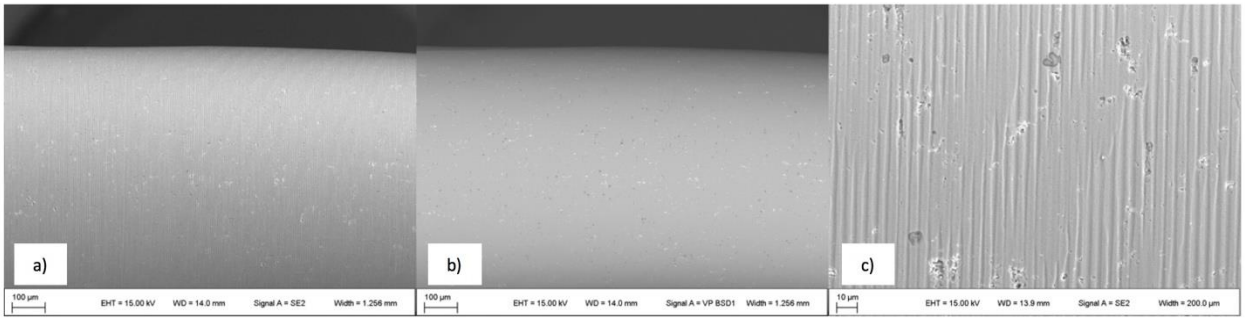

Figure 5-12. SEM images of a rod with 5-um machining. Most rods demonstrated some deviation from cylindricity, apparent in the top right of the first panel. Since visible imaging is restricted to a smaller portion of the rod surface, these deviations are not expected to appreciably modify the observed ETI dynamics, although this has not yet been quantified.

The other electropolishing method, identified in Appendix A as PEG-EP, is more aggressive. It was implemented to remove 21 μm from the radius of rods and entirely remove any residual surface machining features. It was largely effective, but nonetheless leaves a heterogeneous surface, with exposed metallurgical inclusions, multi-micron voids in the metal, differences in height suspected to correspond to different grain orientations, and micro-etching along grain boundaries (Fig. 5-13.c-d). These data show how varied the microscopic environment of an alloyed metal surface can be – and demonstrate the unique challenge of studying the initial conditions for ETI initiation and development.

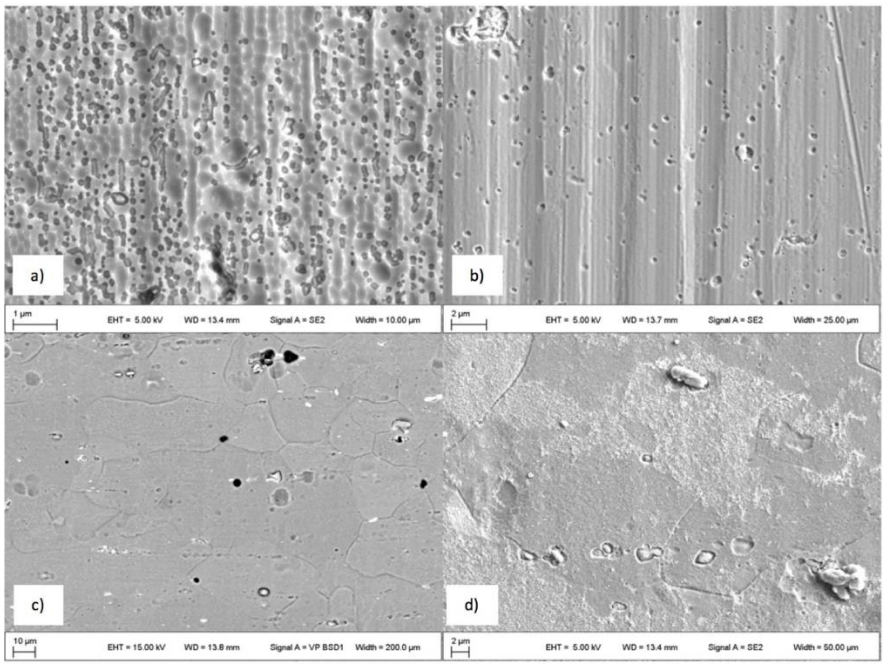

Figure 5-13. SEM of PO-EP (a-b) and PEG surfaces (c-d) – electropolishing leaves a heterogeneous surface. Micro-etching visible in d) along grain boundaries. a-b) and d) are SE images at 5 kV, and c) BSD at 15 kV. Lower voltage SEM SE correspond with higher-resolution imaging, so d) will show more surface structure than an equivalent image at 15 kV.

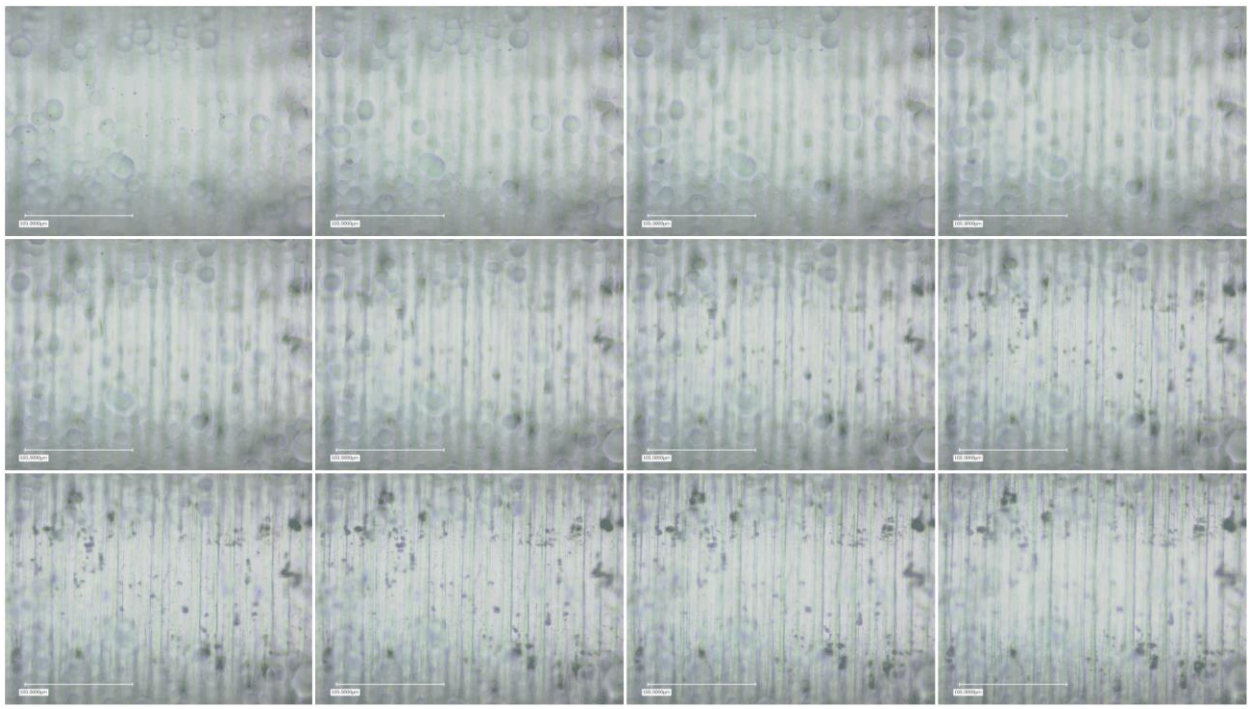

Figure 5-14. Zoom through parylene surface. The focus is on the parylene on the top left, and on the metal in the lower right. The scale bar is 100 um, and the barbell axis horizontal.

'Beading' of the Parylene-N polymer is apparent on the top-left panel of Fig. 5-14, when the microscope is focused on the Parylene-N surface. The machining structure is clearly visible in the last panel of Fig. 5-14 as well, together with metallurgical defects (which appear as black). This figure clearly demonstrates the optical transparency of the Parylene-N dielectric, as well as that the 'beads' on the surface do not appreciably affect imaging of the metal underneath. There were three different thickness of Parylene-N applied: specified as 5 μm, 15 μm, and 45 μm. Measured results were 5 μm, 17 μm, and 41 μm. These measurements were acquired by adding fiducial tungsten welding rods (of equivalent diameter as target rods) to the deposition chamber, and measuring their diameter throughout the deposition process with precision calipers. These 'witness' rods were used to prevent caliper jaws from damaging the dielectric surface of rods used in experiments. The measured results, above, denote the average deposition thickness of 4 'witness' barbells in each coating batch.

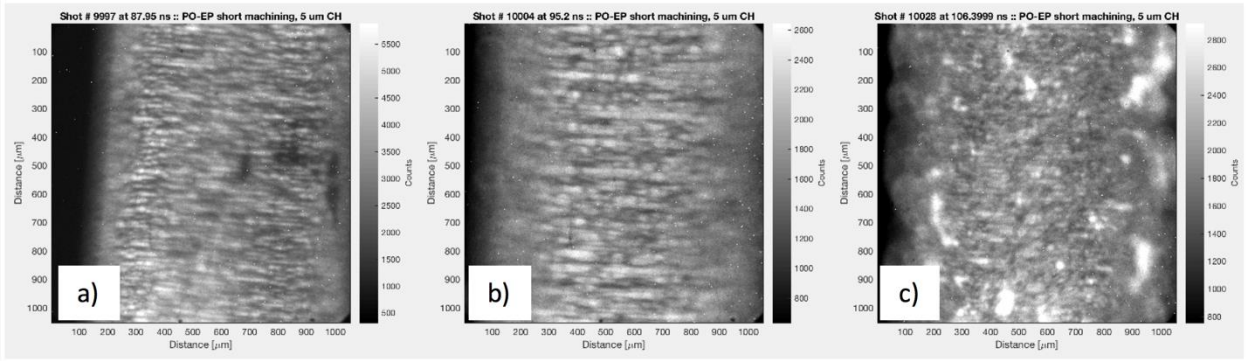

Figure 5-15. Images 2 ns in duration of thermal emissions from rods with 5 μm dielectric coating and short machining structure, at different times and for different barbells. c) demonstrates the bright spots which denote plasma formation. A 5 μm coating provides sufficient tamping to strongly modify the surface evolution. Times are synchronized to current such that 500 kA is at 100 ns, so 90 ns is ~410 kA, as in Fig.5-8.

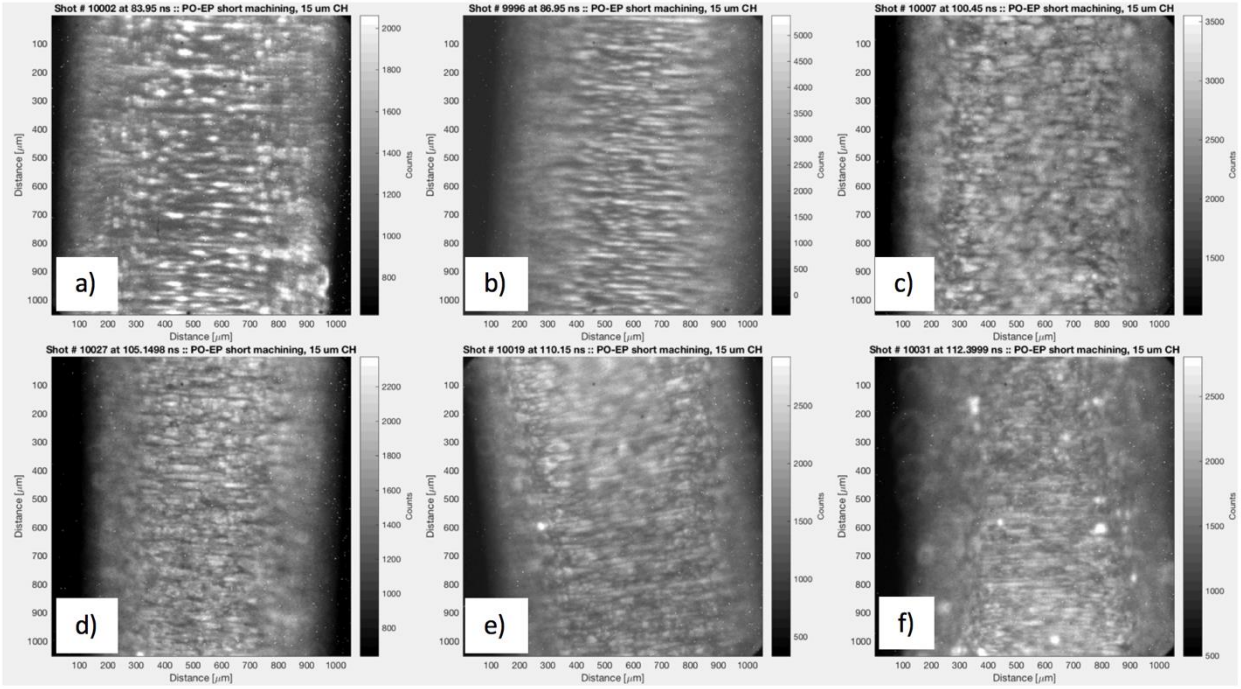

Figure 5-16. Images 2 ns in duration of thermal emissions from rods with 15 μm dielectric coating and short machining structure, at different times and for different barbells. Frame f) demonstrates the spots at which plasma forms. Times are synchronized to current such that 500 kA is at 100 ns, so 90 ns is ~410 kA, as in Fig. 5-8.

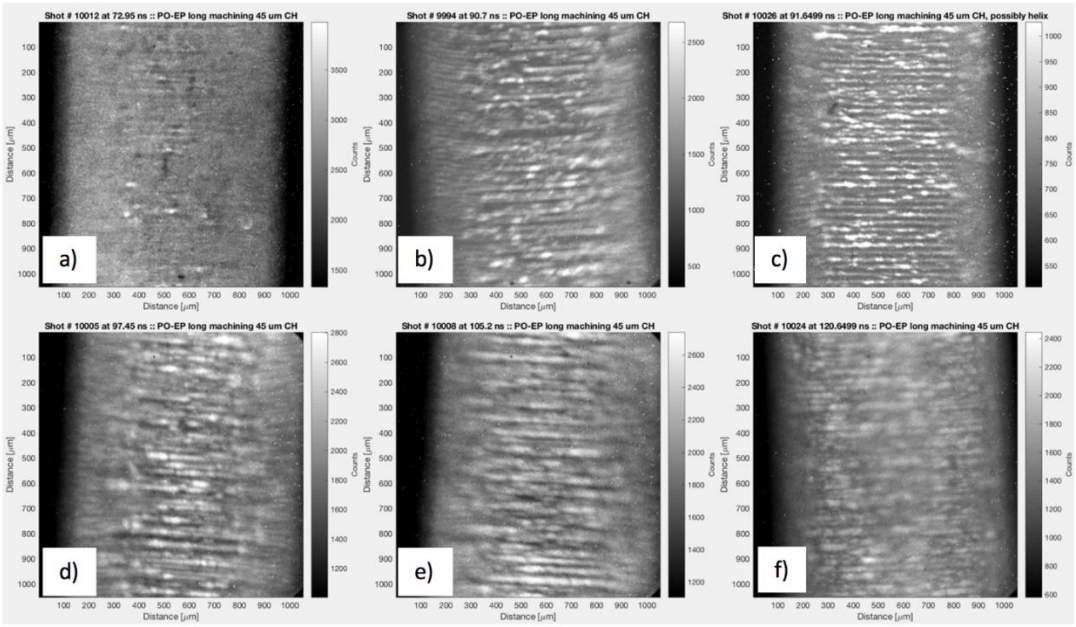

Figure 5-17. Images 2 ns in duration of thermal emissions from rods with 45 μm dielectric coating and long machining structure, at different times and for different barbells. No 45 – μm-coated rods formed plasma. The wavelength of the thermal emissions in c) is consistent with the surface machining structure. Times are synchronized to current such that 500 kA is at 100 ns, so 90 ns is ~410 kA, as in Fig. 5-8.

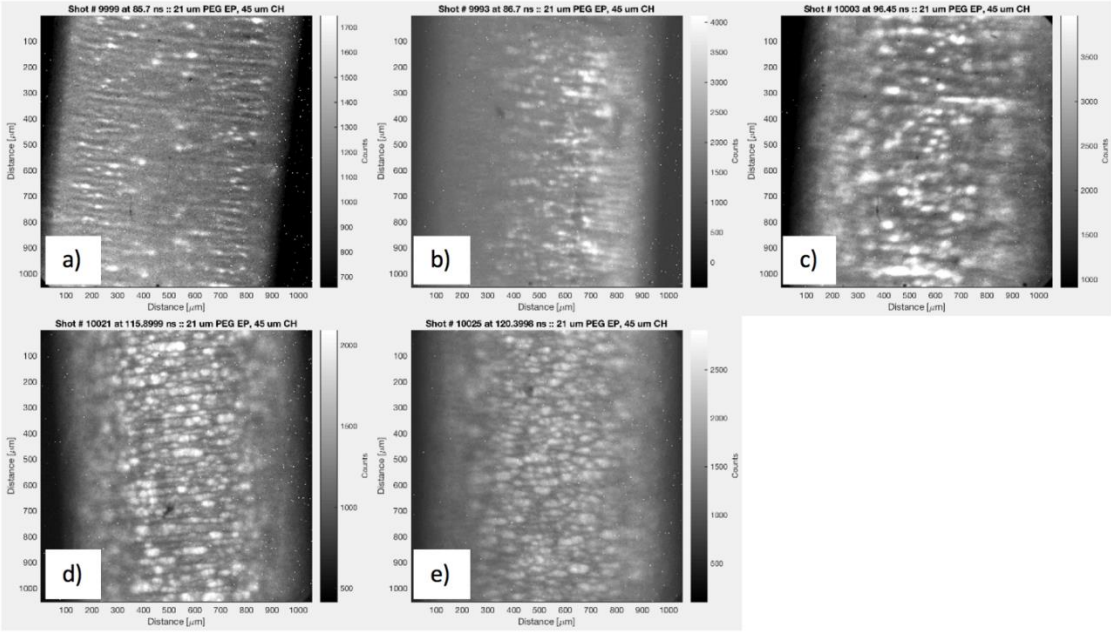

Figure 5-18. Images of thermal emissions from rods with 21 μm removed from the radius by electrochemical etching, and 45 μm dielectric coating. In confocal microscope images of these barbells, very little residual machining structure is present. However, SEM images do show some residual machining structure, which may explain the periodicity in a) and d). Times are synchronized to current such that 500 kA is at 100 ns, so 90 ns is ~410 kA, as in Fig. 5-8.

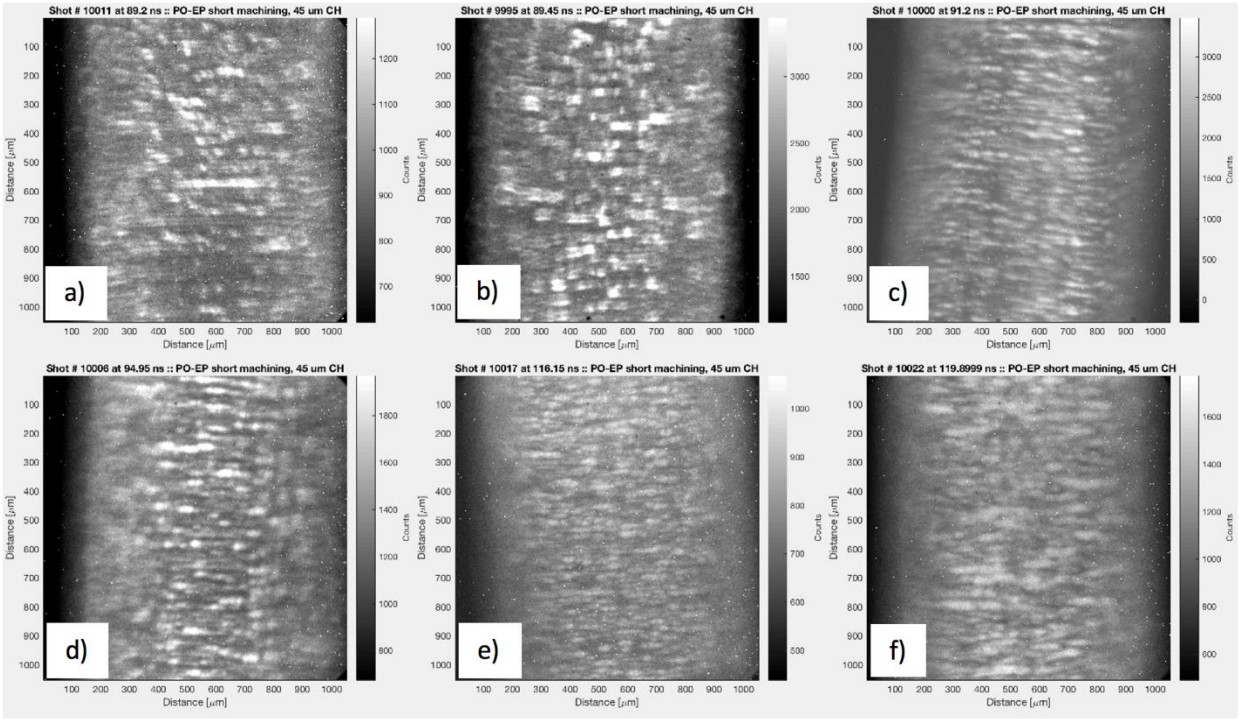

Figure 5-19. Images of thermal emissions from rods with short machining structure and 45 μm dielectric coating. Times are synchronized to current such that 500 kA is at 100 ns, so 90 ns is ~410 kA, as in Fig. 5-8.

ICCD images show variations in thermal emission structure that correlate with surface topography. The preliminary matching of Fourier amplitudes from characterization data and thermal emission data indicate that the ETI does couple to the surface topography. Computation of the full ETI growth rate and terminal amplitude for the different classes of surface finishes above will inform how important each type of surface perturbation is. In addition, variation of the ETI growth rate with coating thickness may inform whether a thinner coating can perform the same instability suppression, allowing lower inertia (and higher velocity) implosions of coated liners. In addition, the results indicate how thin coatings may be before their plasma-suppression function is compromised.

All 12-frame images were taken with a magnification 12, and the same gain setting. Each image denotes a 5-ns time-integrated snapshot of thermal emissions. Frames are back-to-back, so two images denote 10 ns. The earliest frame is the top left (frame a), and the latest the bottom right (frame h). The contrast was changed for some figures to highlight evolution of surface emission features. Images late in time are typically defocused, as the rod expands through the depth of focus of the imaging system. Detailed analysis will follow, but rods in 12-frame images are carrying 400 – 800 kA. Frames are ~ 850 μm wide, consistent with capturing an image of a 800 μm rod with some black background visible (depending on alignment). The first four frames of the 12-frame set are typically dark, and are not shown below to save space.

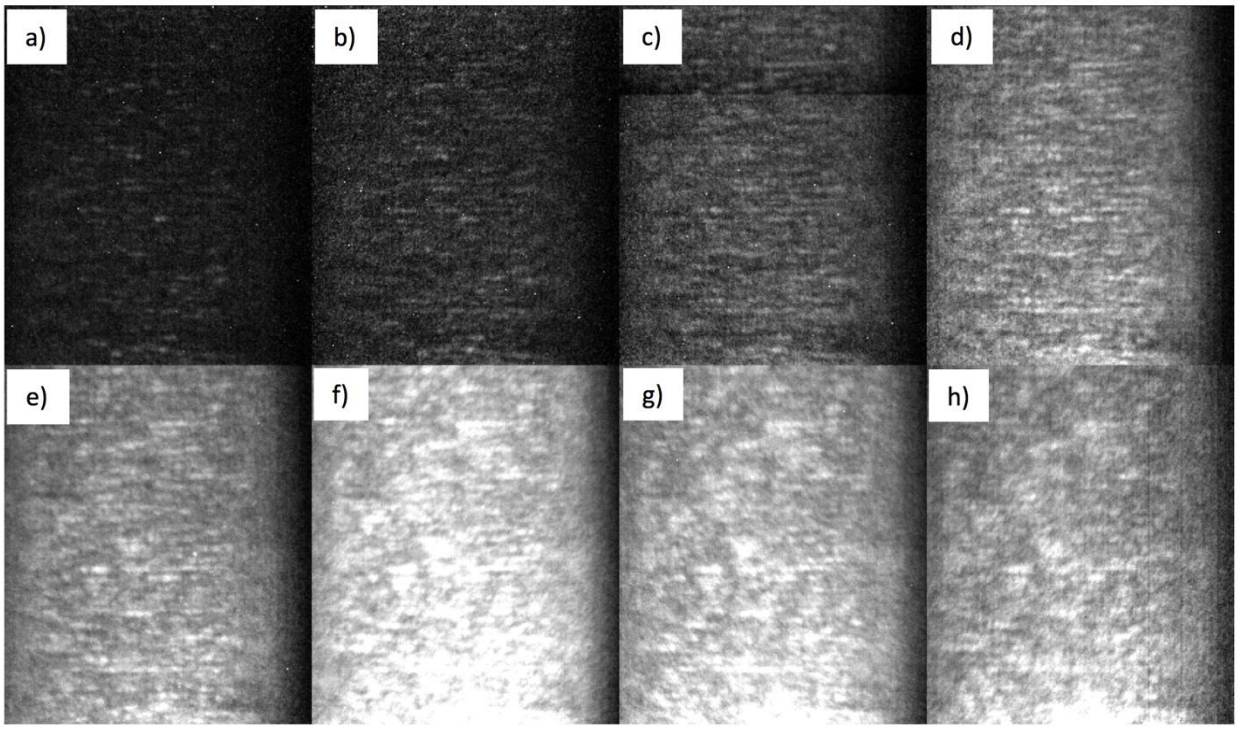

Figure 5-20. A subset of 12-frame images showing thermal emissions for Shot 10000. The rod has short machining structure, and a 45 μm coating. Periodicity in thermal emissions is apparent in all frames, but most pronounced in a)-e).

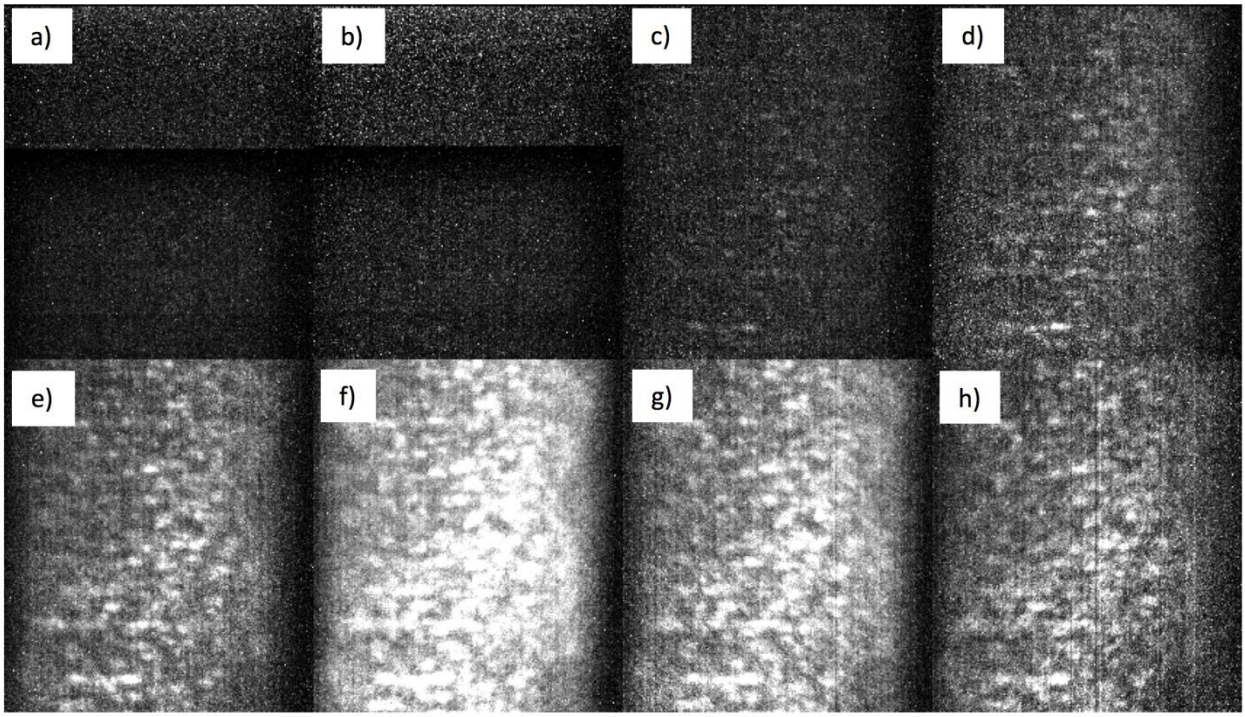

Figure 5-21. Images of thermal emissions from shot 10003, representing a rod with PEG electropolished surface, and a 45 μm coating. Note the comparative lack of periodicity in thermal emissions – likely because the electropolishing procedure removes most (maybe all) machining structure.

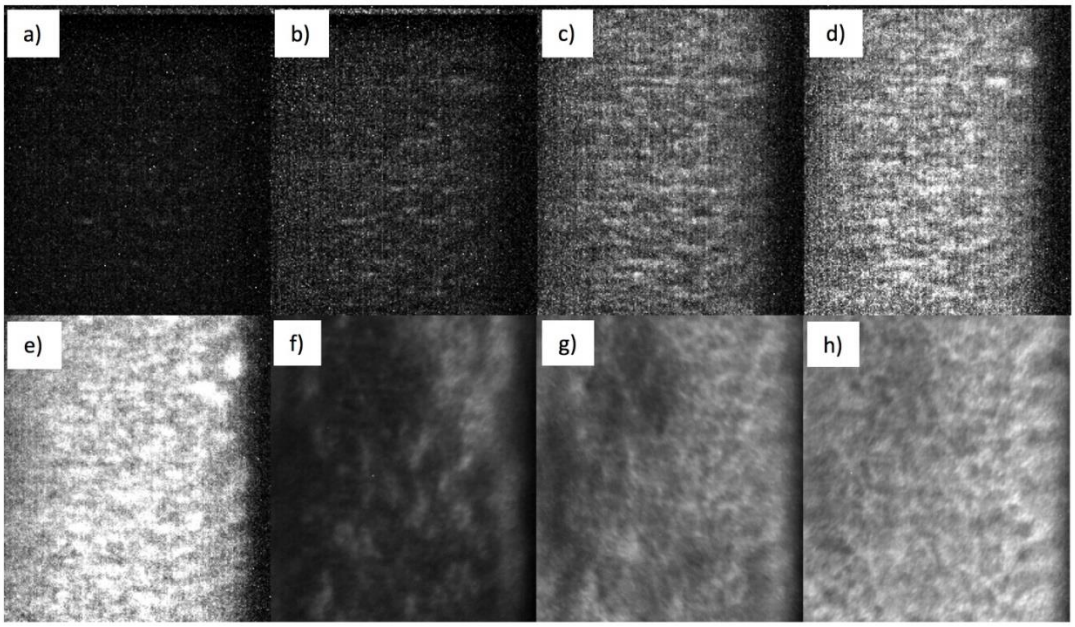

Figure 5-22. Images of thermal emissions from shot 10004, representing a rod with short machining, and a 5 μm coating. Contrast in frames a-e) were adjusted to draw out early time structure. Plasma formation occurs in frame e)-f), and expands in f)-g).

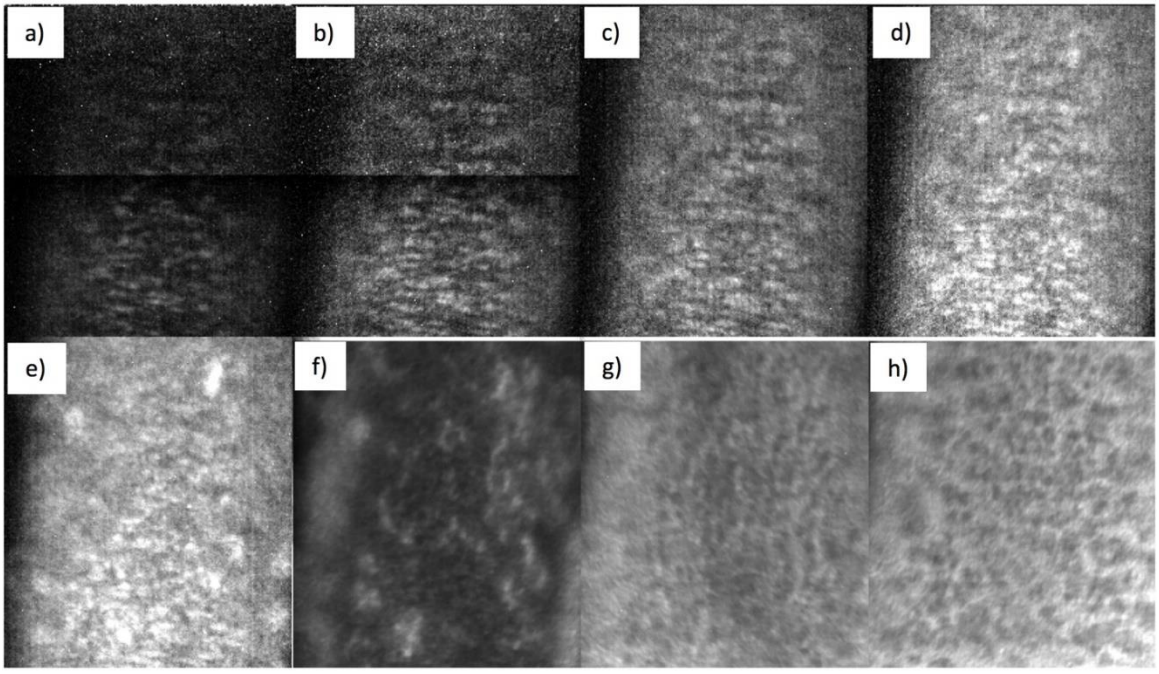

Figure 5-23. Images of thermal emissions from shot 10019, representing a rod with short machining, and a 15 μm coating. Contrast in frames a-e) were adjusted to draw out early time structure. Plasma forms in frame e)-f), and mostly covers the surface by frame g). Note that the qualitative genesis of plasma is distinct from the uncoated case, which forms from smaller regions – this may be because plasma forms on top of the dielectric vs in the metal.

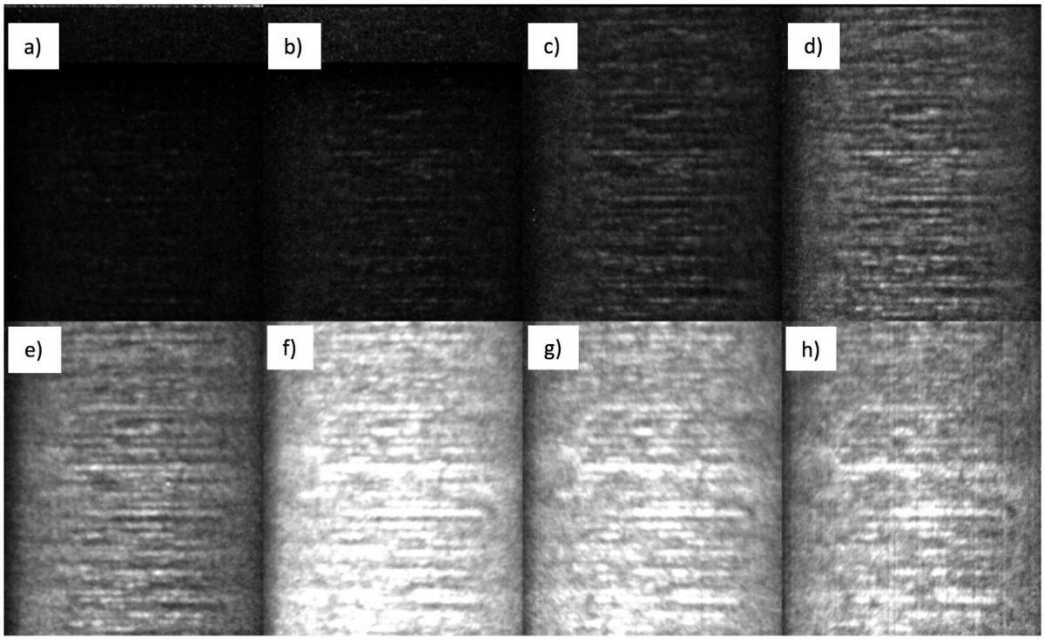

Figure 5-24. Images of thermal emissions from shot 10012, representing a rod with long machining, and a 45 μm coating. This class of rod type displayed thermal perturbations with the most consistent wavelength relative to other rod classes. Again, $45-\mu m$-coated rods did not form plasma.

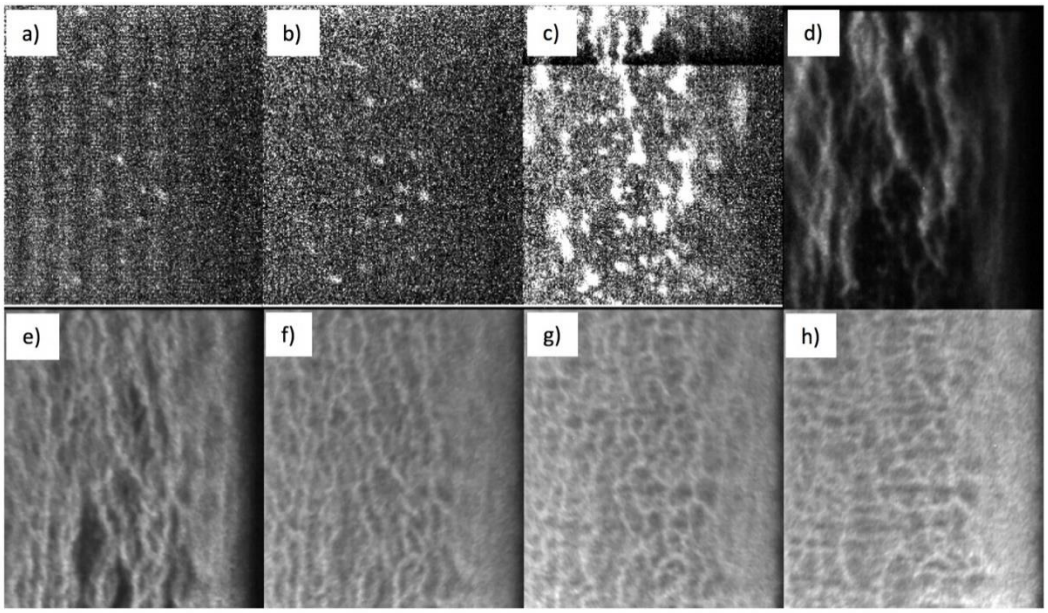

Figure 5-25. Images of thermal emissions from shot 10010, representing a rod with PEG (heavily electropolished) surface and no coating. Plasma forms in frame c)-d), and is filled in by frame f). Contrast in frame a) – c) was modified to show early emissions.

Multi-frame ICCD imaging of rod surfaces demonstrates the dramatic effect that dielectric coatings have on surface evolution. In addition, images show structure in thermal emissions that is correlated with the initial machining topography. It remains to be evaluated whether the

metallurgical defects are a bigger driver of the ETI than the initial surface topography – continued analysis may be able to quantitatively resolve this question.

Preliminary inspection of ETI under different coating thickness is inconclusive. Future analysis is expected to resolve whether the growth rate of thermal perturbations is greater for more-thinly coated rods. This is expected to be the principal focus of analysis efforts going forward.

Campaign 3 -- METI 3:

The intent of this campaign was to investigate how material composition affects the ETI growth. According to theory [xxxiii], T_{crit}/T_{melt} and $d\eta/dT$ control the integral ETI growth. Copper has the same $d\eta/dT$ as Aluminum, but half the ratio T_{crit}/T_{melt}, while Nickel has 70% the $d\eta/dT$ but a third the ratio T_{crit}/T_{melt} as aluminum, which means the three metals could together be used to quantitatively evaluate the ETI growth theory. Pure metals were chosen to diminish the effects of heterogeneous composition and study exclusively how distinct metals manifest ETI differently. Surface finishes have an important effect on ETI and surface evolution. To minimize the effect of surface finish, diamond turning was targeted as the fabrication technique of choice, since it is capable of < 50 nm rms roughnesses (r_a). However, Nickel is on a "no-diamond-turning" list, and comparable surfaces were required. Given this constraint, electropolishing was selected as it was understood (at the time) that electrochemical methods could be used to provide $r_a < 50$ nm. This turned out to be much more difficult than anticipated, and processes led to a diverse set of surface topographies.

Approximately 10 rods of each Copper, Aluminum, and Nickel were first cut from high-purity stock on a lathe to diameter 775 μm, and were then electropolished down to a target diameter 700 μm. Some rods were sacrificed to hone the electropolishing procedure, and only 8 electropolished rods per metal type were coated with dielectric. However, post-electropolishing characterization indicated significant scatter in the diameter of the electropolished rods. For example, for Aluminum, Copper, and Nickel respectively, post-electropolished diameters were measured to be 623 ± 30 μm, 700 ± 16 μm, and 693 ± 15 μm respectively, where the uncertainty corresponds to the standard deviation across the 8 rods of each type. Some Aluminum barbells were only 580 μm, while others were 680 μm – this variability is likely due to the extreme softness of pure aluminum and therefore the difficulty involved in machining rods smaller than $1000\ \mu m$ in diameter. Variability may also be due to the nonlinear nature of the electrochemistry, which changes as Al^{+3} ions are added to the solution after each etch.

The disconnect between well-established electrochemical procedures and the comparatively stochastic results obtained here is potentially due to the large amount of material removed – 75 μm to be specific. The variety of surfaces is also unique to the electrochemical solution, which changes dynamically as each new rod is etched (since each rod deposits metal into the solution when etched).

Al electropolishing: A solution of 4.7% sulfuric acid, 75% sulfuric acid, 6.5% chromic acid, Al^{+3} and Cr^{+3} ions to 6% was heated to $80\ °C$. Barbells were submerged and potentiostatically pulsed at 1.5 V for 200 ms On and 800 ms Off (Off means open circuit, so –1.0 V). Running continuously removed 6 μm/min, so rod diameters were measured, and the run time scaled so their diameters would be consistent. Voltages are measured with respect the steel counter

electrode, so the barbell is the anode and the steel beaker the cathode. Before running each rod, it was soaked in 5 M NaOH at $70\ °C$ for 10-15 seconds to remove the oxide layer.

Cu electropolishing: To a solution of 200 mL H_3PO_4 (Phosphoric Acid, 85% concentration), 0.4 g of soluble starch was added. This was at room temperature with a 200 rpm stir bar. Running continuously yielded a removal rate of $2\ \mu m/min$ -- run times were custom to each barbell to decrease the overall scatter in barbell diameters and produce an average of $700\ \mu m$ barbells.

Ni electropolishing: To a solution of Nickel Sulfate (240 g/L), Ammonium Sulfate (45 g/L), Potassium chloride (35 g/L), O-phosphoric acid (15-70%), and sulfuric acid (15-60%), water was added to reach a total volume of 200 mL. At room temperature and a stir bar rate of 350 rpm, barbells were held at a DC value of 1.2 V for ~ 10 minutes. The rate was $\sim 7\ \mu m/min$, and again times were scaled for each barbell so the diameter-spread decreased.

The results of these electropolishing procedures is shown in confocal microscope images, below.

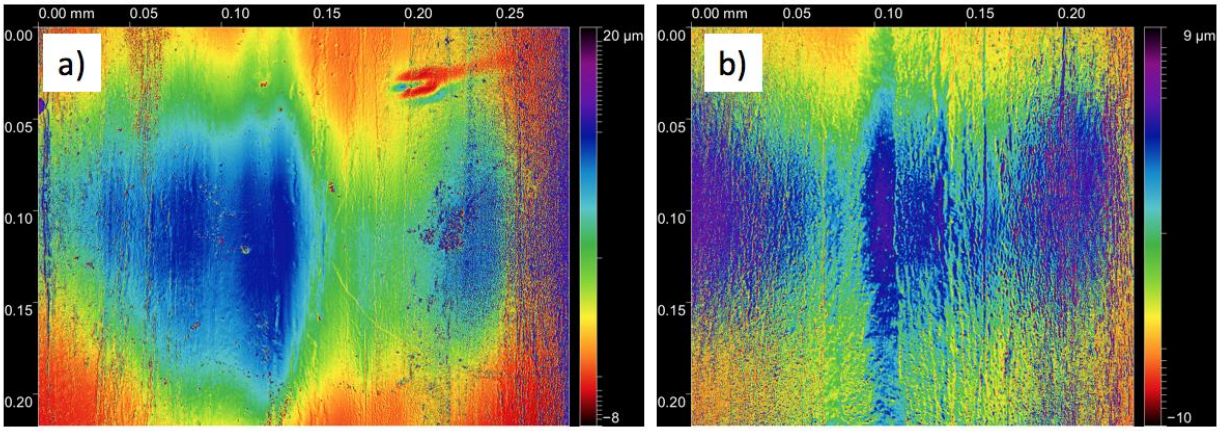

Figure 5-26. Confocal surface maps (curvature corrected) from two $700\ \mu m$ copper barbells, after electropolishing. The barbell axis is vertical.

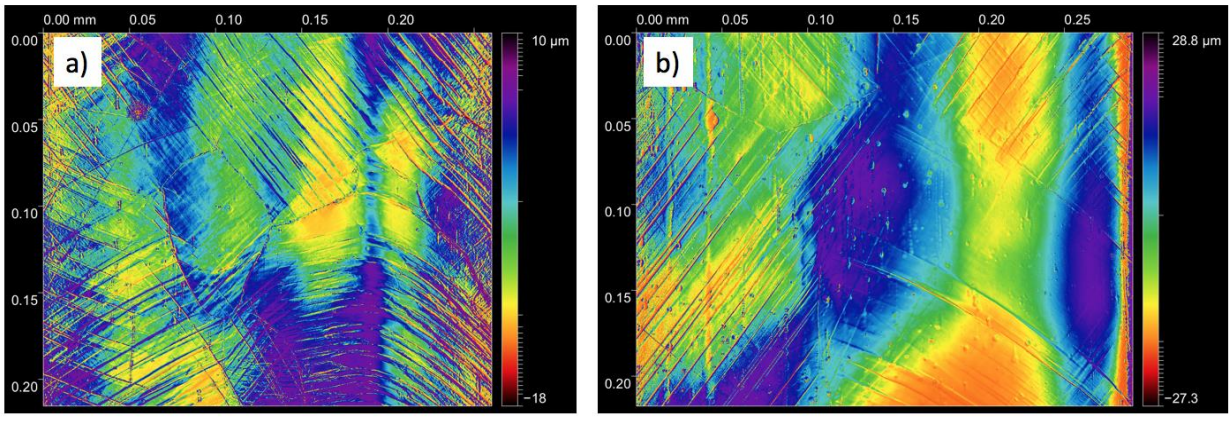

Figure 5-27. Confocal surface maps (curvature corrected) from two $700\ \mu m$ aluminum barbells, after electropolishing. The barbell axis is vertical.

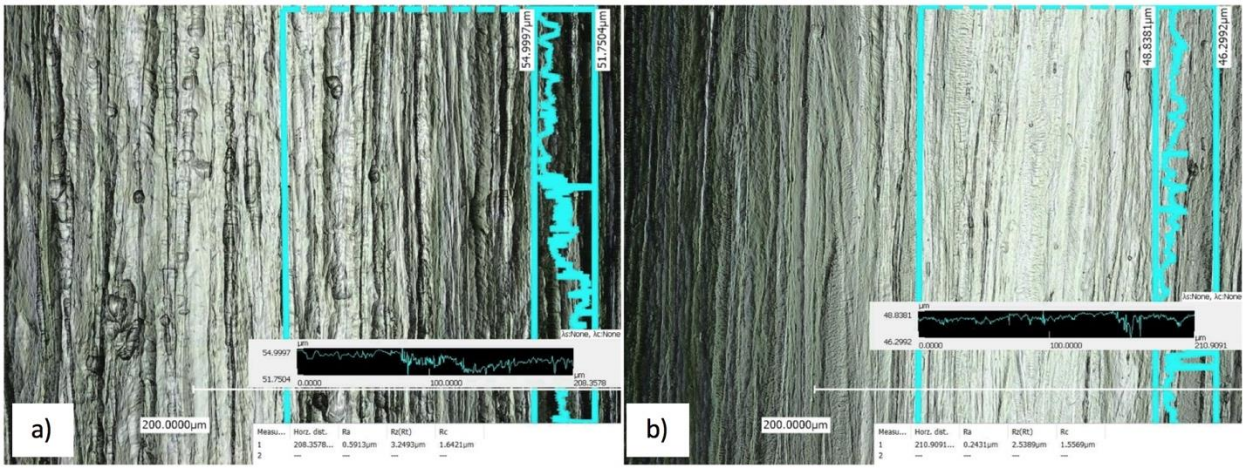

Figure 5-28. Visible light micrographs from two 700 µm Nickel barbells, after electropolishing. Surface height information was captured, but not shown via fake-color maps. A vertical lineout of the surface topography is overlaid on the microscope images, in blue. The barbell axis is vertical, and 'troughs' along the barbell axis are visible in both frames.

After electropolishing, barbells were all coated with (specified as) 45 µm of parylene-N. Characterization images of rods under the microscope (backlit, to silhouette the barbell diameter) were taken before and after the Parylene-N coating. This allowed measurement of the parylene-N coating thicknesses. Manufacturer measured results are pending, but the silhouette method of measuring Parylene-N thickness indicated it was 38 ± 8 µm. An important observation from the target preparation processes above is that generating reproducible metal rods with sub-mm diameter and controlled surface finish (especially with $r_a \sim 50\ nm$) is *exceptionally* difficult. This is in part because each metal has a different softness, machinability, and electrochemistry, and there is no single strategy applicable to all target types.

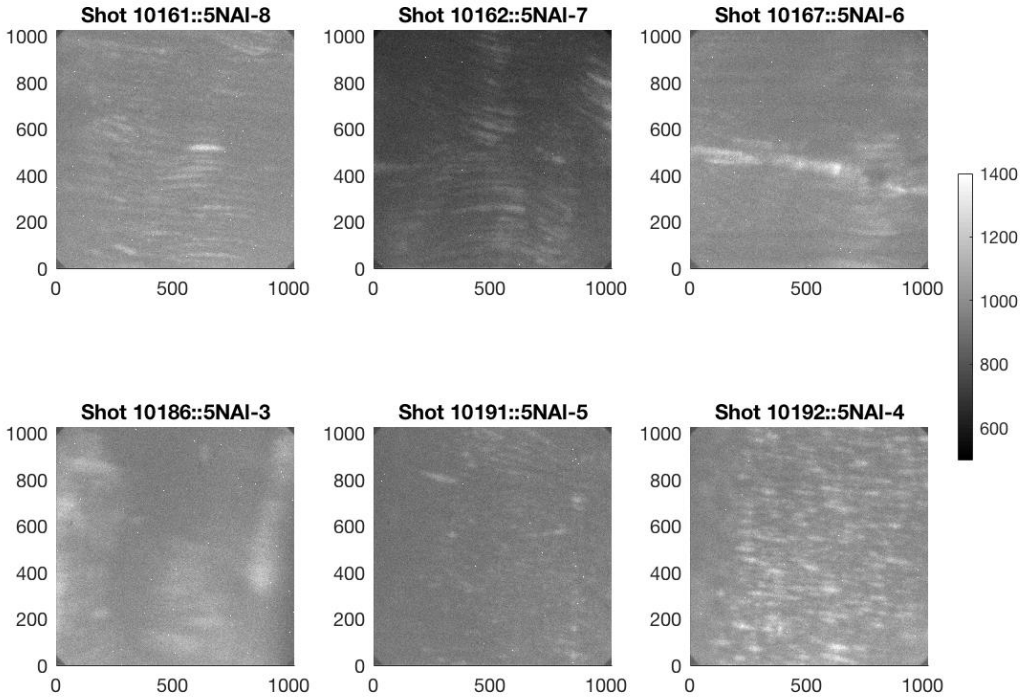

Figure 5-29. ICCD images of thermal emissions from aluminum rod surfaces. The rod is oriented vertical in the image. Timing calculations have not yet been performed, and therefore the current carried by the rod imaged in each frame is not yet clear. Camera gain settings and gate widths are the same for all images, and greyscale denotes counts.

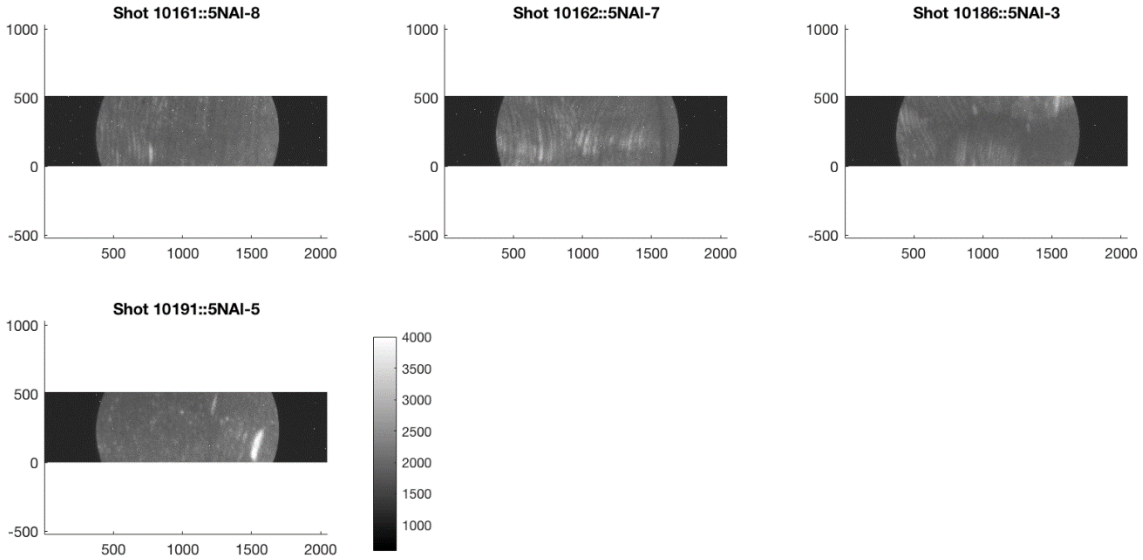

Figure 5-30. ICCD images of thermal emissions from aluminum rod surfaces. The rod is oriented horizontal in the image. Frames captured by this camera are typically 3-5 ns later than those shown in Fig. 5-29. Camera gain settings and gate widths are the same for all images, and greyscale denotes counts.

Tentative inspection of Fig. 5-27 and Fig. 5-29 show that the initial surface topography strongly correlates with the thermal emission structure. While the connection between these is perhaps obvious, it is inconsistent with the original, historical impetus for the ETI (which indicated that surface topography is *uncorrelated* with late time instability amplitudes). It is expected that this relationship be further analyzed and the correlation be made quantitative, if possible.

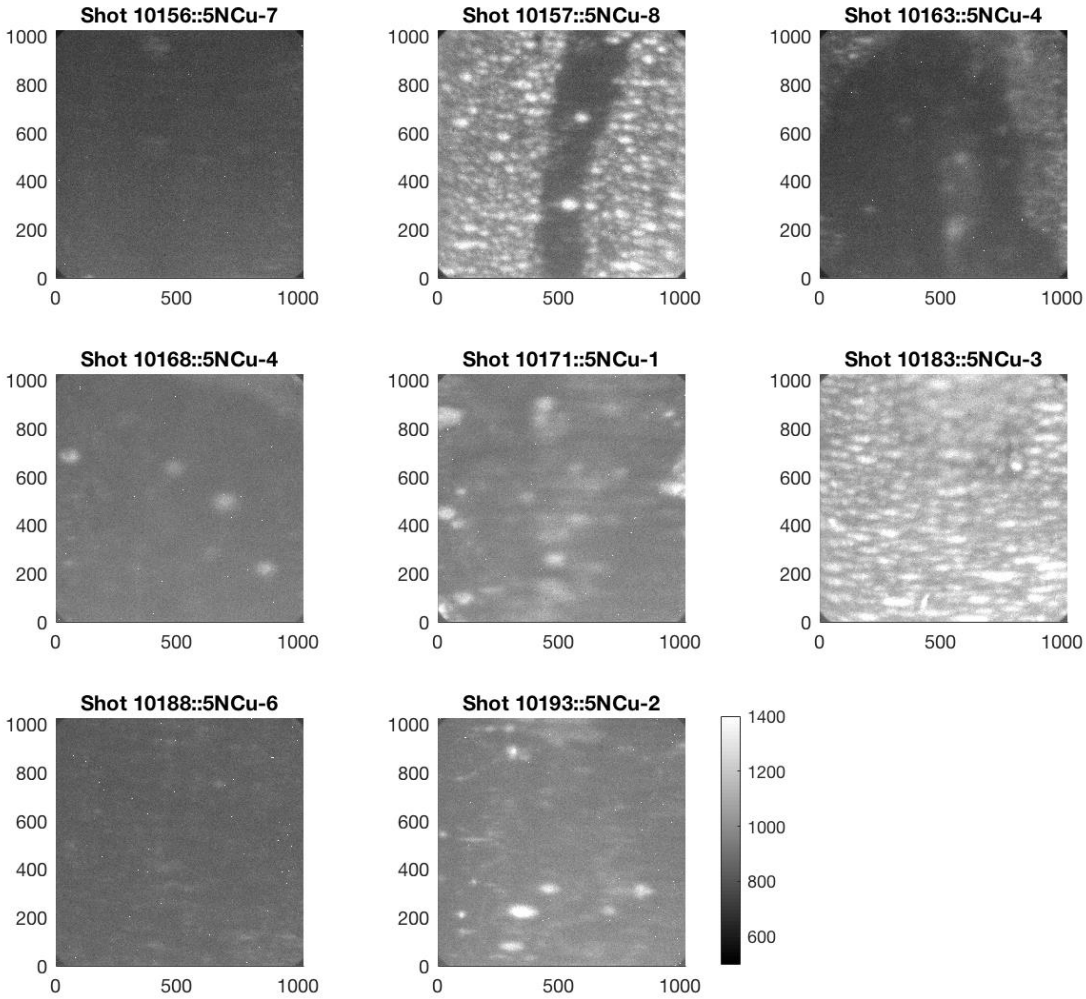

Figure 5-31. ICCD images of thermal emissions from copper rod surfaces. The rod is oriented vertical in the image. Timing calculations have not yet been performed, and therefore the current carried by the rod imaged in each frame is not yet clear. Camera gain settings and gate widths are the same for all images, and greyscale denotes counts. The dark band in shot 10157 does not currently have an explanation. One of two barbells is mislabeled (i.e., either 10163 or 10168 actually denotes 5NCu-5), and a resolution has not yet been determined.

The strata in Fig. 5-31, in the image corresponding to shot 10183, is consistent with strata historically observed in Aluminum 6061 which were, at the time, possibly attributed to metallurgical inclusions. The presence of such well-defined numerous strata on surfaces that are predominantly void of metallurgical inclusion defects suggests two things: One, inclusions may not be the principal perturbation from which ETI grows and two, strata do grow in more diverse

circumstances than aluminum (perhaps obvious, but nevertheless, an important fact to corroborate).

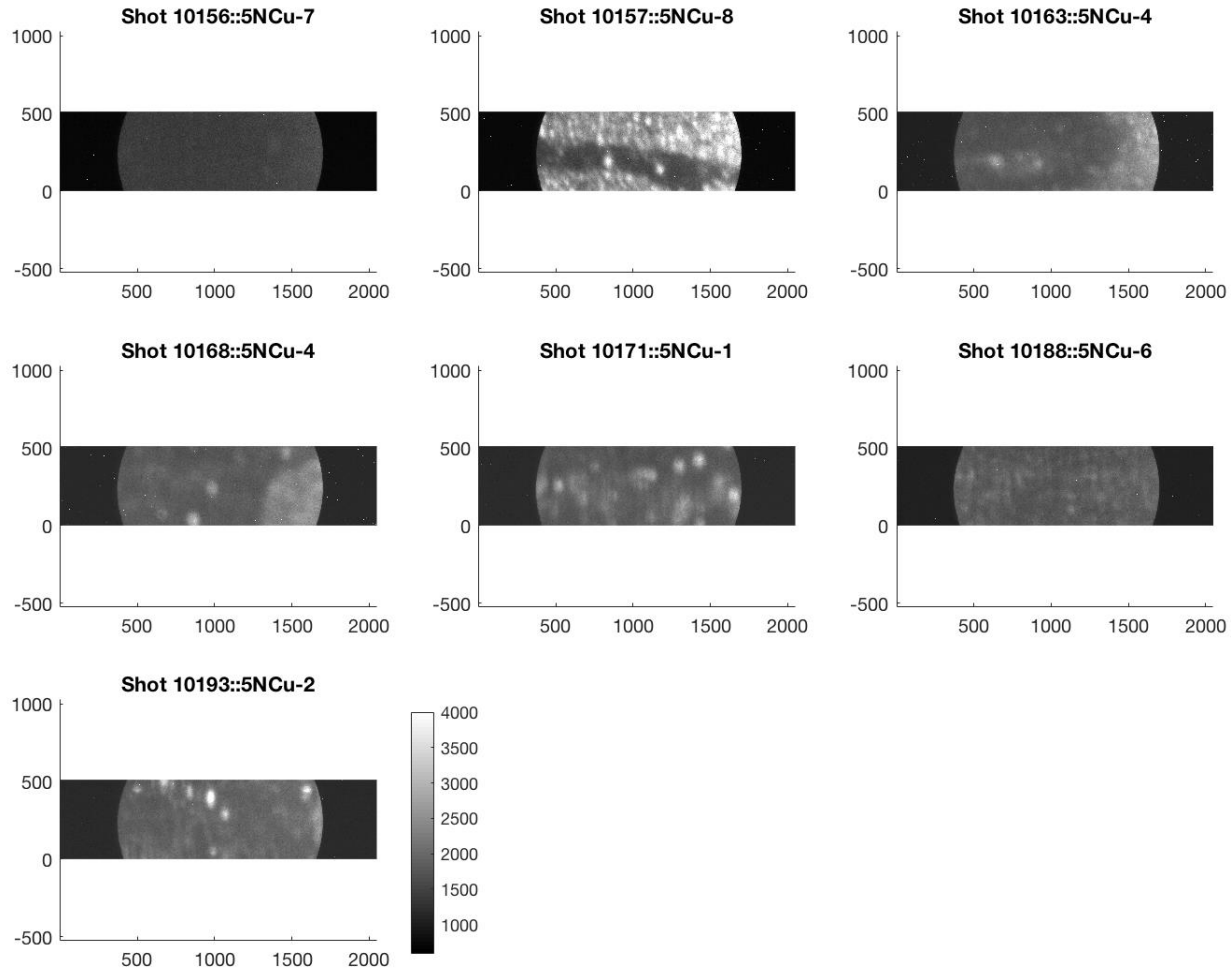

Figure 5-32. ICCD images of thermal emissions from copper rod surfaces. The rod is oriented horizontal in the image. Frames are typically 3-5 ns later than those shown in Fig. 5-31. Camera gain settings and gate widths are the same for all images, and greyscale denotes counts.

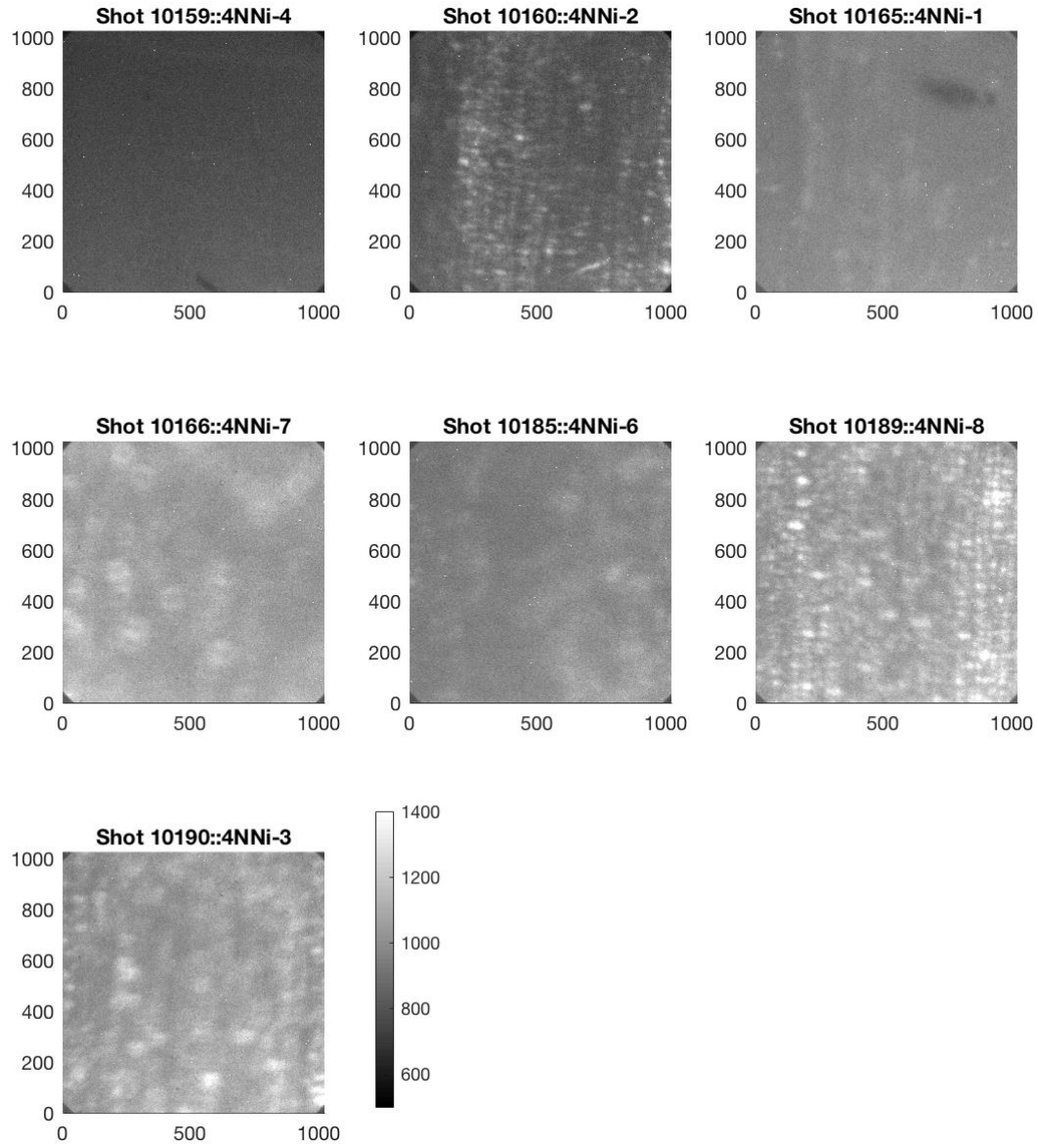

Figure 5-33. ICCD images of thermal emissions from Nickel rod surfaces. The rod is oriented vertical in the image. Timing calculations have not yet been performed, and therefore the current carried by the rod imaged in each frame is not yet clear. Camera gain settings and gate widths are the same for all images, and greyscale denotes counts. Therefore, counts can be compared between different frames.

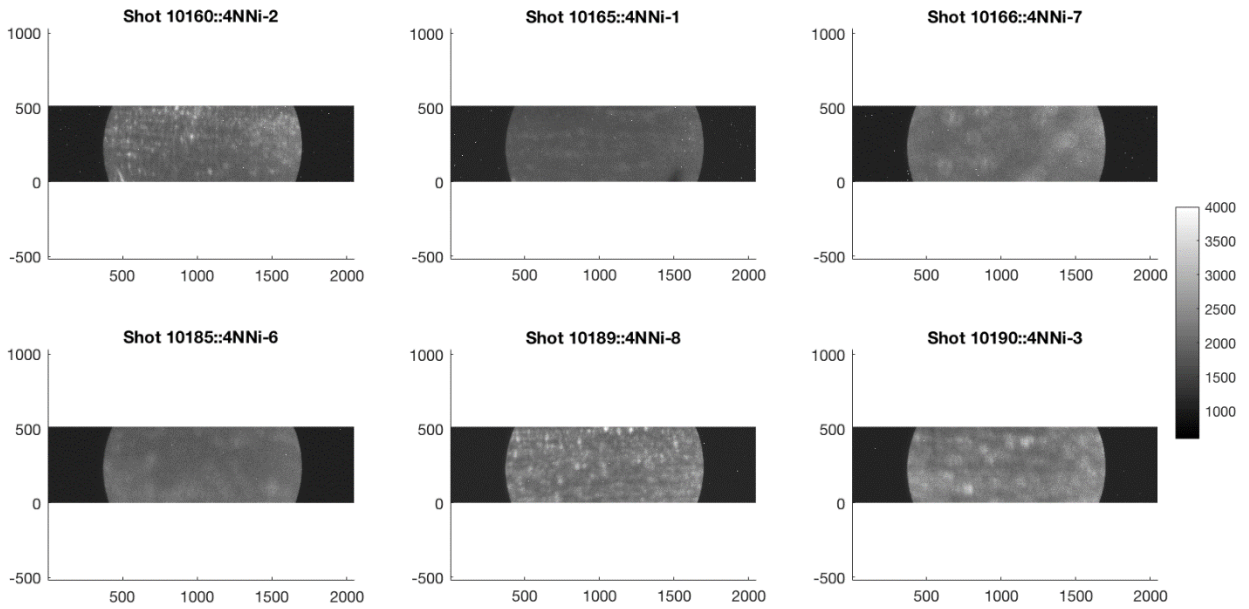

Figure 5-34. ICCD images of thermal emissions from Nickel rod surfaces. The rod is oriented horizontal in the image. Timing calculations have not yet been performed, and therefore the current carried by the rod imaged in each frame is not yet clear. Camera gain settings and gate widths are the same for all images, and greyscale denotes counts. Evidence of defocused imaging is apparent in images from shots 4NNi-7 and 4NNi-4.

Visual inspection of Fig. 5-33 and 5-28 indicate that, like for Aluminum, thermal emission patterns from Nickel rods match those from pre-shot characterization data of the surface topography. Quantifying the correlation between surface topography and surface emission structure is another principal focus of analysis efforts going forward.

6. ENGINEERED DEFECT SIMULATIONS, TARGET FABRICATION, AND EXPERIMENTS

ETI is driven by runaway Joule heating and arises from the dependence of resistivity on temperature [xxxiv, xxxv, xxxvi, xxxvii, xxxviii, xxxix, xl, xli]; early in the current pulse, driving density variations which exceed the liner's initial surface roughness. Simulations of MDIs are generally too coarsely resolved to adequately capture ETI physics, resulting often in dramatic discrepancies between experiment and simulation. Data on ETI is limited and can be difficult to interpret due to the variety of inhomogeneities present in the metal (surface defects, inclusions, grain boundaries, etc.). We've fielded detailed experiments to directly examine ETI growth from high purity (no resistive inclusions) metal z-pinch rods that included carefully characterized "engineered" defects—designed lattices of pits. Such novel targets, with known perturbations in the initial resistivity, can be readily compared with 3D-MHD modeling. Experiments have generated data to constrain 3D-MHD simulations, accelerating the development of an advanced computational model of MDI instability growth.

To execute this research plan, advancements were required in modeling capability, target fabrication and characterization, and experimental execution. In this section, we first detail those theoretical and computation efforts which informed the design of experimental targets. A high-level overview of this work is provided (a draft manuscript which is intended for submission to Physical Review Letters is included in Appendix B). Following this discussion target/defect pattern design choices are discussed. Next, we overview the fabrication techniques developed through this project to generate targets with micron-scale defects of the required depth, diameter, and patterns. Next, we provide pre-shot characterization data from select loads. Then, we summarize the experimental result from the first 6 engineered defect experiments on the Mykonos Facility. Finally, we summarize the preliminary results from these efforts, and propose future work.

Simulation Overview:

Understanding how intense electrical current flows through metal is of singular importance to the Sandia National Laboratories pulsed power program, affecting inertial confinement, dynamic material studies, and power flow physics. In applications involving metal acceleration, a key concern is what seeds the magneto Rayleigh Taylor (MRT) instability, which amplifies surface distortions and limits performance. Initially, researchers hypothesized that surface roughness seeded MRT, but experiments involving metal liners with horizontally vs vertically-oriented grooves showed little difference in implosion behavior, thus implying that surface roughness is not the dominant seed, at least for sufficiently smooth liners. An alternative seed is the electrothermal instability (ETI), which assuming vertical current flow, predicts horizontally-oriented overheated striations in metals, followed by vertical overheated filaments in the plasma state. However, ETI theory does not address how, exactly, ETI striations develop, nor how do striations convert into filaments.

A possible seed for ETI is a non-metallic inclusion, occurring in abundance in many metals. In this work, we study how current redistributes around a resistive inclusion, both analytically and computationally, to seed the striation and filament form of ETI. Our theory, based on the analogy between electrical and hydrodynamic flow, shows that inclusions are powerful sources of current amplification, *independent* of size, so that even micron-scale inclusions are important. The theory also predicts the current perturbation due to a sinusoidally-rippled surface, of amplitude A and

wavelength λ (i.e. an idealization of surface roughness), allowing us to estimate values of (A, λ) at which surface roughness dominates inclusions.

Although the theory allows us to understand how current density **j** is perturbed initially, this is only the beginning of the story: **j** and electrical conductivity σ are entangled in a feedback loop i.e. in metal, regions of higher **j** result in higher Joule heating and temperature, and thus lower σ, forcing **j** out of this region. Using 3D MHD simulation, we show how this feedback loop allows micron-scale inclusions to *transform* into overheated striations 10-15X larger. Later, striations explode, forming craters that can seed MRT, as well as vertical plasma filaments.

Simulations results depend heavily on equation of state (EOS) and conductivity tables, as well as hydrodynamic expansion, thus necessitating validation against experiment. Recent data on rod expansion velocity (see T. Hutchinson paper) allowed us to narrow the suitable EOS tables down to one; even commonly-used tables are deficient, either in their treatment of phase transitions or disagreement with expansion velocities.

An even tighter constraint on simulations is comparison of the visible emission patterns predicted by 3D simulations with experiment. However, diagnostics cannot resolve the micron-scale features exhibited in simulation. To remedy this, we investigated pure Al rods (i.e. essentially devoid of inclusions) machined with ~24 micron-diameter pits, which are more easily diagnosable. Recall that our theory shows that the current perturbation due to the pit is independent of its size, so we can investigate the physics of small-scale inclusions with much larger pits. Remarkably, the emission patterns predicted by 3D simulation agree with experiment. This represents the first "controlled" explosion of current-driven metal, in which a specific heating/emission pattern is predicted and observed.

A draft manuscript concerning these simulations is intended for submission to PRL has been included in Appendix B.

Defect pattern Summary:

Included below are sections from the Statement of Work used to formalize the engineered defect target specifications. It should be noted that General Atomics (GA) was a partner in this process. First, GA's Kurt Tomlinson "invented" the technique to generate engineered defects (see target fabrication discussion within this section), after laser drilling and micro-milling processes proved inadequate. Second, GA responded to new/evolving information from the experimental team, responding to new requests regarding the target profile, maximum roughness specification, acceptance of burrs, etc. In the end, the GA team provided targets that met the needs of the experimental team, allowing project objectives to be met.

Engineered defect fabrication statement of work

The Subcontractor shall machine "engineered defects" of a variety of specified patterns into the surface of a 5N-aluminum 800-micron-dimeter rod.
The Subcontractor shall conduct research and development, and provide targets with engineered defects per the following requirements:

•Rods shall be fabricated according to the drawing shown in Figure 6-1, below.

•Rods shall be diamond turned, using 5N-aluminum.

•Subcontractor shall work with Sandia National Laboratories (SNL) to define the final target details. For, example, radii may be added to the final profile to avoid sharp corners, as agreed upon by Subcontractor and SNL.

•Engineered defects shall be machined into the central rod surface, as listed in Table 1.

•A slow tool servo in "C-axis mode" shall be used to machine defects into the diamond turned surface. The Subcontractor shall work with SNL to define the final target details.

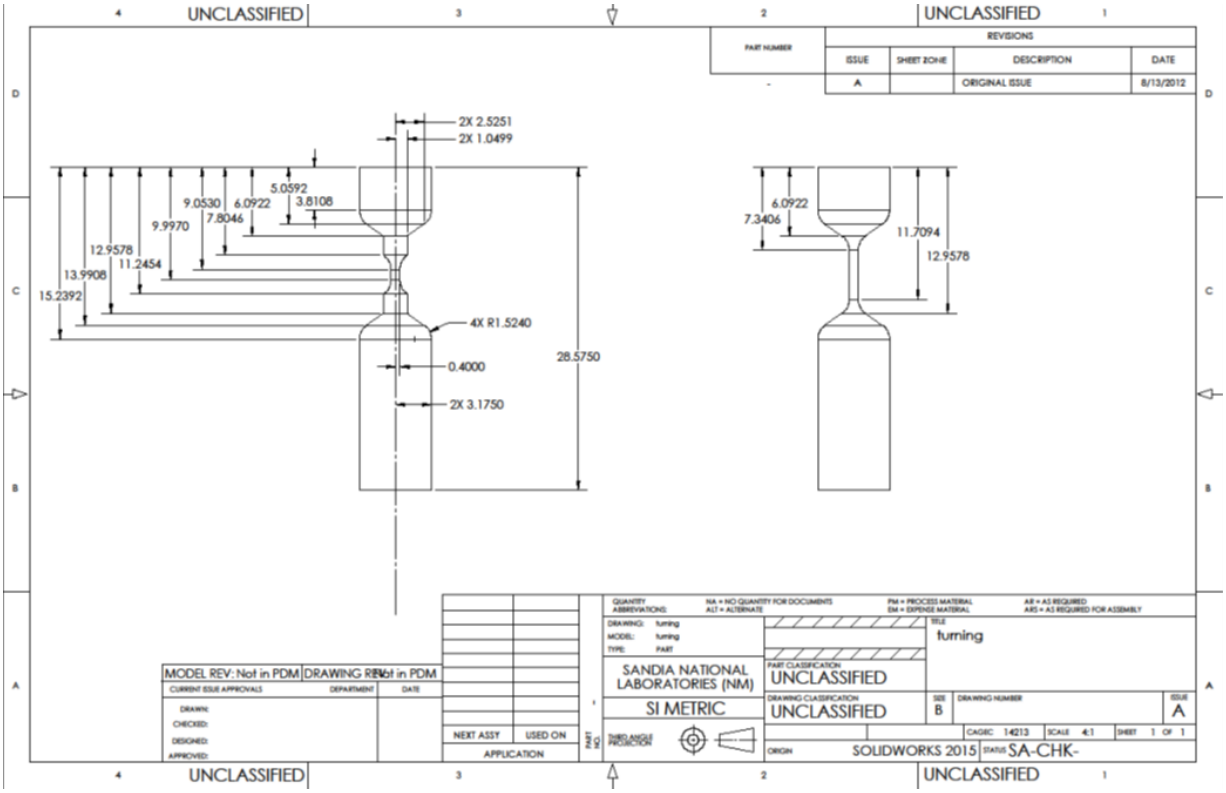

Figure 6-1. Barbell profile drawing

Quantity	Type	Defect Specification
8	Type 1	60 defects on one size, 7.5-micron tool radius, 12-micron diameter pit, 3 microns deep. For further details on defect layout please refer to Figure 2.
8	Type 2	60 defects on one size, 17-micron tool radius, 27-micron diameter pit, 7 microns deep. For further details on defect layout please refer to Figure 3.
6	Type 3	2 defects at 0 degrees, two defects at 180 degrees. For diameter, depth, and defect spacing, please refer to table 2
6	Type 4	2 defects at 0 degrees, two defects at 180 degrees. For diameter, depth, and defect spacing, please refer to table 2
6	Type 5	2 defects at 0 degrees, two defects at 180 degrees. For diameter, depth, and defect spacing, please refer to table 2
6	Type 6	2 defects at 0 degrees, two defects at 180 degrees. For diameter, depth, and defect spacing, please refer to table 2
6	Type 7	2 defects at 0 degrees, two defects at 180 degrees. For diameter, depth, and defect spacing, please refer to table 2
6	Type 8	2 defects at 0 degrees, two defects at 180 degrees. For diameter, depth, and defect spacing, please refer to table 2
6	Type 9	2 defects at 0 degrees, two defects at 180 degrees. For diameter, depth, and defect spacing, please refer to table 2

Table 6-1. Target defect specifications

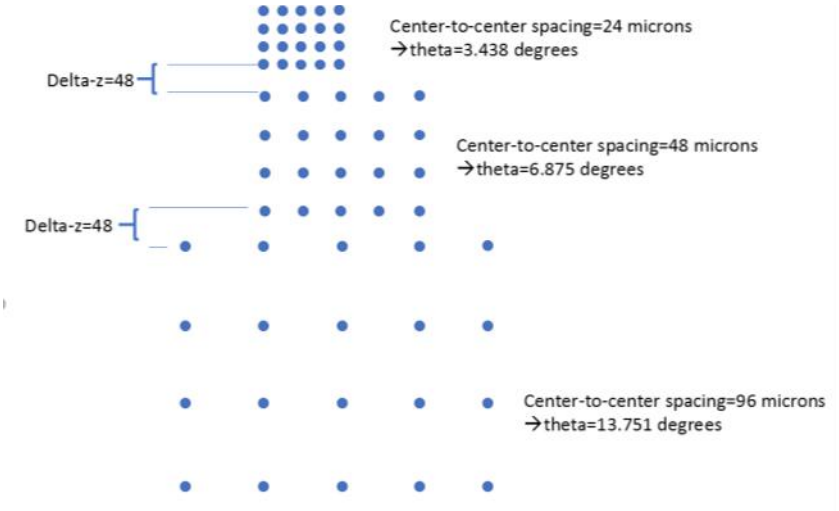

Figure 6-2. Defect pattern 1

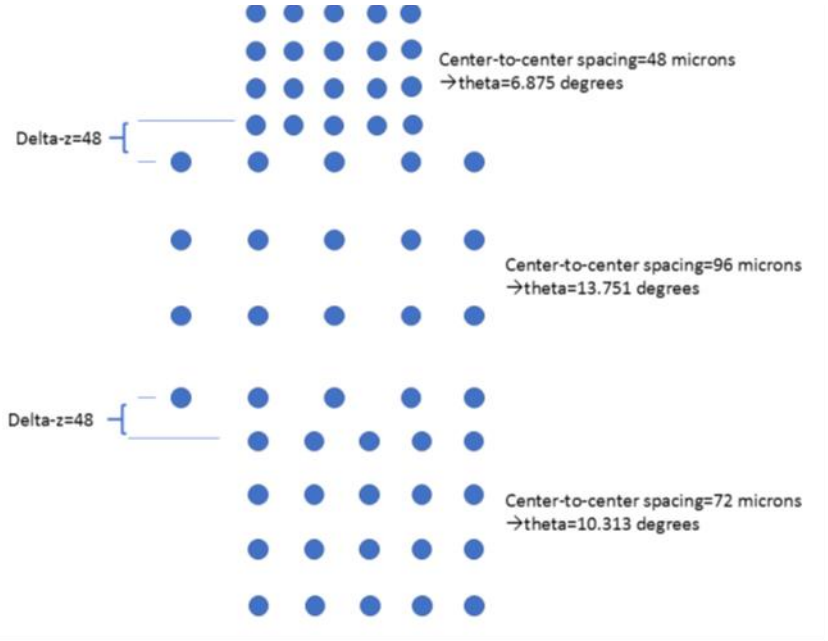

Figure 6-3. Defect pattern 2

		Side at 0 degrees						Side at 180 degrees				
Target type		# of defects	diameter	depth	axial c-to-c	arc length c-to-c		# of defects	diameter	depth	axial c-to-c	arc length c-to-c
3		2	12 µm	3 µm	0	36 µm		2	12 µm	3 µm	0	72 µm
4		2	12 µm	3 µm	36 µm	0		2	12 µm	3 µm	72 µm	0
5		2	24 µm	6 µm	0	72 µm		2	24 µm	6 µm	0	144 µm
6		2	24 µm	6 µm	72 µm	0		2	24 µm	6 µm	144 µm	0
7		2	24 µm	6 µm	72 µm	72 µm		2	24 µm	6 µm	144 µm	144 µm
8		2	48 µm	12 µm	0	144 µm		2	48 µm	12 µm	0	288 µm
9		2	48 µm	12 µm	144 µm	0		2	48 µm	12 µm	288 µm	0

Table 6-2. Target defect specifications

A total of 6 engineered defect experiments were executed in August 2019. At the time of those experiments, only 20 of the requested targets had been fabricated. A preliminary review of the experimental data suggested that the background surface roughness near the defects was often too large. Based on this observation, the experimental team requested that future loads be machined to a final diameter of 1.0 mm, rather than 800 microns, to increase the stiffness off the target during

machining. This change was implemented and found to be extremely effective. Second, the experimental team observed strong overheating generated from burrs along the edges of the machined defect. This was compromising the date, and the GA team responded by modifying the machining process in the following way. First, the barbell profile was cut. Second, the defects were cut (with burrs generated along select edges). Third, an additional 200 nm of material was removed from the entire central rod surface, removing all burrs. This process was also determined to be extremely effective, and all subsequent loads were machined via this process. To date, no burr-free targets have been studied in experiments.

Fabrication Process:

The loads are produced as follows: The overall "barbell" profile of the load is first turned using a single-crystal diamond tool mounted in a 5-axis Precitech diamond lathe. This is a conventional turning operation with the machine in "lathe" mode, meaning the spindle rotational frequency (RPM) is controlled, but not its angular position, and only 2 of the available axes (X and Z) are required (see Figure 6-4). Next, without removing the part from the lathe, the defects are immediately cut using a second single-crystal diamond tool with the lathe operating in the "slow-tool-servo" (STS) mode. In STS mode, as opposed to lathe mode, the spindle's angular position is controlled (C-axis) and precisely synchronized with the motion of any other machine axes. Also, rotational frequency of the spindle must be much slower than with conventional turning (~10 RPM vs. ~1000 RPM) to enable accurate, simultaneous control of multiple axes given the kinematic limitations of the machine. By not removing/replacing, or otherwise disturbing the load between the turning and STS (defect) machining operations, the depth of the defects can be most accurately controlled because the perfect alignment of the load with the machine axes that was established during the turning operation is not altered. Further improvement of defect depth control is achieved by performing the STS operation within minutes of the turning, minimizing machine temperature variations between the two steps which would invalidate relative calibrations of the two tools used. Time to fully machine one load is approximately 4 hours.

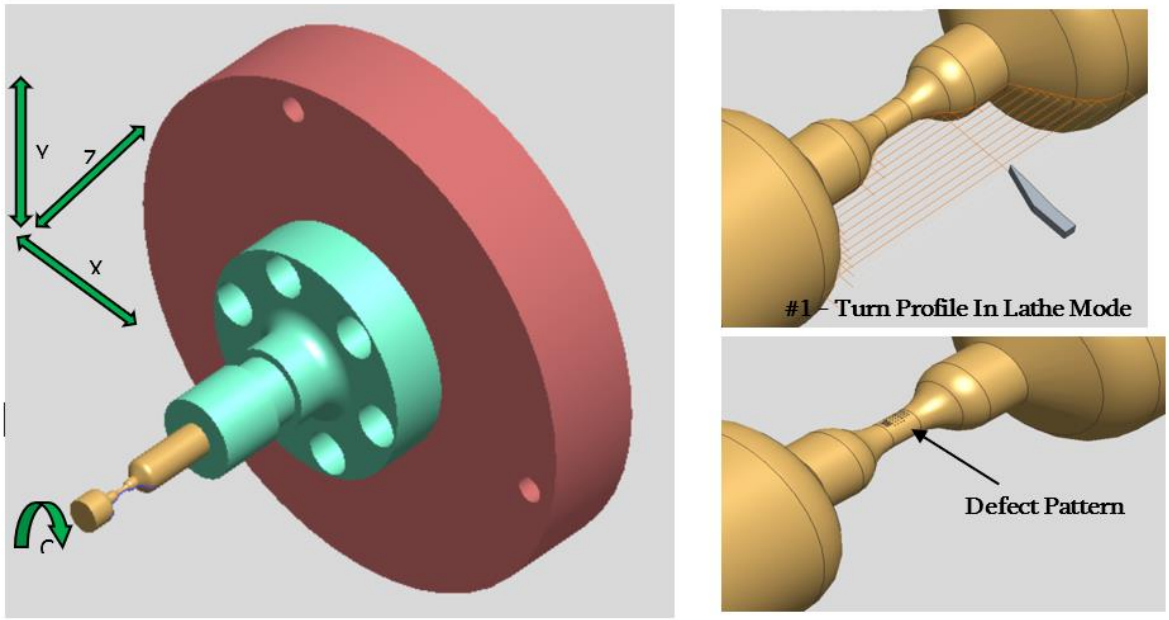

Figure 6-4. Machining setup

The defect cutting uses a scooping motion of a specially shaped, single-crystal diamond tool as illustrated in Figure 6.5. The 2-D radius of the diamond's tip is the same as the spherical radius of the defect. Figure 2 shows only the final pass of the tool (i.e., at full depth), but the operation is actually comprised of numerous passes, each of only half-micron depth, repeated in succession until the final depth is reached. Depth varies for each of the three defect sizes used in the experiments (i.e., spherical radius = 0.0075um, 0.015um, and 0.030um), but all have depth equaling $1/4^{th}$ of the 2-D defect diameter at the load surface. By adhering to the 4:1 rule, and rotating the cutting tool around where a line connecting the load axis with the spherical center of the defect intersects the theoretical far side of the defect sphere, the minimum required relief angle to avoid the heel of the diamond from rubbing the defect is a constant 26.6 degrees throughout the cut. This minimum required relief angle enables the use of a diamond tool with 30 degrees relief, which happens to be about the maximum relief achievable on a single-crystal diamond tool to prevent fracturing during its manufacture.

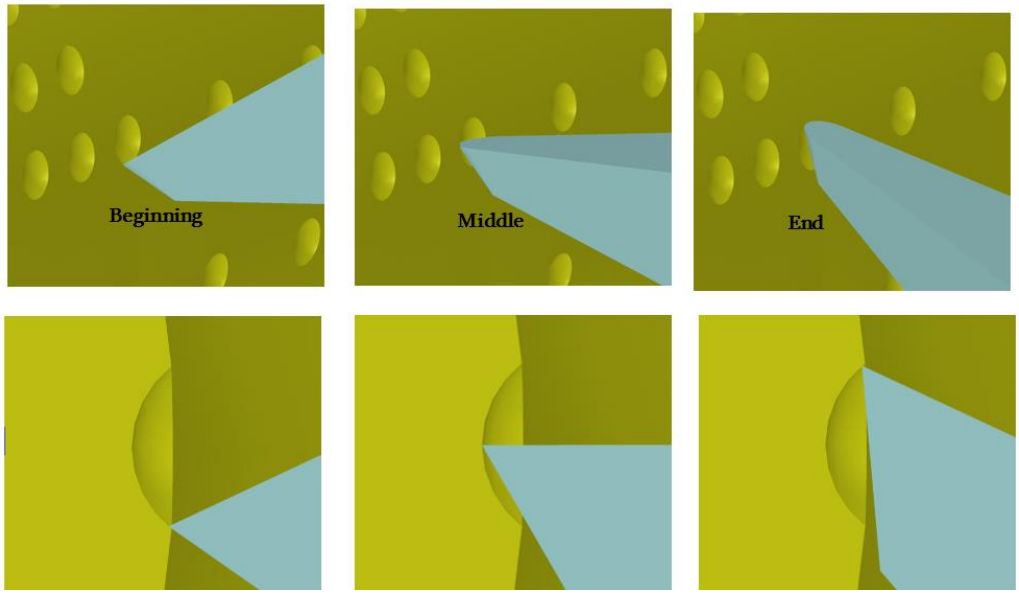

Figure 6-5. Tool path when "scooping" a defect

Target Characterization:

A total of six engineered defect experiments have been executed on the Mykonos Facility. The primary purpose of these initial experiments was to gain a preliminary understanding of the evolution of these targets, and compare the experimental data to pre-shot characterization data to determine whether target design changes and/or changes in fabrication technique were required. In this section we show confocal microscopy data for each of the 6 targets used in experiments. In the following section, we show preliminary results from those experiments, and discuss changes that were made to the target design due to learning from the initial 6 experiments.

Targets were characterized by the GA (General Atomics) target fabrication team to confirm appropriate defect spacing, requested rod diameter, as well as to determine surface roughness of the barbell near the defect. The defect locations and rod diameter met the desired specification. In Table 6-3, the characterization information provided by the GA team shows a large spread in the measured "adjacent surface roughness." As will be clear in the following experimental results discussion, the background surface roughness is a critical experimental parameter, and must measure in the 10s of nm to enable study of engineered defect evolution. In response to this experimental observation, surface roughness was improved by first executing more frequent diamond tool inspection to ensure worn tools were not used, and second, by increasing the central target diameter from 800 microns to 1000 microns to reduce rod vibration during turning.

Shot Number	Load Type	Barbell #	OD (mm)	Divot Depth (mm)	Divot Width (mm)	Side 1 Divot Spacing (mm)	Side 2 Divot Spacing (mm)	Adjacent Surface Ra (nm)
10194	7	2	0.8000	0.0055	0.0235			156
10195	5	2	0.8010	0.0060	0.0235	0.0720	0.1440	245
10196	7	3	0.8010	0.0055	0.0230			17
10197	7	4	0.8006	0.0055	0.0230			41
10198	7	5	0.8020	0.0065	0.0240			10
10199	5	4	0.8025	0.0060	0.0235	0.0720	0.1440	67

Table 6-3. Barbell and defect characterization results

After receiving loads from GA, the physics team gathered further pre-shot characterization data using a confocal microscopy system. Date from all six experimental loads are shown below. Gwyddion software was used to process the .vk4 data files from the microscopy system. For the first dataset, the generic process used to process the data is detailed below.

Step 1: Open raw 50X mag characterization data in Gwyddion, and rotate CCW by 90 degrees. Rotated but otherwise raw data is shown if Fig 6-6. Next to the topographic data are profiles generated along the crosshair overlaying the surface data. The cylindrical curvature of the load is obvious in the profile data, as is the ~6 micron dip associated with the defect. Note that much of the defect surface is not well characterized. This is because the light return to the microscope from very steep surfaces is insufficient for a measurement. New techniques are being developed to better characterize the defect. In general, we anticipate turning the rod in small angular increments to gather high quality date from the normal portion of the defect pointing towards the instrument. Then, we'll develop a means of stitching together the data from multiple scans.

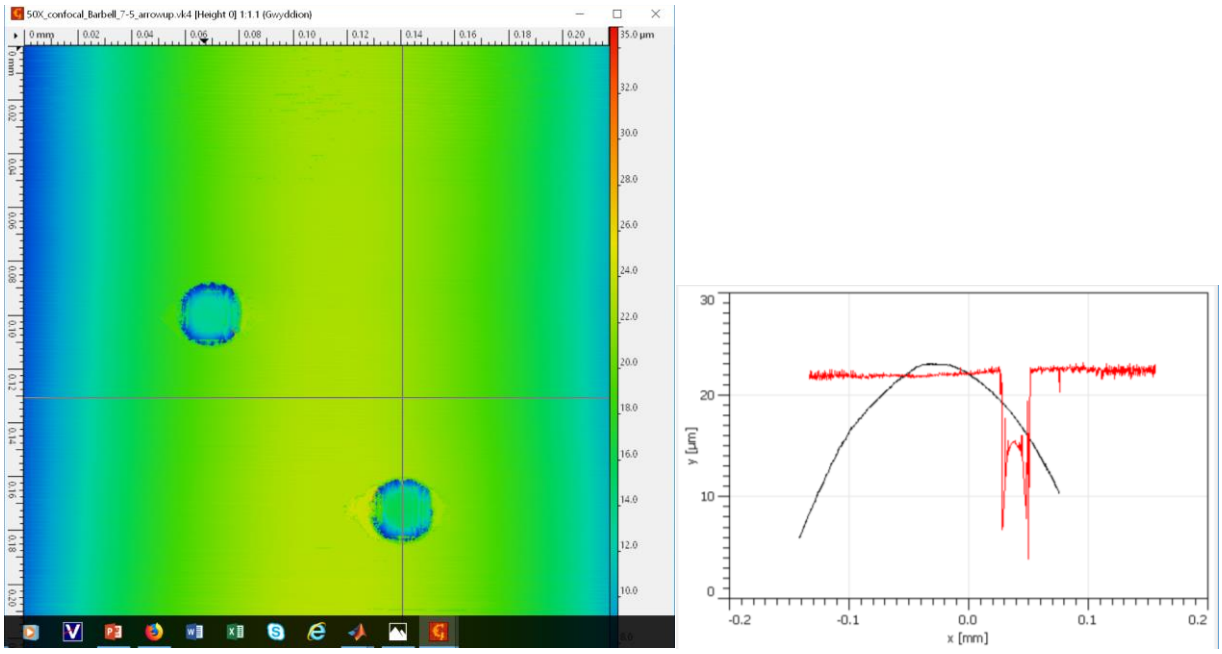

Figure 6-6. Rotated but otherwise raw confocal microscopy data.

Step 2: Remove cylindrical curvature via the steps below.

→Data Process

→Level

→Fit shape

In fit shape menu:

Function type: cylinder (lying)

Output type: difference

Check “full fit is geometric” and “show differences with adapted color map”

Click “Fit” button, and it will output data with cylindrical curvature removed

Data has now been processed to remove the cylindrical curvature.

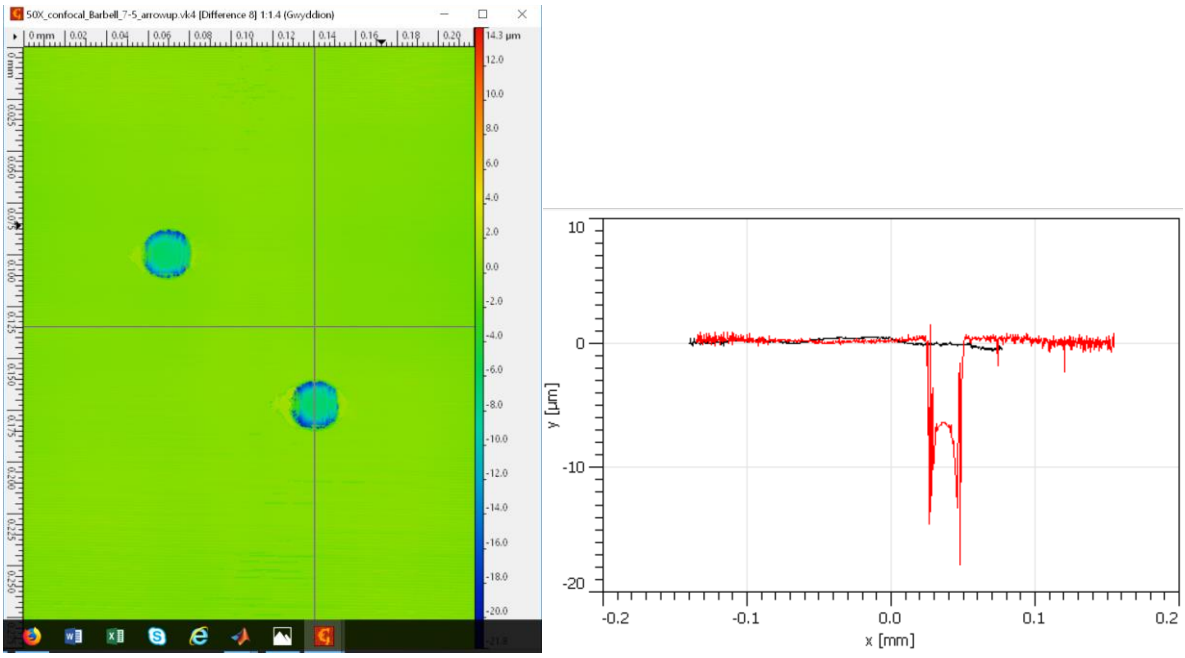

Figure 6-7. Microscopy data after correcting for cylindrical curvature.

Step 3: Modify the vertical (or depth) scale to accentuate features of interest. Two examples are shown below

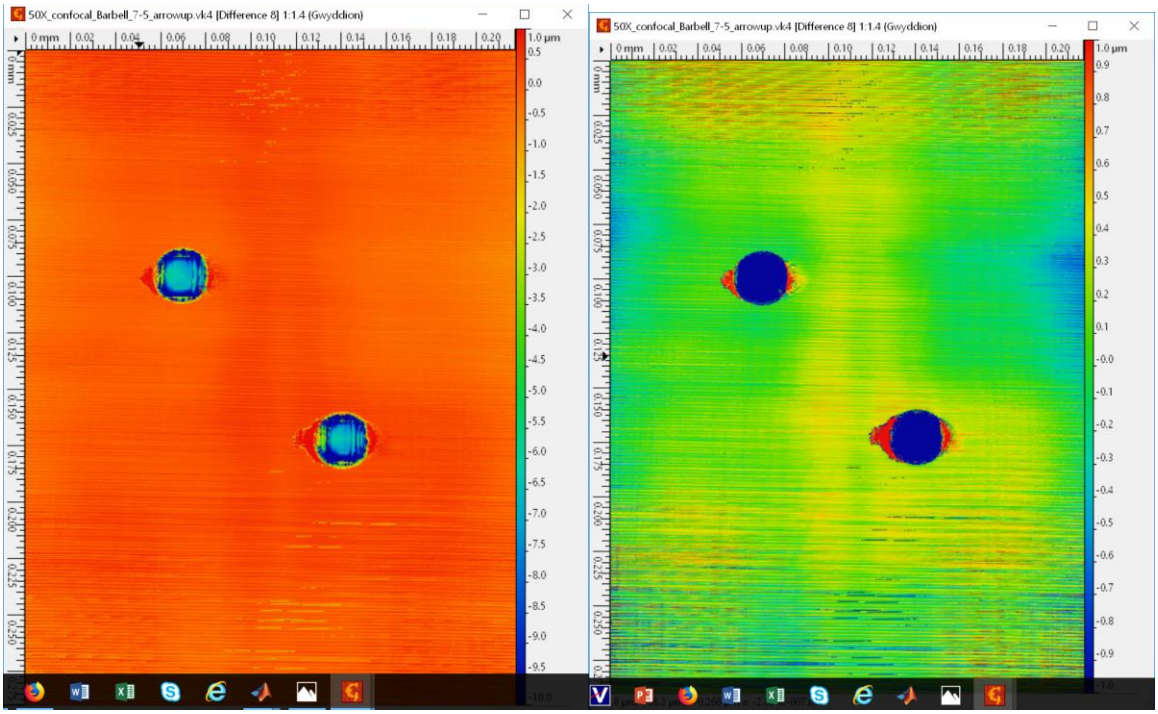

Figure 6-8. The same data set, represented with different vertical colorbar scales to accentuate different features.

In the representations of the characterization data shown below, we follow the general procedure outlined above for each of the 6 experimental loads. We provide data only from one side of the load, namely the side with the smaller defect-to-defect spacing, as this was the side of the load that the high resolution Andor ICCD cameras generally viewed during Mykonos experiments.

Below, confocal microscopy data is shown for each of the 6 experimental loads (named by Mykonos shot number). Data is displayed after correcting for the cylindrical curvature of the rod. The colorbar associated with surface height variation is truncated to accentuate the roughness of the surfaces near the defects. Data from the defect itself is not well captured, and therefore, we've truncated the color bar to not include this information, allowing more dynamic range for the rod surface structure. In all cases, a single vertical line runs down the (near) center of the image. This line is what was used when the Gwiddion software calculated the surface roughness (Ra). The roughness shown here does not match that shown in Table 6-3. This is largely due to the fact the different surfaces were selected. A systematic means of evaluating and reporting surface roughness for each load needs to be determined to ensure comparisons from one target to the next are meaningful.

Mykonos-10194:

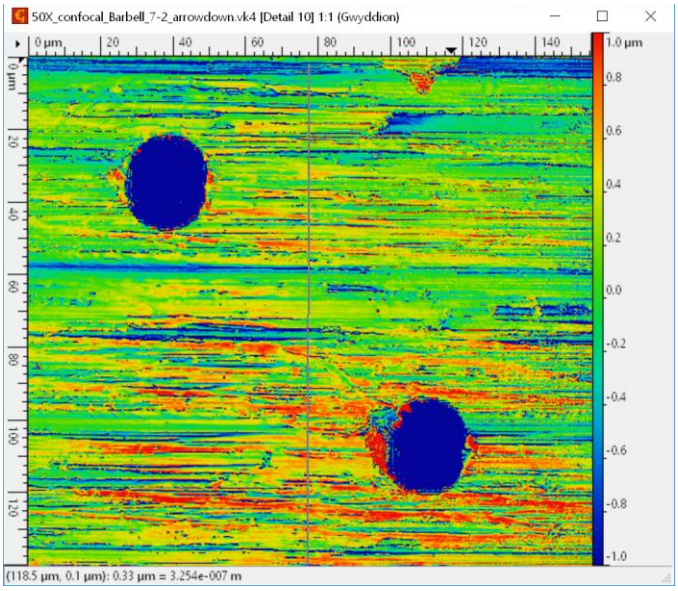

Figure 6-9. **Ra=397 nm**

Mykonos-10195:

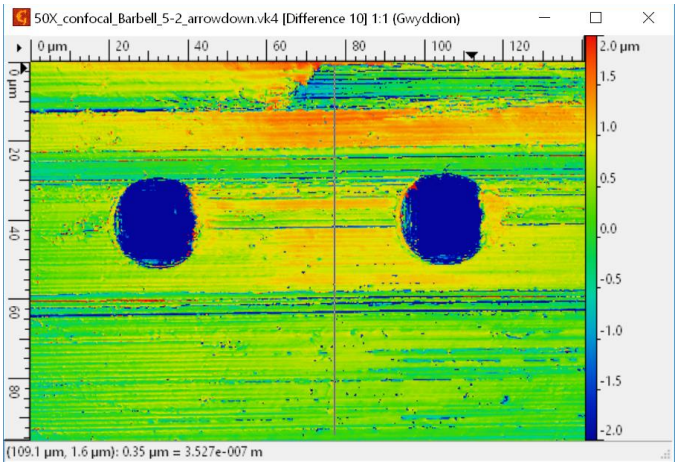

Figure 6-10. **Ra=533 nm**

Mykonos-10196:

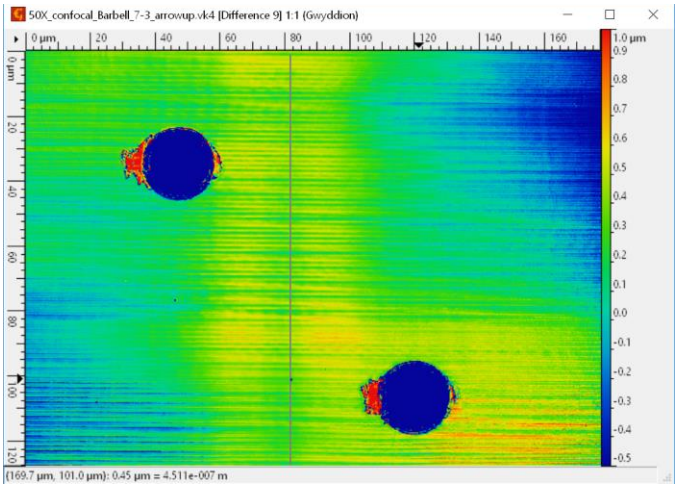

Figure 6-11. **Ra=81 nm**

Mykonos-10197:

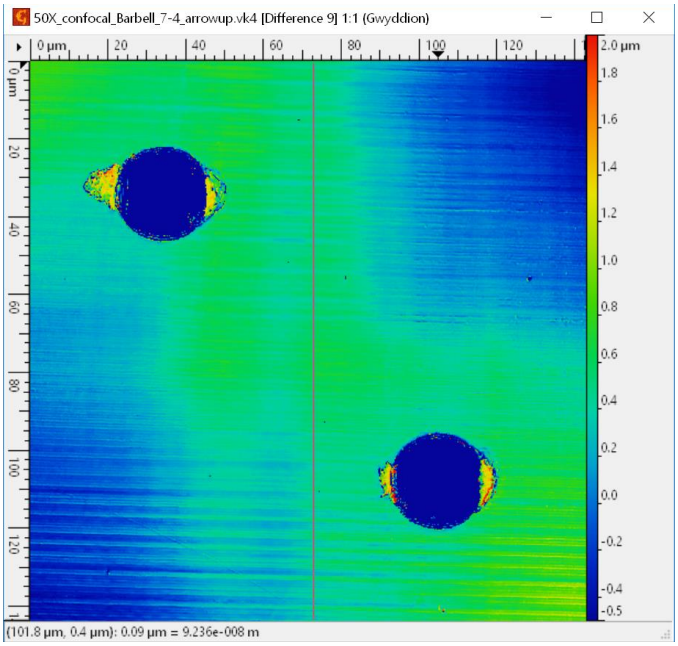

Figure 6-12. **Ra=57 nm**

Mykonos-10198:

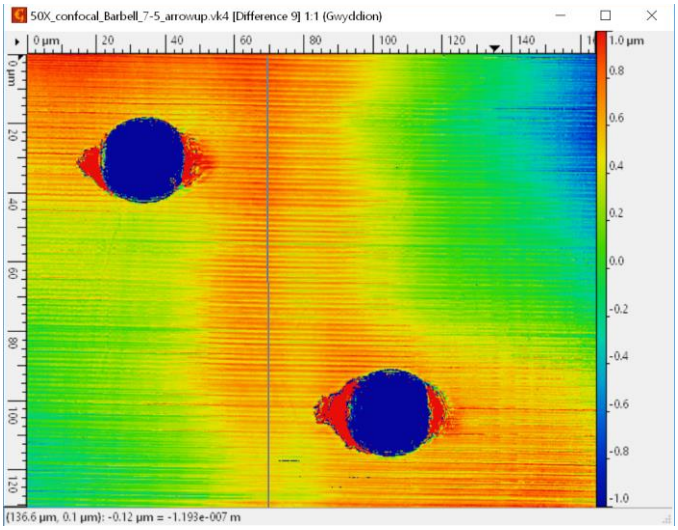

Figure 6-13. **Ra=73 nm**

Mykonos-10199:

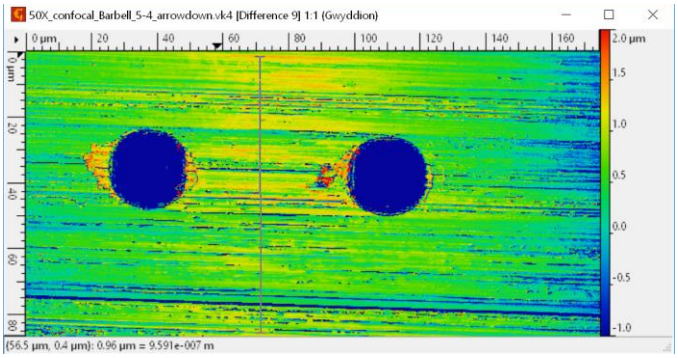

Figure 6-14. **Ra=361 nm**

Results from the first 6 experiments:

In this section, we show data from the first 6 engineered defect experiments executed on the Mykonos facility. Analysis has only begun and is far from complete. Data from two ICCD cameras are shown. The two cameras viewed the same defect pattern, as they used the same long distance microscope for imaging, with a 50-50 pellicle splitter used to direct light to the two independent cameras. Pre-shot images were gathered (long integration time) to ensure that the defect pattern was facing the desired diagnostic line of sight. Fig. 6-15 shows one such pre-shot image, next to its companion experimental image, to exemplify the utility of this technique.

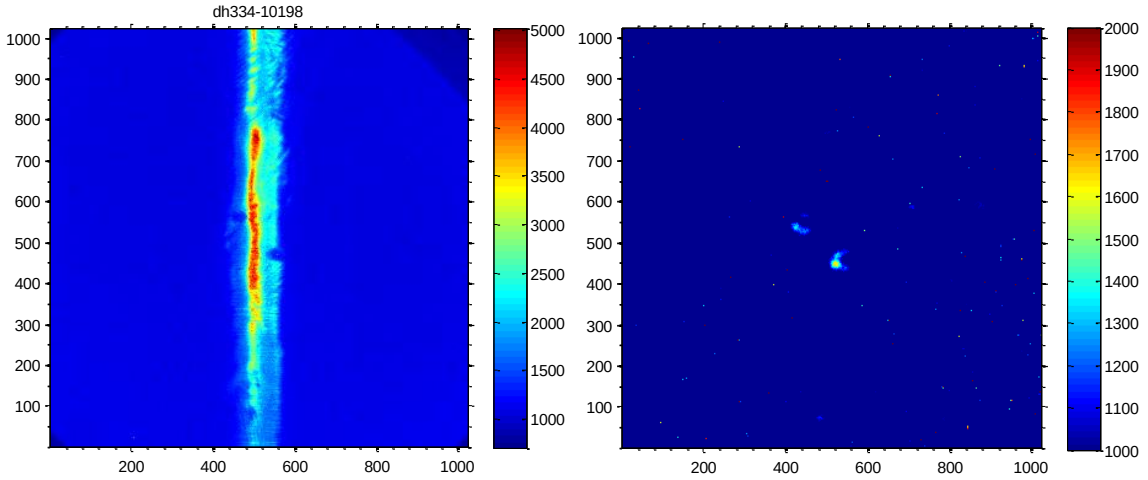

Figure 6-15. (Left): Pre-shot image of the barbell load, with engineered defects observable within the bright band of reflected light. (Right): Corresponding shot data from the same instrument, with the engineered defects displaying bright emissions versus the background smooth cylindrical surface.

The timing, and thus machine current, associated with each image is still being precisely determined, but in general, the images associated with the Andor-340 (rectangular image) camera are gathered later than those images from the Andor-334 camera (square image). All experimental images captured are shown below.

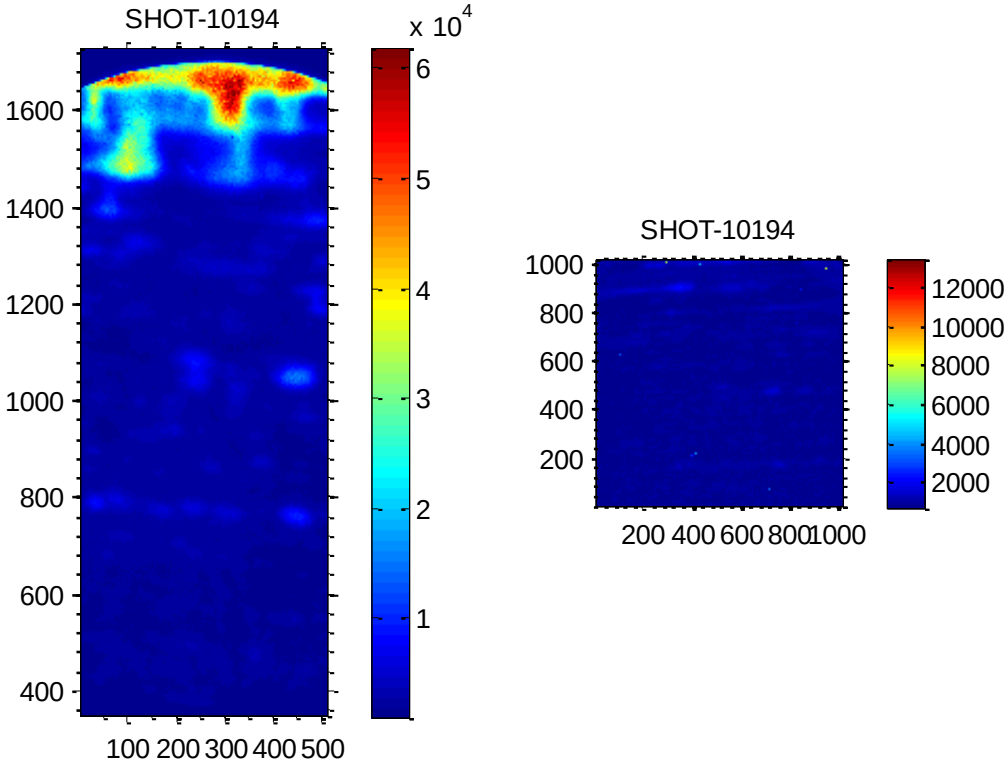

Figure 6-16. ICCD data from Mykonos shot 10194.

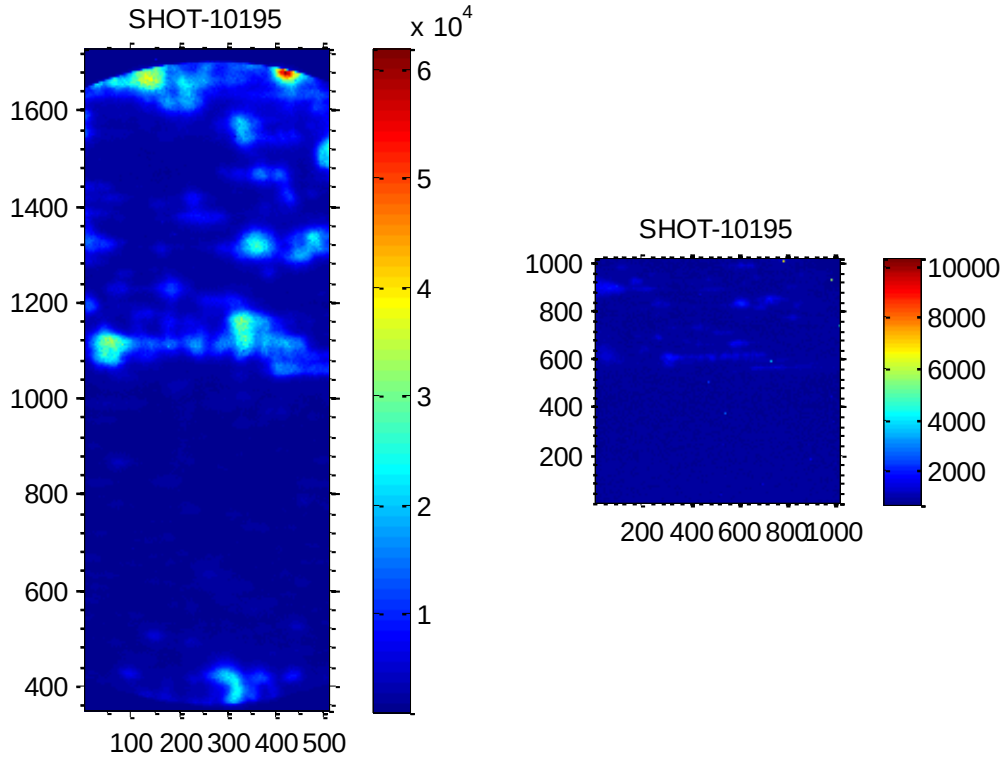

Figure 6-17. ICCD data from Mykonos shot 10195.

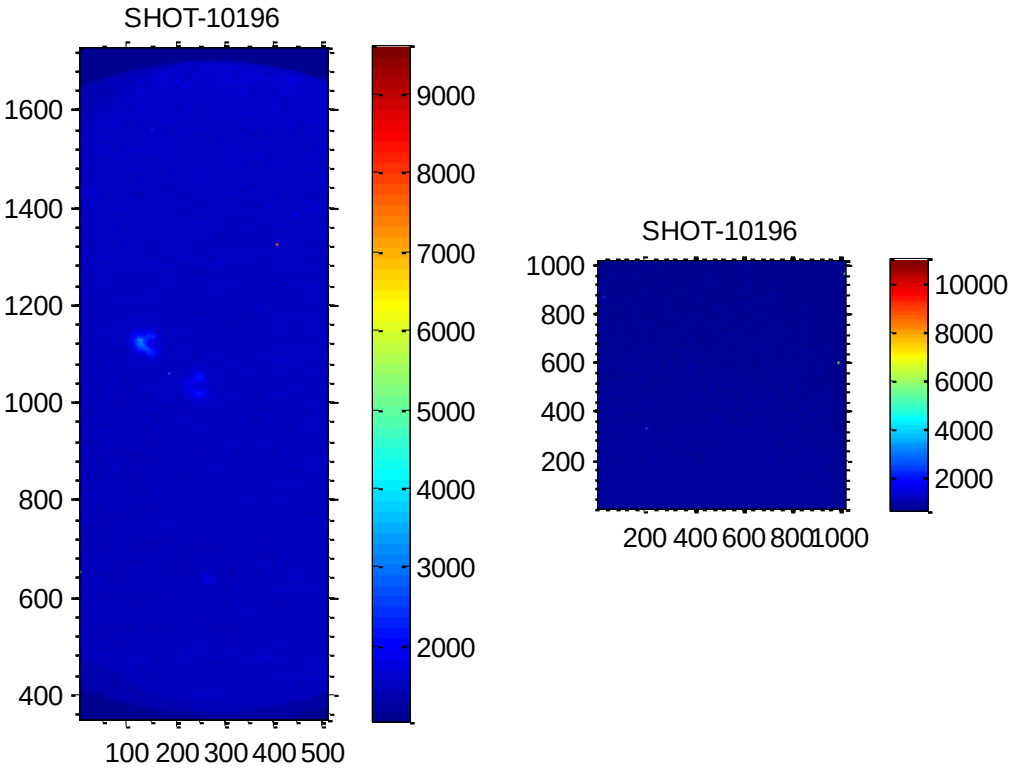

Figure 6-18. ICCD data from Mykonos shot 10196

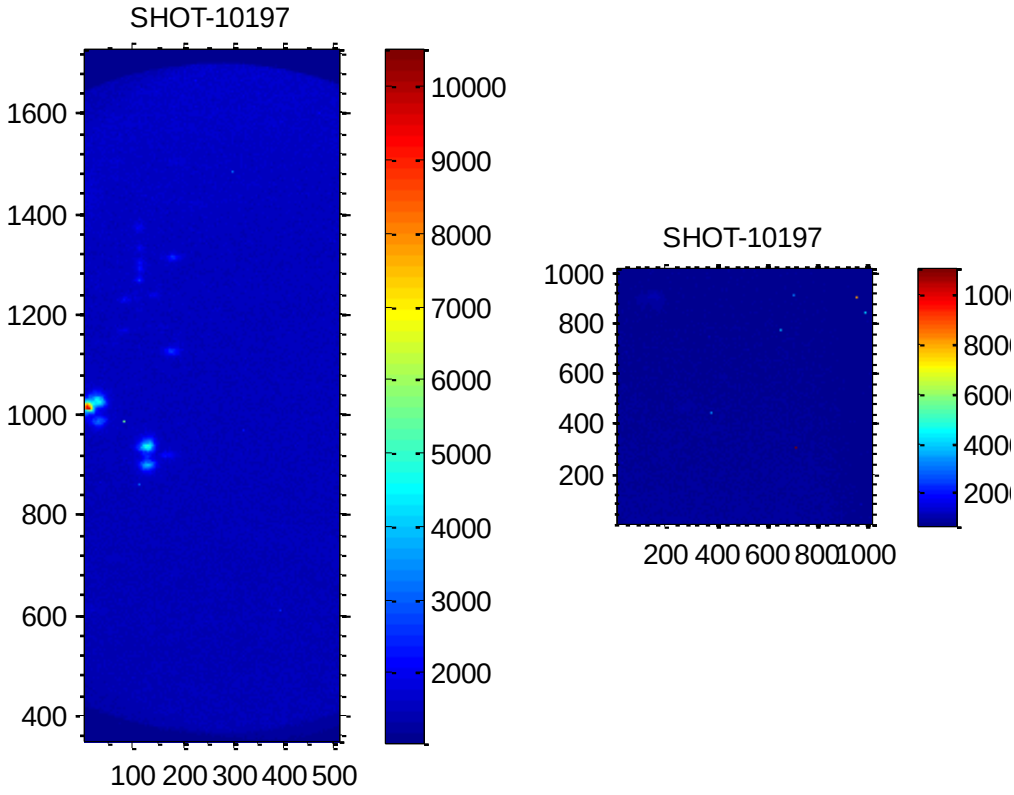

Figure 6-19. ICCD data from Mykonos shot 10197.

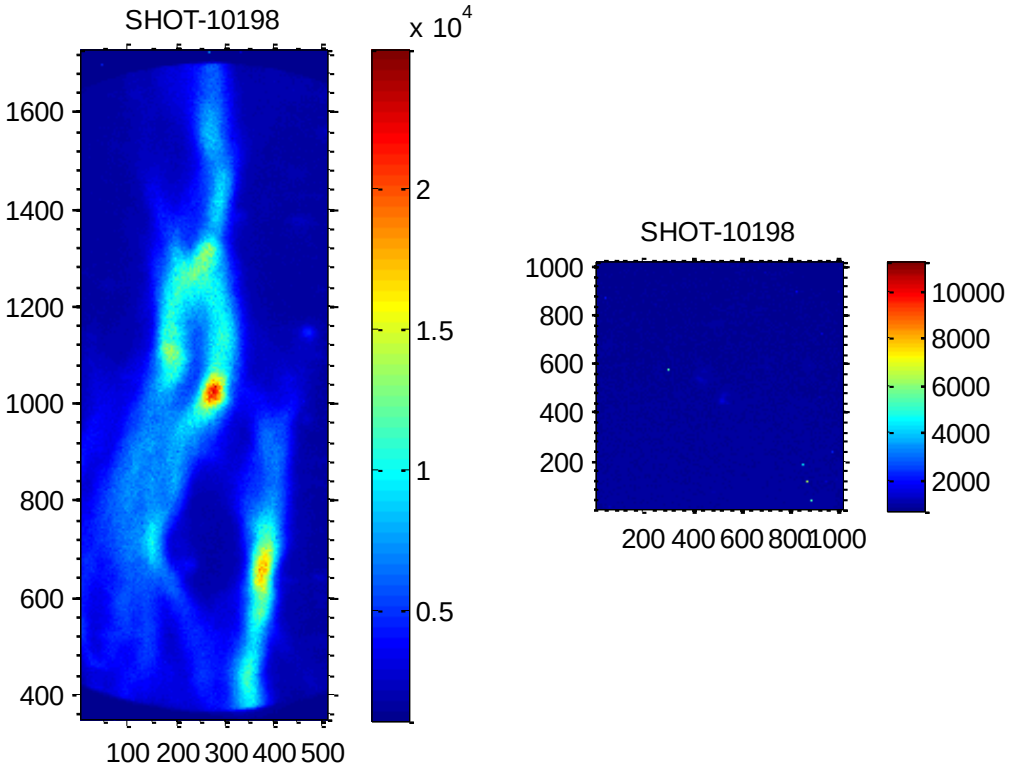

Figure 6-20. ICCD data from Mykonos shot 10198.

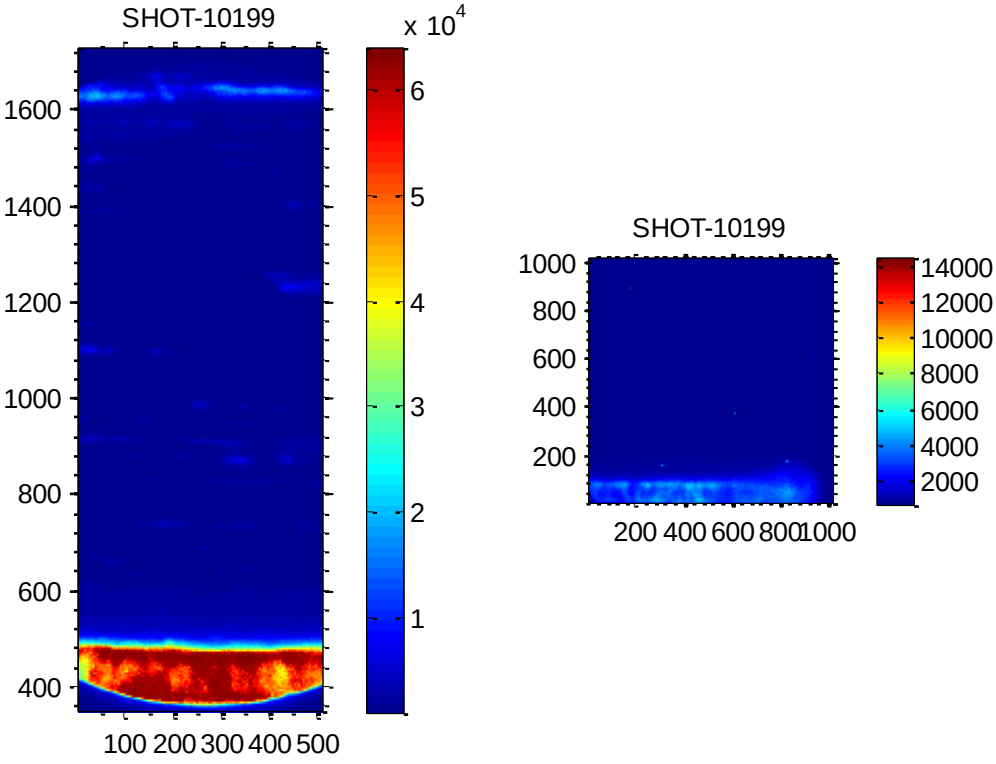

Figure 6-21. ICCD data from Mykonos shot 10199.

Of the 6 experiments, all captured self-emission from the rod surface, demonstrating that the pulsed power and imaging diagnostics performed nominally. 3 experiments saw observable emissions generated from the engineered defects, whereas for the remaining 3 targets, any emissions that may have been generated from the engineered defects were overwhelmed by emissions from the neighboring background metal. The table below indicates that the roughness of the neighboring background metal plays an important role in determining whether the engineered defects drive the most rapid surface heating.

Shot number	Ra [nm]	Comment on emission grooves
10194	397	Select machining grooves
10195	533	Select machining grooves; different top/bottom
10196	81	Defects
10197	57	Defects
10198	73	Defects
10199	361	Select machining grooves

Table 6-4. Catalog of surface roughness and emission structure.

Based on this limited data set, there appears to be a correlation between background surface roughness and emission structure, where, if the surface roughness is too large, the background metal overheats more rapidly than the engineered defects. Presumably, once the image timing has been verified, the data will show that rougher surface generate observable emissions at slightly lower current. To enable detailed comparisons with the simulations presented above, it was necessary to improve the surface finish so that emissions from the engineered defects are observed. Therefore, we requested that future loads be machined to a final diameter of 1.0 mm, rather than 800 microns. By increasing the rod diameter, and thus the stiffness off the target during machining, the surface roughness can be reduced. This change was extremely effective. Characterization data from a 1.0 mm diameter load with Ra~5 nm is shown below.

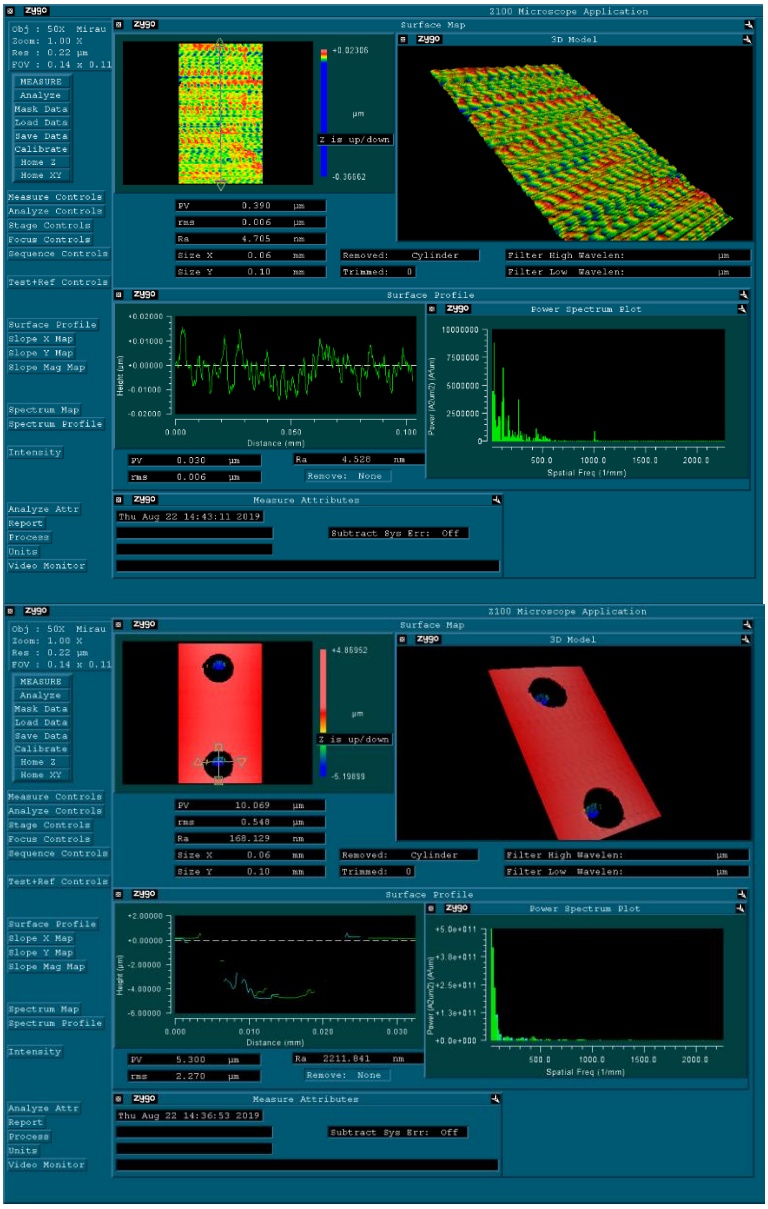

Figure 6-22. Characterization data from an ultra-smooth 1.0 mm diameter barbell with burr-free engineered defects.

Next, we briefly discuss data from Mykonos shot 10197, where the target was sufficiently smooth to enable direct observation of overheating from the engineered defects. At the time of this writing, analysis is far from complete, however, comparison of the pre-shot characterization data and the experimental self-emission does suggest that the burrs on the edge of the defect where the diamond tip exits during machining result in appreciable overheating. In the pre-shot characterization data shown below, it is clear that both defects have burrs on the left-hand side, as well as an artifact on the right-hand side. All rise above the background surface by 1 to 1.5 microns. Detailed understanding of the burr cannot be gained from this dataset. For example, it is unclear whether the burr is a "pile" of metal or a "fin" of metal. The burr on left side of the upper defect is 3 to 4 times larger in surface area than the burr on the left side of the lower

defect. The self-emission data shows stronger emissions from left side of the upper burr, versus the left side of the lower burr, suggesting that the burr itself is overheating.

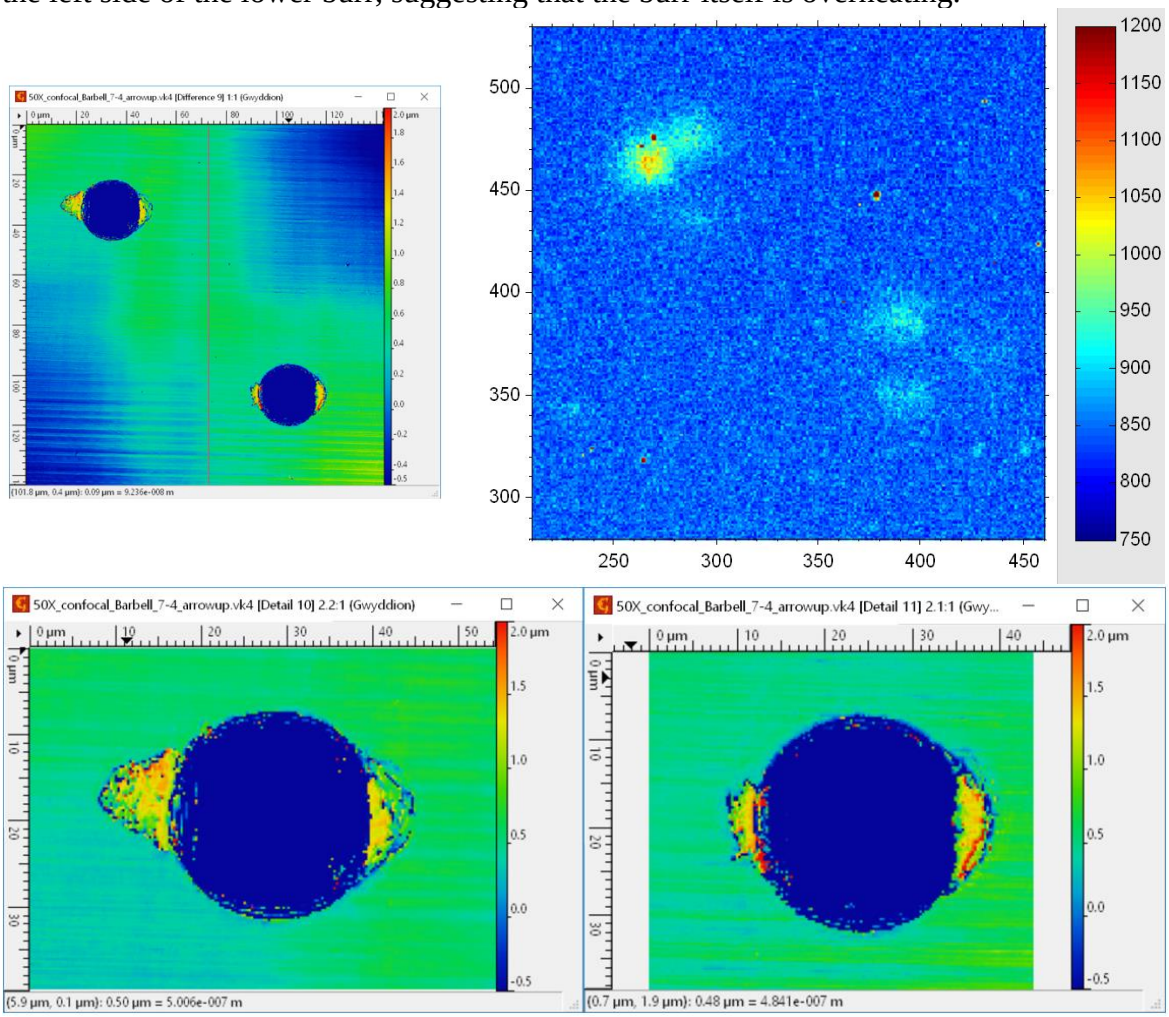

Figure 6-23. When comparing self-emission data (upper right) to pre-shot characterization data, it appears that the burrs at the edges of the defect are resulting in overheating.

While understanding the evolution of burrs is clearly important from a practical perspective (electrodes and targets often contain micron-scale burrs), the presence of these burrs complicates experimental interpretation. Furthermore, the burrs will be challenging to properly characterize. Since the objective of this experimental series was to study targets with idealized defects which can be carefully characterized and then compared with simulations, it is desirable to eliminate the burrs. To that end, the GA team modified the machining process in the following way. First, the barbell profile was cut. Second, the defects were cut (with burrs generated along select edges). Third, and additional 200 nm of material was removed from the entire central rod surface, removing all burrs. This process was extremely effective (see Fig. 6-22), and all subsequent loads were machined via this process.

Future work:

By the end of the project, we expect to have nearly 30 burr-free engineered defect loads of the various designs specified in table 6-2 but with D=1.0mm. We expect most loads will have Ra~10 nm. Experiments are planned for January of 2020, where we will study the overheating from these loads. Based on the 6 engineered defect experiments that have already been fielded, we expect the engineered defects to be the dominant current-density perturbation, and we further expect the data to lend itself to detailed comparison with simulation, since the burrs (of uncertain geometry) have been eliminated. In these experiments we also intend to study larger diameter defects to test the hypothesis of self similar heating.

Assuming success with these experiments, the remain loads will be used to determine the impact of embedded "engineered inclusions." An engineered inclusion is simply an engineered pit which has been backfilled with a resistive material such as epoxy. While the epoxy will carry essentially no current (like the vacuum in the engineered pit), when the pit surface overheats and expands, the expansion will be tamped by the mass of the epoxy. Simulations suggest this will impact the heating evolution in a diagnoseable way.

Finally, loads with engineered inclusions will be surface coated with 10s of microns of aluminum to create "buried engineered inclusions." In these experiments, we will determine how the thin film of metal located directly above a buried resistive inclusion heats and evolves.

REFERENCES

[1] E. G. Harris, Phys. Fluids 5, 1057 (1962).

[2] Y. Y. Lau, J. C. Zier, I. M. Rittersdorf, M. R. Weis, and R. M.Gilgenbach, Phys. Rev. E 83, 066405 (2011).

[3] S. A. Slutz, M. C. Herrmann, R. A. Vesey, A. B. Sefkow, D. B. Sinars, D. C. Rovang, K. J. Peterson, and M. E. Cuneo, Phys. Plasmas 17, 056303 (2010).

[4] S. A. Slutz and R. A. Vesey, Phys. Rev. Lett. 108, 025003 (2012).

[5] M. E. Cuneo, M. C. Herrmann, D. B. Sinars, S. A. Slutz, W. A. Stygar, R. A. Vesey, A. B. Sefkow, G. A. Rochau, G. A. Chandler, J. E. Bailey, J. L. Porter, R. D. McBride, D. C. Rovang, M. G. Mazarakis, E. P. Yu, D. C. Lamppa, K. J. Peterson, C. Nakhleh, S. B. Hansen, A. J. Lopez, M. E. Savage, C. A. Jennings, M. R. Martin, R. W. Lemke, B. W. Atherton, I. C. Smith, P. K. Rambo, M. Jones, M. R. Lopez, P. J. Christenson, M. A. Sweeney, B. Jones, L. A. McPherson, E. Harding, M. R. Gomez, P. F. Knapp, T. J. Awe, R. J. Leeper, C. L. Ruiz, G. W. Cooper, K. D. Hahn, J. McKenney, A. C. Owen, G. R. McKee, G. T. Leifeste, D. J. Ampleford, E. M. Waisman, A. Harvey-Thompson, R. J. Kaye, M. H. Hess, S. E. Rosenthal, and M. K. Matzen, IEEE Trans. Plasma Sci. 40, 3222 (2012).

[6] A.B.Sefkow, S.A. Slutz, J.M. Koning, M.M. Marinak, K.J. Peterson, D.B. Sinars, and R.A. Vesey, Phys. Plasmas 21, 072711 (2014).

[7] M. R. Gomez et al. Phys. Rev. Lett. 113, 155003 (2014).

[8] D.B. Sinars, et al. Phys. Plasmas 18, 056301 (2011).

[9] R. D. McBride et al., Phys. Rev. Lett. 109, 135004 (2012).

[10] R. D. McBride, M. R. Martin, R. W. Lemke, J. B. Greenly, C. A. Jennings, D. C. Rovang, D. B. Sinars, M. E. Cuneo, M. C. Herrmann, S. A. Slutz, C. W. Nakhleh, D. D. Ryutov, J.-P. Davis, D. G. Flicker, B. E. Blue, K. Tomlinson, D. Schroen, R. M. Stamm, G. E. Smith, J. K. Moore, T. J. Rogers, G. K. Robertson, R. J. Kamm, I. C. Smith, M. Savage, W. A. Stygar, G. A. Rochau, M. Jones, M. R. Lopez, J. L. Porter, and M. K. Matzen, Phys. Plasmas 20, 056309 (2013).

[11] K.J. Peterson, T.J. Awe, E.P. Yu, D.B. Sinars, E.S. Field, M.E. Cuneo, M.C. Herrmann, M. Savage, D. Schroen, K. Tomlinson, and C. Nakhleh, Phys. Rev. Lett. 112, 135002 (2014)

[12] T.J. Awe, K.J. Peterson, E.P. Yu, R.D. McBride, D.B. Sinars, M.R. Gomez, C.A. Jennings, M.R. Martin, S.E. Rosenthal, D.G. Schroen, A.B. Sefkow, S.A. Slutz, K. Tomlinson, R.A. Vesey, Phys. Rev. Lett. 116, 065001 (2016).

[13] D. Ryutov,M. Derzon, and M. Matzen, Rev. Mod. Phys. 72, 167 (2000).

[14] K. J. Peterson, D. B. Sinars, E. P. Yu,M. C. Herrmann, M. E. Cuneo, S. A. Slutz, I. C. Smith, B.W. Atherton, M. D.

Knudson, and C. Nakhleh, Phys. Plasmas 19, 092701 (2012).

[15] V. Oreshkin, R. Baksht, N. Ratakhin, A. Shishlov, K. Khishchenko, P. Levashov, and I. Beilis, Phys. Plasmas 11, 4771 (2004).

[16] V. Oreshkin, Tech. Phys. Lett. 35, 36 (2009).

[17] V. I. Oreshkin, Phys. Plasmas 15, 092103 (2008).

[18] A. G. Rousskikh, V. I. Oreshkin, S. A. Chaikovsky, N. A. Labetskaya, A. V. Shishlov, I. I. Beilis, and R. B. Baksht, Phys. Plasmas 15, 102706 (2008).

[19] K. J. Peterson, E. P. Yu, D. B. Sinars, M. E. Cuneo, S. A. Slutz, J. M. Koning, M. M. Marinak, C. Nakhleh, and M. C. Herrmann, Phys. Plasmas 20, 056305 (2013).

[20] J.D. Pecover and J.P. Chittenden, Phys. Plasmas 22, 102701 (2015).

[21] K. J. Peterson, D. B. Sinars, E. P. Yu,M. C. Herrmann, M. E. Cuneo, S. A. Slutz, I. C. Smith, B.W. Atherton, M. D.

Knudson, and C. Nakhleh, Phys. Plasmas 19, 092701 (2012).

[22] T.M. Hutchinson, T.J. Awe, B.S. Bauer, K.C. Yates, E.P. Yu, W.G. Yelton, and S.

Fuelling, Phys. Rev. E 97, 053208 (2018).

[23] T. J. Awe, E. P. Yu, K. C. Yates, W. G. Yelton, B. S. Bauer, T. M. Hutchinson, S. Fuelling, and B. B. McKenzie, IEEE Trans. Plasma Sci. 45, 584 (2017).

[24] A. C. Robinson, et al., in Proceedings of the 46th AIAA Aerospace Sciences Meeting and Exhibit, Reno, NV, 7–10 January 2008, Paper No. AIAA-2008-1235, see http://arc.aiaa.org/doi/abs/10.2514/6.2008-1235

[25] K.J. Peterson, T.J. Awe, E.P. Yu, D.B. Sinars, E.S. Field, M.E. Cuneo, M.C. Herrmann, M. Savage, D. Schroen, K. Tomlinson, and C. Nakhleh, Phys. Rev. Lett. 112, 135002 (2014)

[26] T.J. Awe, K.J. Peterson, E.P. Yu, R.D. McBride, D.B. Sinars, M.R. Gomez, C.A. Jennings, M.R. Martin, S.E. Rosenthal, D.G. Schroen, A.B. Sefkow, S.A. Slutz, K. Tomlinson, R.A. Vesey, Phys. Rev. Lett. 116, 065001 (2016).

[27] P. Rahimi and C.A Ward, Int. J. of Thermodynamics, 8, 1-14 (2005).

[28] D.M. Murphy and T. Koop, Q. J. R. Meteorol. Soc. 131, 1539-1565 (2005).

[29] B.J. Kim and E. Meng. Polymers for Adv. Tech. 2016, 27 564–576 (2015).

[30] R. Castaneda and J. Garcia-Sucerquia, Applied Optics 57, A12 (2018).

[31] G. Hass, J. of the Optical Soc. of America. 39, 532 (1949).

[32] http://gwyddion.net/

[33] V. I. Oreshkin, Phys. Plasmas 15, 092103 (2008).

[34] D. Ryutov,M. Derzon, and M. Matzen, Rev. Mod. Phys. 72, 167 (2000).

[35] K. J. Peterson, D. B. Sinars, E. P. Yu,M. C. Herrmann, M. E. Cuneo, S. A. Slutz, I. C. Smith, B.W. Atherton, M. D. Knudson, and C. Nakhleh, Phys. Plasmas 19, 092701 (2012).

[36] V. Oreshkin, R. Baksht, N. Ratakhin, A. Shishlov, K. Khishchenko, P. Levashov, and I. Beilis, Phys. Plasmas 11, 4771 (2004).

[37] V. Oreshkin, Tech. Phys. Lett. 35, 36 (2009).

[38] V. I. Oreshkin, Phys. Plasmas 15, 092103 (2008).

[39] A. G. Rousskikh, V. I. Oreshkin, S. A. Chaikovsky, N. A. Labetskaya, A. V. Shishlov, I. I. Beilis, and R. B. Baksht, Phys. Plasmas 15, 102706 (2008).

[40] K. J. Peterson, E. P. Yu, D. B. Sinars, M. E. Cuneo, S. A. Slutz, J. M. Koning, M. M. Marinak, C. Nakhleh, and M. C. Herrmann, Phys. Plasmas 20, 056305 (2013).

[41] J.D. Pecover and J.P. Chittenden, Phys. Plasmas 22, 102701 (2015).

APPENDIX A. PDV MANUSCRIPT DRAFT

Photonic Doppler velocimetry of ohmically-exploded aluminum surfaces

T.M. Hutchinson[1,*], T.J. Awe[2], B.S. Bauer[1], D.H. Dolan[2], S.L. Payne[3], J.R. Pillars[2], B.T. Hutsel[2], E.P Yu[2], and S. Kreher[1]

[1]*University of Nevada, Reno, Nevada 89506, USA*
[2]*Sandia National Laboratories, Albuquerque, New Mexico 87185, USA*
[3]*MSTS, Albuquerque, New Mexico 87131, USA*

Photonic Doppler Velocimetry was used to measure the exploding surface of coated thick metal driven by lineal current density $3\times10^{15}\ A/m/s$. Aluminum-6061 rods were coated with three thicknesses (5, 17, and 41 μm) of Parylene-N and driven to 850 kA in 100 ns, with the metal thicker than the skin depth. The metal surface melts at $85 \pm 13\ T$ and expands at a constant acceleration $10 - 16$ m/s/ns that depends on coating thickness. Then, at the time of metal vaporization, at surface magnetic field 164 ± 20 T, the metal acceleration begins to linearly increase in time. Later, plasma forms for aluminum coated with only 5 μm and 17 μm of dielectric, but is suppressed for $41 - \mu m$-coated metal.

The electrical explosion of a thick metal is an exceptionally complex process, involving the transformation of a cold solid metal to a $10 -$ eV plasma[1] in 50 ns on $\mu m - mm$ length scales. Accurate magnetohydrodynamic (MHD) modelling of this process requires transport properties for warm dense matter (WDM), the prediction of which further requires a full many-body quantum mechanical treatment at atomic scales[2]. A simple-to-state, but important prediction from such modelling is the time-resolved velocity of the metal surface, an historically challenging process to accurately model in part due to limited experimental data, equation of state (EOS) uncertainties, and numerical difficulties in modelling matter-vacuum interfaces[3, 4]. Existing experimental surface evolution data, whether inferred from self-emission[5, 6] or shadowgraphy[7, 8], shows an acceleration from a static surface to a constant velocity sufficiently fast to have been unresolved. Only recently, using Velocity Interferometry for Any Reflector (VISAR), has the time-resolved surface velocity of current-carrying conductors been directly diagnosed[9], while the surface expansion velocity of dielectric-coated metal has never been measured, until now. Finally, dielectric-coatings are increasingly being used to mitigate instabilities in magnetically accelerated systems[10, 11], and therefore it is valuable to understand the full range of effects that accompany their use.

The surface velocity of a current-carrying conductor was made with Photonic Doppler Velocimetry (PDV), a heterodyne optical diagnostic capable of resolving km/s velocities of reflective objects with better than ns precision[12, 13]. PDV is typically fielded to measure breakout velocities of shock-driven surfaces for dynamic compression research[14], and more recently to infer z-pinch load currents by measuring the back-anode surface[15], but has never been used on current-carrying surfaces to diagnose surface expansion from ohmic heating. The diagnostic can simultaneously resolve multiple velocities, where standard implementations of its homodyne counterpart VISAR lose contrast. In addition, PDV is robust to misalignment and target roughness, tolerating worse than 40 dB return losses[16, 17]. These capabilities make it the diagnostic of choice for evaluating ohmically-heated surfaces, and an improvement on recent VISAR measurements[9].

Aluminum rods with diameter 789 ± 9 μm were electrically connected to the Mykonos Linear Transformer Driver (LTD)[18], which delivers 850 kA in 100 ns (Fig 3). At the initiation of the current pulse, the current I rises exponentially with coefficient 0.12 ± 0.02 ns^{-1} to ~ 70 kA, then linearly with rate 8.8 ± 0.2 kA/ns until 700 kA, when $\dot{I}$ decreases and finally changes sign at 165 ns and 850 kA. The experimental time of interest is during the linear rise, from 100-700 kA, when the current pulse is most reproducible. During this time, the electrical skin depth is much thinner than the rod diameter (this defines *thick*), and the current density $\vec{j}$ non-linearly diffuses into the metal, leading to an electrical explosion of the metal surface, an inward-moving magnetic diffusion wave, and an associated inward-moving hydrodynamic shock wave[19, 20] that outpaces it. Previous research has demonstrated that bare metal surfaces form plasma at specific surface magnetic field thresholds[21], and that dielectric coatings suppress plasma formation[22] and tamp expansion[23], facilitating diagnosis of the WDM underneath the coatings.

Metallic targets were extensively characterized prior to experimentation. Aluminum 6061-T6 stock was machined on a lathe to form the rods; premeditated specification of lathe feed rates (specifically the helical pitch of the cutting tool relative to the rod, 5 μm and 30 μm) allowed the wavelength of residual, lathe-generated machining marks on the metal surface to be controlled. Indeed, Scanning Electron Microscope (SEM) and confocal microscope investigation of the rods revealed two distinct classes of surface finish, which are identified as short and long (see Fig. 1f), with dominant wavelengths 5.1 μm and 30.4 μm (Fig. 1f, approximate modal depth 150 nm) and R_a surface roughness 428 ± 57 nm and 584 ± 97 nm respectively. More details about the Fourier modes are in the Fig. 1 caption. There were 18 rods in each of the short and long rod classes.

Metal topography was additionally controlled via two electrochemical surface finishing methods. The first method, identified as Pulsed-Oxide Electropolishing (PO-EP), was applied to all rods. For this first method, 3% by mass tartaric acid ($C_4H_6O_6$) is added to deionized water to reach 150 mL total. Ammonium hydroxide (NH_4OH) is added to reach pH = 5.5, and oxygen is bubbled through. Rods were immersed at room temperature and held at -30 V relative to the metal beaker for 2 minutes. This anodization forms an aluminum oxide (Al_2O_3) layer that passivates further electrochemical activity. Rods are removed, rinsed, and etched for ten minutes in a chromic acid chemistry (0.4M H_3PO_4 with 0.2M CrO_3) at $T = 60$ ° C, which dissolves Al_2O_3 and other oxides but does not affect pure aluminum. Overall, the process removes non-metallic inclusions and smooths the surface. The R_a specified earlier (and Fourier spectra in Fig. 1f) for the short and long machining classes corresponds to that after the PO-EP process. Since very little (estimated 600 nm) Aluminum was removed from the surface, the machining structure is intact – this can be seen in post-PO-EP characterization, Figs. 1a-d.

The second electrochemical method, identified as PEG-EP (Polyethylene Glycol Electropolishing), was only applied to 7 long-wavelength-machining rods (applied in addition to and after PO-EP). For this second method, a total volume of 200 mL of 60% phosphoric acid (only 85%, remaining 15% water) and 40% polyethylene glycol was heated to $T = 85$ ° C. Rods were submerged and held at $+1$ V relative to the beaker for 100 ms, then at -400 mV for 900 ms. This 1000-ms process is defined as one cycle, and 350 cycles were applied, leading to a measured surface roughness R_a of 410 ± 101 μm (R_a were measured with confocal microscopy). PEG-EP was largely successful in erasing the surface machining structure (although some residual machining did remain on the surface [Fig. 1e]), ultimately removing 21 μm of aluminum from the surface (determined by SEM). PEG-EP exposed numerous metallurgical defects in the metal (inclusions, see Fig. 1e), determined by Energy Dispersive

Spectroscopy (EDS) to be composed of Al6061 alloying elements – Silicon, Magnesium, Iron, and Manganese.

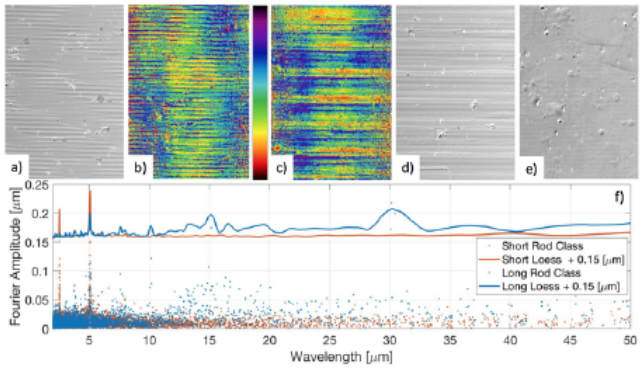

Figure 1 (color). Representative SEM and confocal images of aluminum surfaces before coating, together with spectral information. a) SEM image of short machining b) Confocal image of short machining, c) confocal image of long machining, d) SEM image of long machining, e) SEM image of PEG-EP, and f) Fourier amplitudes from confocal data; dots correspond to Fourier amplitudes in μm calculated from confocal micrographs of all rods in each surface wavelength class (11 long and 18 short), together with smoothed Loess fits (continuous lines, upshifted by 150 nm for visibility). Class composition was determined by eye, then corroborated with Fourier amplitudes. Fourier amplitudes correspond to data averaged over an azimuthal width of 35 μm – this mitigate noise but is narrow enough to avoid errors due to averaging over the helical structure of machining. SEM images were captured at 15 kV with secondary electrons. Confocal and SEM images are all 200 μm × 137 μm. The colorbar applies to confocal images (b, c) and denotes ± 2.5 μm surface displacement. No images are of the same surface.

Chemical vapor deposition (CVD) was used to conformally coat all rods with different thickness of an insulating, transparent[24] dielectric. First, the dimer di-p-xylylene is sublimated at 1 torr and 150 ° C. Second, the dimer vapors are split at 0.5 torr and 680 ° C into monomer units. Third, the monomer vapor flows to a room-temperature chamber (0.1 torr) where it self-polymerizes into Parylene-N [$(C_8H_8)_n$, poly(p-xylylene)] on rod surfaces. This is known as the Gorham process[25]. Since the aluminum remains at room temperature during the deposition, the aluminum surfaces are not expected to be modified by the CVD procedure from those shown in Fig 1. Rods with short machining structure were coated with Parylene-N to three different thicknesses, δ_p: 5.0 ± 1.4 μm, 17.0 ± 1.2 μm, and 41.2 ± 1.3 μm, with 6 rods in each class. Dielectric thicknesses were measured on 'witness' tungsten rods (to prevent damaging the dielectric surfaces on rods in experiments) with precision micrometers, and error bars denote the standard deviation across 4 different tungsten rods in the same coating batch as rods used in experiments. The 7 PEG-EP rods, and the remaining 11 long-wavelength rods batch were coated with Parylene-N to a thickness of 41.2 ± 1.3 μm. These processes created 6 classes of rod: short machining with three different coating δ_p, PEG-EP and long-machining surfaces with the thickest coating, and uncoated (with PEG-EP surfaces).

Diagnosis of the metal evolution during the Mykonos current pulse relied on an imaging photodiode (magnification $M = 15$) to measure time-resolved self-emission from the metal surface, two single-frame time-gated Intensified Charge Coupled Devices (ICCDs) to observe high-resolution surface emission features, and PDV to measure time-resolved surface velocities of the expanding metal.

The PDV diagnostic used a 1550-nm 35-mW probe laser, fiber-coupled to an achromatic optics imaging system. The optics were aligned to yield a full width half maximum (FWHM) 53 ± 5 μm spot size on the aluminum surface. The optical system was designed to be limited by the fiber $NA = 0.14$, and calculations showed optimal return signals for spot sizes on the metal

significantly larger than diffraction limited[26]. By imaging $633-$ nm specular reflections off a rod, a FWHM was measured of the spot size. An equivalent FWHM at $\lambda_0 = 1550$ nm is inferred based on achromatic optics (accurate to XYZ% via Zemax?). Probe laser light was retro-reflected off the metal surface back to two non-polarization-preserving single-mode receive fibers (Channels 1 and 2). Laser light from a ~1 mW reference laser with frequency f_{LO} was set $f_{het} = 2$ GHz lower than the probe laser, $f_{LO} = f_0 - f_{het}$ via thermal tuning, and added with optical splitters to each of the two signals, after reflection from the metal. The resulting intensity was measured with an 18-GHz-bandwidth photodiode and digitized by a DSOS804A oscilloscope (8 GHz bandwidth) at 20 GS/s. Since the recorded intensity is proportional to the electric field squared, the term representing interference between electric fields from the reference laser and the reflected light (the cross term) contains the product of two sinusoidal functions. This term is mathematically equivalent to the superposition of sum and difference frequencies. The sum frequency is 387 THz (far outside the digitizer bandwidth), while the difference frequency is f_{het} plus the Doppler shift. For a reflector much slower than the speed of light, the relativistic Doppler shift of the reflected light can be linearized as $\bar{f} = 2f_0 v^*/c$, where v^* is the apparent velocity of the reflector, and c the speed of light. We find the frequency shift $\bar{f} = f - f_0$ from the raw recorded interference frequency by first subtracting the initial f_{het} shift of the probe laser relative to the reference laser. The resulting frequency deviations $\bar{f}$ indicate reflective matter moving parallel to the probe laser (normal to the metal surface) with a velocity of:

$$v^* = \frac{\lambda_0}{2}\bar{f}. \qquad (1)$$

In analyzing PDV signals, we consider both the Doppler shift from the moving aluminum and the optical path length change in the dynamically compressed Parylene-N. We will neglect corrections (presumed small) associated with non-paraxial beams, reflections from the Parylene, and dispersion in collection optics. The effects of dynamic compression only apply for coated rods and are contained in the apparent velocity v^*, which differs from the true metal velocity by the rate of optical path length change via

$$v^*(t) = v_s(t) - \frac{d}{dt}\left[\int_{x(t)}^{x_s(t)} n(x',t)dx'\right], \qquad (2)$$

where $n(x',t)$ is the refractive index of the Parylene-N, $v_s(t)$ is the velocity of the surface of the Parylene-N exposed to vacuum (the free surface), $v(t)$ and $x(t)$ correspond to the true metal-dielectric interface velocity and position respectively, and $v^*(t)$ is the apparent metal velocity[27, 28] measured by PDV. Spatial coordinates increase radially outwards from the rod. Since the dielectric's index of refraction varies with density, the phase (frequency) of the light making the round-trip transmission through it is also expected to vary. The dependence of $n(x',t)$ with temperature has been neglected in this analysis, although the dielectric is not expected to carry current and appreciably heat[22]. Applying the Leibniz integral rule to Eq. (2), rearranging, and applying the chain rule with the mass density ρ as an intermediate variable to the integrand,

$$v(t) = \frac{1}{n(x(t),t)}\left\{v^*(t) + v_s(t)\left[n\left(t, x_s(t)\right) - 1\right] + \int_{x(t)}^{x_s(t)} \frac{\partial n(x',t)}{\partial \rho(x',t)}\frac{\partial \rho(x',t)}{\partial t}dx'\right\}. \qquad (3)$$

This indicates that the true metal velocity $v(t)$ may be bigger or smaller than the apparent velocity $v^*(t)$, depending on the evolution of the load. According to the rearranged Lorentz-Lorenz equation, applicable for solid dielectrics[29], the refractive index of the Parylene-N behaves as

$$n(\rho) = \sqrt{\frac{8\pi\rho\alpha + 3M\varepsilon_0}{3M\varepsilon_0 - 4\pi\rho\alpha}}. \quad (4)$$

This indicates that $n(\rho)$ monotonically-increases with density, so $\partial n(x',t)/\partial\rho(x',t)$ is always positive (where α is Parylene-N's molecular polarizability[36] 26.5 Å^3, and M its molecular mass 3.46×10^{-25} kg/molecule. Before mechanical waves generated by the moving aluminum reach the free surface, v_s is zero, the dielectric cannot decompress, and the integral in Eq. 3 is positive and adds to $v^*(t)$. In general, the terms in the sum are typically positive [as $n(t, x_s(t)) > 1$], increasing $v(t)$, but the denominator $n(x(t),t) > 1$, decreasing $v(t)$.

To determine the velocity of the surface, the raw intensity data must be converted to the amount of each frequency at each time. First, the data from each channel (e.g., Fig. 2a) is divided into 3.2 ns blocks (δt). Grouping three blocks together into a $3\delta t$-wide window, the data is multiplied with a Hamming windowing function $3\delta t$ wide and Fourier transformed. A windowing function was chosen to redistribute spectral leakage to distal sidelobes, and a Hamming window represents an intermediate choice between full attenuation at the window boundaries (temporal fidelity) and using all data points per window (spectral fidelity)[30, 31]. At the time-center of the window, the power spectral density (PSD) is reported, where color denotes dB from the maximum power[32]. Repeating this process at sequential time-centers (shifted forward by time increment δt), subtracting off the f_{het} baseline, and scaling the vertical frequency axis by Eq. 1, Short-Time Fourier Transform (STFT) spectrograms (e.g., Fig. 2 b-e) are constructed. Since the increment and column widths are equivalent, but an FFT sources data from a window $3\delta t$ wide, there is δt overlap in the data represented by neighboring FFT columns. Columns separated by more than δt contain no shared information. A synthetic PDV input containing a linear frequency chirp beginning at a known time was used to confirm that the use of overlap does not correspond to artificially shifted PSD maxima denoting frequency turn-on times (to much better than other timing uncertainties). The overlap procedure improves the signal to noise ratio (SNR) and the frequency resolution, facilitating later analysis.

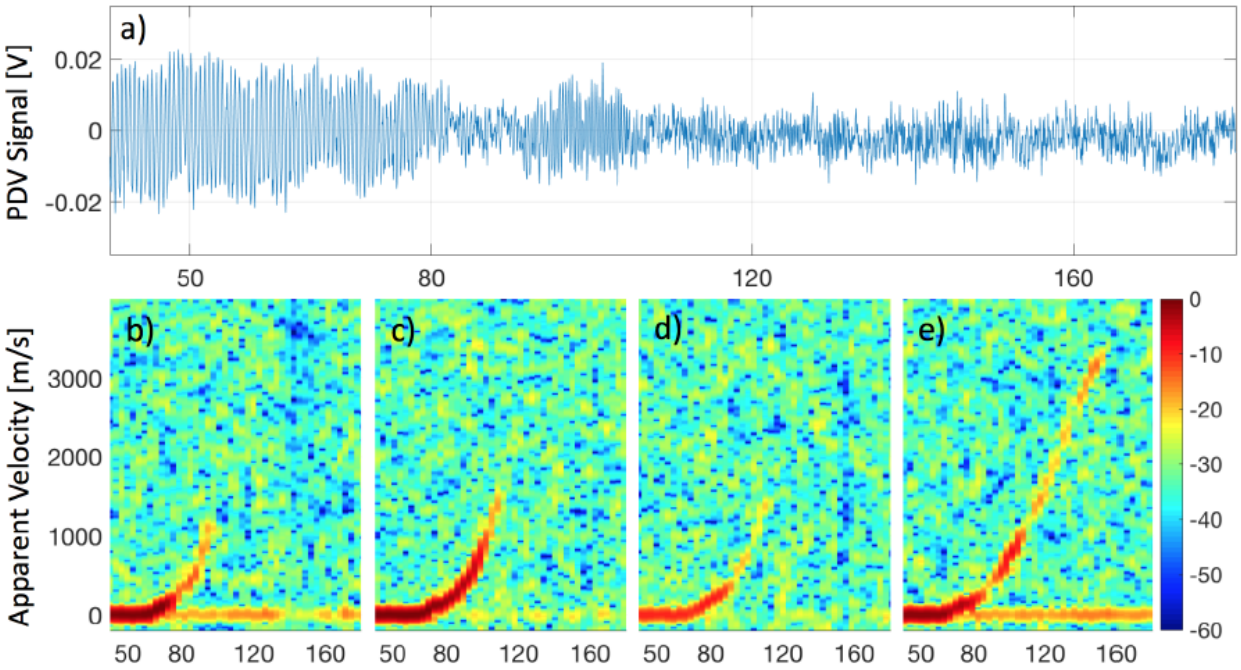

Figure 2 (color). Representative unprocessed PDV data (a) and STFT spectrograms (b-e) corresponding to 800 − µm aluminum rods during the Mykonos current pulse. Spectrograms (b-e) correspond to rods with Parylene-N thicknesses 0, 5, 17, 41 µm respectively. The raw data in (a) generated the spectrogram (e). The colorbar applies to all spectrograms and denotes PSD in dB relative to the maximum PSD for each spectrogram. All x-axes denote time (in ns) and range from 40-180 ns. The y-axis in (b) applies also to spectrograms in (c-e). Time axes in all figures are shifted so that 500 kA occurs at 100 ns. Histograms of spectrograms (e.g., b-e) are approximately normal, reflecting a Gaussian background noise distribution.

By identifying the appropriate PSD in each time column, and storing the corresponding apparent velocity, spectrograms can be dimensionally reduced into $v^*(t)$ traces representing surface velocities (Fig. 3-4). More precisely, the apparent velocity which appears to contain the relevant signal is selected by-eye, then the local maximum-power apparent velocity within 20 frequency bins (151 m/s) is calculated. This selection process is performed to cleanly distinguish between signal indicating melt (non-zero velocity, $>$ 2 GHz) and signal from light which reflected off the vacuum chamber window before reaching the target (zero velocity, 2 GHz). For example, in Fig. 2e around 125 ns, the PSD maxima for a column *is* the window reflection at zero velocity, and not the relevant signal. This process notwithstanding, data at zero velocity after liftoff and before $v^*(t) > 151$ m/s in Fig. 3-4 (65 − 85 ns) are likely residual artifacts.

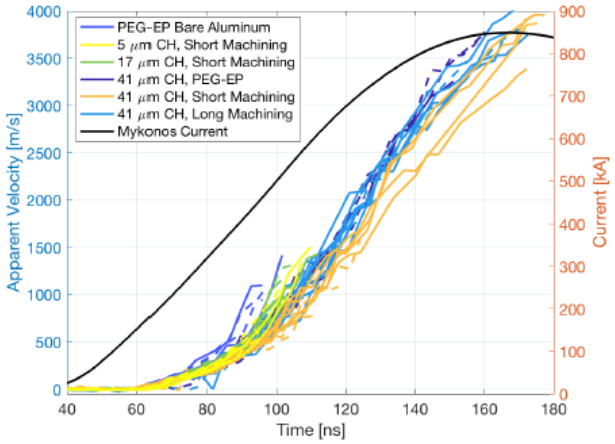

Figure 3 (color). Apparent aluminum velocity, $v^*(t)$, color-coded by coating thickness and surface treatment. Solid lines originate from Channel 1, and dashed from Channel 2. A representative Mykonos current waveform is also plotted. All data derived from spectrograms draws from at most two channels on each of 34 shots, downselected such that only PSD values 1σ ($6.9 \pm 0.3\ dB$) out of the spectrogram histogram (i.e., the noise distribution) are plotted[33].

PDV indicates the aluminum-6061 surface explodes at 62.5 ± 1.5 ns, then expands with constant acceleration until 80.4 ± 3.5 ns, when it begins non-linearly expanding. A piecewise polynomial model (linear-quadratic, or LQ) with a linear term from a specified start time, γ to the non-linear transition τ ($c + dt$), and then a quadratic term until 700 kA ($e + ft + gt^2$) was fit to scatterplot $v^*(t)$ data for each class of rod. The intercept with zero velocity of the linear fit was 62.5 ± 1.5 ns (see Table 1). The surface magnetic field was 85 ± 13 T at melt, where the uncertainty is due to variability between the four $\dot{B}$ probes used to measure the total Mykonos current on each shot, and liftoff timing uncertainty. The linear-to-non-linear transition 80.4 ± 3.5 ns and best start time γ were determined by maximizing the adjusted-r-squared $\left(R^2_{adj}\right)$ of the LQ fit for each rod class as a function of τ and γ, for all τ between 75-90 ns and all γ between 60-65 ns. Using the preshot radius and this time, the surface magnetic field at τ is 164 ± 20 T. For uncoated loads, PDV signals have all fallen to worse than 1 σ by the time the surface magnetic field is 243 T, approximately consistent with the threshold above which aluminum surfaces form plasma, 220 T[1].

	c [m/s] ± 95% Conf.	d [(m/s)/ns] ± 95% Conf.	e [m/s] ± 95% Conf.	f [(m/s)/ns] ± 95% Conf.	g [(m/s)/ns^2] ± 95% Conf.	τ [ns]	Melt [ns]
Bare Aluminum PEG-EP	$-891 \pm N/A$	14.7 ± 0.1	$4319 \pm N/A$	-127.9 ± 6.6	0.97 ± 0.08	77.4	60.7
5 μm CH, Short Machining	$-802 \pm N/A$	12.7 ± 0.1	$5968 \pm N/A$	-156.6 ± 2.5	1.06 ± 0.03	78.9	63.2
17 μm CH, Short Machining	$-1074 \pm N/A$	16.5 ± 1.1	$-1463 \pm N/A$	$0 \pm N/A$	0.24 ± 0.02	86.8	64.9
41 μm CH, Long Machining	$-618 \pm N/A$	9.9 ± 0.1	$2215 \pm N/A$	-67.4 ± 1	0.52 ± 0.01	78.2	62.5
41 μm CH, Short Machining	$-629 \pm N/A$	10.2 ± 0.1	$1630 \pm N/A$	-50.5 ± 2	0.41 ± 0.01	78.9	61.7
41 μm CH, PEG-EP	$-667 \pm N/A$	10.8 ± 0.1	$583 \pm N/A$	-34.6 ± 1	0.37 ± 0.01	82.1	61.8

Table 1. LQ regression coefficients describing the velocity history of the aluminum rod surfaces, depending on surface finish and coating thickness. LQ fits can be seen in $v^*(t)$ plots (see Fig. 4a). Independent linear and quadratic fits will not, in general, agree at τ without imposing constraints on the fitting parameters. In these cases, confidence intervals cannot be found because fit parameters are bounded at the constraint, and thus are specified as N/A. These bounds are found by iteratively and incrementally

constraining c, e from the appropriate direction until the two polynomials agree to within 1 m/s at τ, while f was constrained to be ≤ 0 otherwise $g < 0$ for the $17-$ µm-coating case; the statistical metrics of fit quality are calculated after this procedure.

For every class of rod, the LQ fit was significantly better than a single quadratic fit (determined by R^2_{adj}) with the same melt time, which badly models the linear liftoff (apparent in Fig. 4a). In addition, while data in Fig. 2e appears linear from $85-160$ ns, $\dot{I}$ becomes sub-linear at ~ 125 ns (700 kA), which determined where the LQ fitting region terminates. That v^* slows around peak current suggests that thermal pressure ($-\vec{\nabla}P$) dominates magnetic pressure ($\vec{j}\times\vec{B}$). PDV data on metal for which v^* is expected to be zero, that is, when $\vec{j}\times\vec{B} = -\vec{\nabla}P$ may constrain the local current density. Fit coefficients to v^* for different rod types are presented for future MHD modelling comparisons (see Table 1).

A shock in the dielectric is absent in the PDV data, although there is some uncertainty in the literature as to the true speed of sound, v_{ss}, for Parylene-N. For example, the speed of sound in cold, uncompressed Parylene-N inferred from $v_{ss} = \sqrt{E/\rho}$ (where E is the experimentally measured Parylene-N elastic modulus[34, 35, 36]) is $v_{ss} = 1.5$ µm/ns, while Ref. 37 calculated $v_{ss} = 1.9$ µm/ns as calculated from the QEOS physics model[38, 39]. In any case, $v^*(t)$ data does not show discontinuous transitions indicative of a shock. However, since the metal speed eventually exceeds the fastest literature v_{ss} (1.9 µm/ns), and since this occurs while the metal is constantly accelerating, a shock in the dielectric is not fast enough to detach from the metal (i.e., it is expected to be pinned to the metal surface).

Modelling suggests the nonlinear transition time τ corresponds to metal entering the vapor dome. This transition time does not obviously covary with the coating thickness (See Table 1). Additionally, metal behavior can only vary under different coating thicknesses when rarefaction waves return from the free surface to the metal-dielectric boundary. However, τ is only 20 ns after surface motion begins, an insufficient amount time for mechanical waves travelling at v_{ss} to reflect off the free dielectric surface and return to the dielectric-metal interface (at least for the $41-$ µm-coated rods). Preliminary modelling with the ALEGRA MHD[40] code suggest τ corresponds to metal entering the vapor dome, which permits identification of the linear portion of the curve as denoting liquid metal, and the quadratic part as a liquid-vapor mixture. Since it is in low-density aluminum vapor that plasma is expected to form[41], and no evidence suggests plasma does form for $41-$ µm-coated rods, the density in that case is likely sufficiently tamped to keep the metal from exiting the vapor dome. Although metal follows the binodal through phase space in thin-wire explosions[42], an equivalent statement in the thick-rod case is inconsistent with both the MHD-supported inference that τ corresponds to metal entering the vapor dome, and that plasma forms[1] in metal vapor[41] (indicating the existence of single-phase metal).

The constant acceleration after melt depends on the presence of a dielectric coating (Table 1, or Fig. 4a), albeit inconsistently. Data indicate uncoated and thinly-coated rods experience a larger initial acceleration than the $41-$ µm-coated rods, consistent with inertial tamping (Table 1). The surface finish does not have an appreciable effect on the surface velocity (Fig. 3), although the PEG-EP rods are 42 µm smaller in diameter due to electropolishing, carry the corresponding ratio more surface $\vec{j}$, and therefore are expected to expand marginally faster (as seen in Fig. 3) than other $41-$ µm-coated rods. Additionally, no negative (or compression-related) velocities were observed, as suggested by[43]. Figures 2-4 show the surface acceleration is certainly not zero, as has historically been understood for thin wire explosions[7], and not even constant throughout the current pulse.

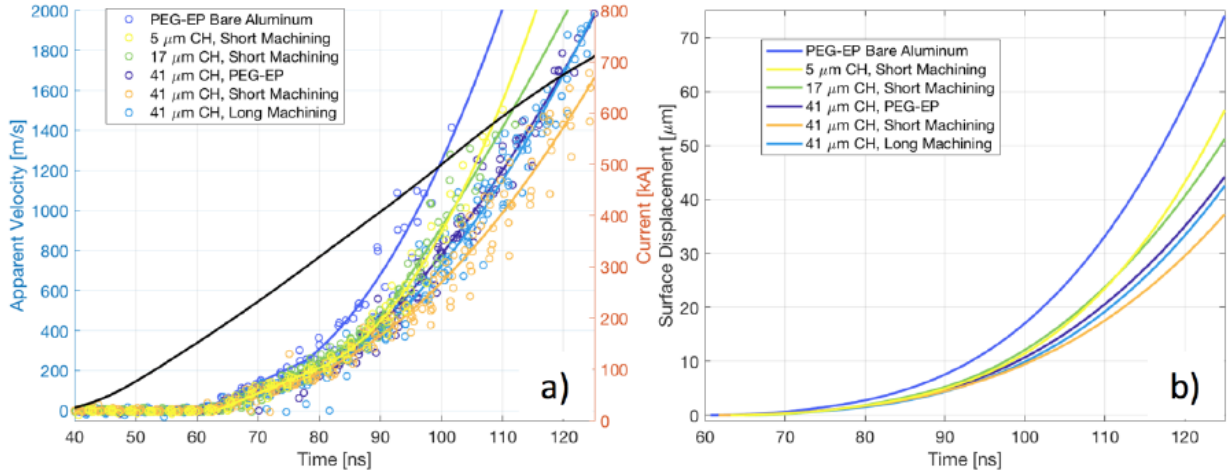

Figure 4 (color). LQ fits to PDV data for rods with different Parylene-N thicknesses and surface treatments (a), and trapezoidal integrals of LQ fits, representing the total surface displacement (b). All data in (a) are again at least 1σ out of the background spectrogram noise. The slope transition is visible in (a) at ~ 81 ns. Some PDV signals disappear at 100-110 ns, but quadratic fits (and their integrals) extend past these for visual comparison.

Reflected light persists through peak current for loads which do not form plasma. Due to the laser coherence, light reflected from the non-uniform metal surface forms a speckle pattern on the return fiber aperture. This diffraction pattern changes dynamically as the surface evolves, and therefore amplitude trends in the data cannot be unequivocally attributed to material properties of the reflective matter. However, the average rate of signal loss across all rods is 0.45 ± 0.1 dB/ns for the $70 - 110$ ns period. This rate doesn't vary with coating thickness. The loss of PDV signal for thinly-coated rods (5 μm and 17 μm Parylene-N) is approximately at the same time as filamentation in ICCD imaging (Fig. 5b, c, indicative of plasma) and with the sharp rise in visible emissions (seen in photodiode data, Fig. 6) that is also indicative of plasma[1]. However, the PDV signal doesn't entirely vanish for 41 μm-coated rods. Rather, it intermittently persists until (at the latest) 170 ns, indicating the hot, expanded aluminum reflects PDV light throughout the current pulse, and therefore the matter is not a blackbody at 1550 nm. This inference compromises blackbody assumptions often used in radiometry calculations, and indicates interferometry- or reflectometry-based diagnostics are suitable for measuring properties of the WDM underneath transparent insulating coatings.

PDV light is expected to propagate through any underdense aluminum, and continue propagating up a density gradient until it eventually reflects off aluminum at the critical density. The maximum critical density for extraordinary light is

$$n_e = \omega^2 \frac{\varepsilon_0 m_e}{e^2}\left(1 + \frac{eB_0}{\omega m_e}\right), \qquad (5)$$

where B_0 is the magnetic field, ω the PDV laser frequency, e an electron charge, m_e an electron mass, and ε_0 the vacuum permittivity. For $B_0 = 100\ T$, $n_e = 4.7{\times}10^{20}$ e$^-$/cm^3, although $n_e(B_0 = 0)$ is only a couple percent different. Assuming 3 valence electrons per aluminum atom, Eq. 5 indicates the critical aluminum atom density for $\lambda = 1550$ nm light is $\rho_{cr} \sim \rho_{solid}/380$. Differences in ρ_{cr} with the GHz-scale shifts are negligible. Since all Doppler shifts (weighted by the apparent area fraction of matter, further scaled by reflectivity of that matter) are reported simultaneously, that the FWHM of peaks in the PSD after explosion (e.g.,

Fig. 2b-e) are approximately as large as those before explosion suggests a narrow distribution in surface velocities. In fact, since PDV is capable of diagnosing λ-scale diffuse metallic ejecta from the free-surface of a shock-driven metal[44, 45], and the corresponding features in spectrograms of ohmically-exploded rods are absent, diffuse surface ejecta are not present (at least for matter with $\rho < \rho_{cr}$). This supports the idea that the metal expands with a narrow distribution of velocities throughout the current pulse. In addition, if underdense metallic vapor is partially reflecting PDV light, the velocity of that underdense vapor would appear in the data together with that corresponding to denser material. The lack of two different velocities (or more generally, a distribution of velocities) suggests either a steep density gradient, or transparency of underdense aluminum to PDV light. In principle, the density gradient of a z-pinch driven metal explosion could be measured with polychromatic PDV. While quantitative comparisons are beyond the scope of this paper, and although Parylene-N is not expected to carry current, these results are qualitatively distinct from extended MHD predictions of coated current-carrying rods[46].

Additional preliminary MHD modelling using the Arbitrary Lagrangian-Eulerian FLAG code[47] accurately predicts the metal melt time, and indicates that the Parylene-N outer surface decompresses (due to the release of waves generated by the expanding aluminum), although it overpredicts (by up to a factor of ten) the expansion velocity, especially after matter enters the vapor dome. The ALEGRA code also overpredicts the expansion velocity once material becomes vapor, but further predicts a dependence of expansion velocity on cell size and EOS table. Collectively, these difficulties signal PDV data may pose an enduring challenge to well-benchmarked numerical modelling of surface metal velocities during electrical explosions, although it is expected that the coated-rod case will be easier to model than the bare metal case.

ICCD imaging indicates that plasma forms for bare aluminum and thinly coated rods, but does not form for 41-um coated rods. Intensified images were taken with Andor DH334T-18U-73 and DH340T-18F-E3 cameras. 4 μm resolution was achieved at a magnification of 12.4 using an annular-aperture Questar QM100 long distance microscope. The depth of focus (DOF) for ICCD imaging was approximately 125 μm, as measured by moving an imaging reticle through best focus with a $10-$ μm-sensitive translation stage. This shallow DOF explains the twin-focused bands in Fig. 5a, and the ring structures in Fig. 5f, which are imaging artifacts of far-field-defocused point-like emission in an annular-aperture optical system[48]. Plasma formation occurs for bare aluminum when the surface has expanded by ~ 35 μm, while for thinly-coated rods it is slightly more, ~ 40 μm (from Fig. 4b). No images of $41-$ μm-coated rods showed signs of filamentation (that is, plasma formation). ICCD imaging also shows electrothermal instability strata[22] for all coated-aluminum rods. Absolute calibration of ICCD images is beyond the scope of this article, but recent literature reporting comparable results indicates images represent metal in the range of $0.4-0.8$ eV[22]. The bright spots in Fig. 5 (b, c) correspond to the initiation of plasma filamentation[49].

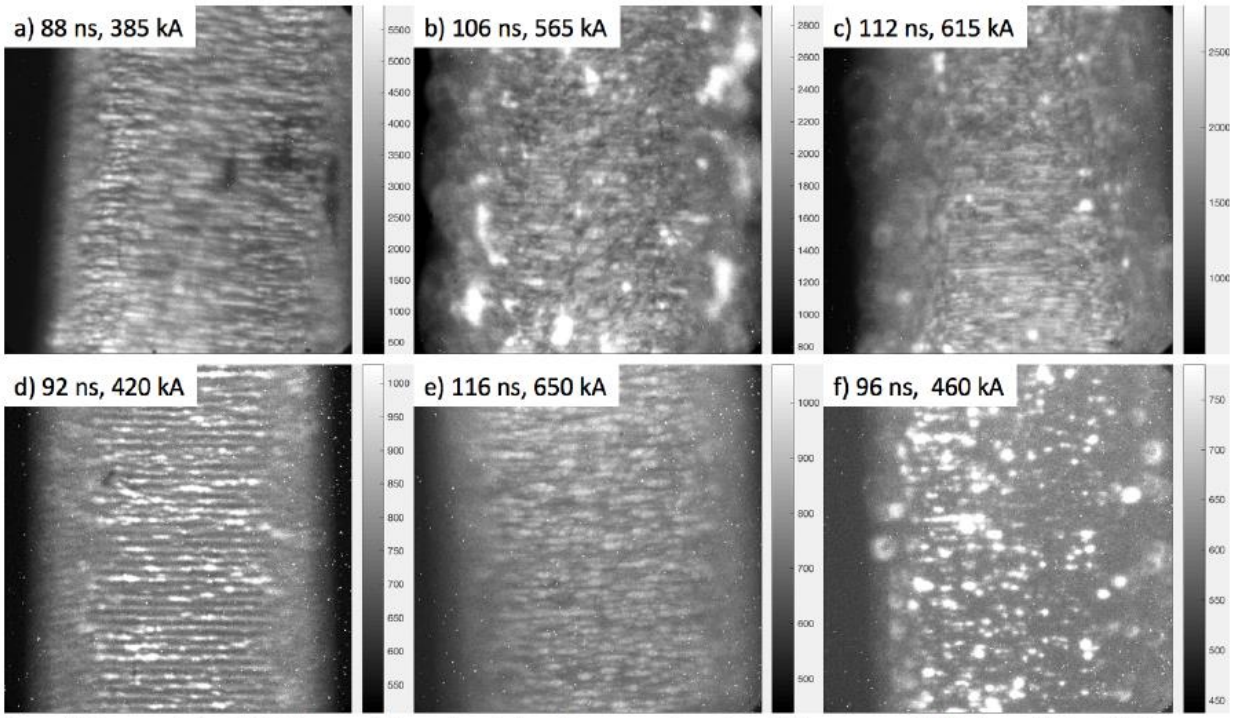

Figure 5. Representative ICCD frames of thermal emissions from current-carrying (a) 5 − μm-coated short machining, (b) 5 − μm-coated short machining (c) 17 − μm-coated short machining, (d) 41 − μm-coated long machining, (e) 41 − μm-coated short machining, and (f) uncoated rods. Frames are all 2 ns long and each image is 1053 μm on an edge – alternatively, the scalebar in d) is 100 μm × 300 μm. Non-linear gain settings were (2000, 1000, 1000, 1000, 50, 1000) for (a-f) respectively, and greyscale values denote counts.

It is not known whether the plasma forms beneath, above, or through the dielectric, but four potential plasma formation mechanisms are identified: 1) when the free-surface releases, the Parylene-N must admit circumferential tensile forces that may be large enough to tear the dielectric, creating crevasses or point-like defects that facilitate plasma formation; 2) the local explosion around inclusions[22, 49] may push through thin dielectric coatings and form plasma as bare metal does; 3) the ultraviolet flux (or shock) from the aluminum may weaken the otherwise enormous Parylene-N dielectric strength[36]; and 4) since any flow electrons from the transmission line would form plasma irrespective of coating thickness, they could not alone be responsible for the plasma formed on thinly-coated metal. However, any number of the above mechanisms could simultaneously contribute to plasma formation. Finally, for thinly-coated rods, ICCD imaging indicates plasma forms simultaneously at spatially separated locations from 10 − 50 μm spots. The number density of these plasma-forming-locations (Fig. 5b, c) is smaller than for bare metal (Fig. 5f), which at minimum suggests not every inclusion would contribute to the mechanism 2), above.

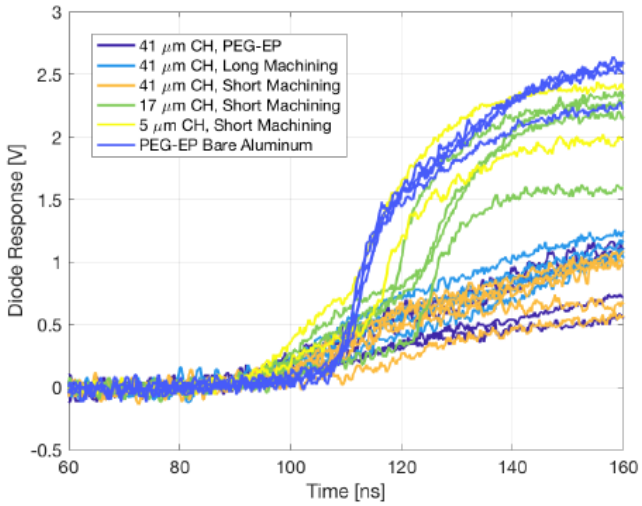

Figure 6 (color). Time-resolved emission history for each rod type, determined by a fast photodiode. The photodiode relies on an achromatic imaging system for the visible light spectrum, and has spectral responsivity typical for a photoconductive silicon diode (400 – 1100 nm).

Time-resolved photodiode data indicate that thinly-coated and bare aluminum form plasma, while 41 – μm-coated aluminum does not. The photodiode integrates emissions over 60 μm × 290 μm of the rod surface. For uncoated rods, plasma formation occurs at the inflection in photodiode signals (Fig. 6, at 110 ns)[1]. Plasma formation is delayed for coated loads, and presents with greater variability, hinting at a stochastic mechanism for plasma formation on thinly-coated rod experiments (or non-uniform coating thicknesses). The inflection does not appear for 41 – μm-coated rods, indicating they do not form plasma. Before plasma formation, during the ramp in visible light signals 90 – 105 ns, uncoated rods typically emit less light than coated rods, consistent with the supplemental *PdV* cooling associated with untamped expansion[22]. For rods which form plasma, the inflection in photodiode data (historically used to infer plasma formation) occurs 5 – 10 ns after PDV signals have fallen into the noise. The photodiode integrates over a much larger part of the surface than PDV, potentially attributing this delay to the spatially non-uniform (i.e., temporally extended) plasma formation process seen in typical ICCD images of rod surfaces (Fig. 5b, c, or see Ref. 49). These arguments support the hypothesis that the PDV signal disappears when plasma forms.

In conclusion, PDV was used to measure the surface velocity of aluminum pulsed with intense electrical current. The liquid metal expands with constant acceleration until a transition to a linearly growing acceleration, suggested by MHD modelling to corresponds to a liquid to liquid-vapor transition. Plasma formation was observed for uncoated, 5–μm-coated and 17 – μm-coated but not 41 – μm-coated aluminum, and is correlated with PDV signal cutout. The expansion rate of the metal is not appreciably affected by the aluminum surface finish under the coatings. The data presented in this article may be used to benchmark future MHD simulations, and signals that PDV functions well as a phase-discernment diagnostic.

The authors would like to sincerely thank V. Anaya, E. Baca, W. Cline, K. Cochrane, C. Davidson, M.P. Desjarlais, M. Gilmore, M.W. Hatch, J. Jarrell, D. Lammpa, J. Moore, T. Mulville, S. Patel, A. Porwitzky, G.A. Shipley, B. Stolzfus, D.A. Yager-Elorriaga, K.C. Yates, and D. Young for helpful discussions, technical assistance and/or experimental equipment. This material is based upon work supported by the Department of Energy, National Nuclear Security Administration, under Award Number DE-NA0003870. This research was also supported by

Sandia's Laboratory Directed Research and Development Program (Project No. 200269). Sandia National Laboratories is a multi-mission laboratory managed and operated by National Technology and Engineering Solutions of Sandia, LLC., a wholly owned subsidiary of Honeywell International, Inc., for the U.S. Department of Energy's National Nuclear Security Administration under Contract No. DE-NA-0003525.

---

*trevorhutchinson@unr.edu

[1] T. J. Awe, B. S. Bauer, S. Fuelling, and R. E. Siemon, Phys. Rev. Lett. 104, 035001 (2010).
[2] F. Graziani, M. P. Desjarlais, R. Redmer, and S. B. Trickey, eds., Frontiers and Challenges in Warm Dense Matter (Springer, Berlin, 2014).
[3] C.D. Munz, R. Schnieder, and O. Gerlinger. Math. Meth. in Appl. Sci. 17, no. 8 (1994).
[4] E.L. Toro. *Riemann Solvers and Numerical Methods for Fluid Dynamics* (Springer, Berlin, 1997). See section 4.6.
[5] T. J. Awe, Ph.D. dissertation. University of Nevada, Reno 2009; see Fig VI.3, VI.9.
[6] R.E. Siemon, B.S. Bauer, T.J. Awe, M.A. Angelova, S. Fuelling, T. Goodrich, I.R. Lindemuth, V. Makhin, W.L. Atchison, R.J. Faehl, R.E. Reinovsky, P.J. Turchi, J.H. Degnan, E.L Ruden, M.H. Frese, S.F. Garanin, and V.N. Mokhov. J. Fusion Energy **27**: 235-240 (2008).
[7] G.S. Sarkisov, K.W. Struve, and D.H. McDaniel. Physics of Plasmas **11**, 4573 (2004).
[8] M.R. Douglas and B.S. Bauer. Sandia National Laboratory SAND Report 3361 (2001).
[9] W. Zou, J. Dan, G. Wang, S. Duan, B. Wei, H. Zhang, X. Huang, Z. Zhang, F. Guo, B. Gong, L. Chen, M. Wang, S. Feng, W. Xie, and J. Deng. Physics of Plasmas **25** 022120 (2018).
[10] K. J. Peterson, T. J. Awe, E. P. Yu, D. B. Sinars, E. S. Field, M. E. Cuneo, M. C. Hermann, M. Savage, D. Schroen, K. Tomlinson et al., Phys. Rev. Lett. 112, 135002 (2014).
[11] T. J. Awe, K. J. Peterson, E. P. Yu, R. D. McBride, D. B. Sinars. M. R. Gomez, C. A. Jennings, M. R. Martin, S. E. Rosenthal, D. G. Schroen et al., Phys. Rev. Lett. 116, 065001 (2016).
[12] O.T. Strand, L.V. Berzins, D. R. Goosman, W.W. Kuhlow, P.D. Sargis, and T.L. Whitworth. Proc. of SPIE 5580 (2004).
[13] O.T. Strand, D.R. Goosman, C. Martinez, and T.L. Whitworth. Rev. Sci. Ins. **77** 083108 (2006).
[14] D.H. Dolan Rev. Sci. Ins. **81** 053905 (2010).
[15] A. Porwitzky and J. Brown. Phys. Plasmas. **25** 063102 (2018).
[16] M.I. Kaufman, R.M. Malone, B.C. Frogget, D.L. Esquibel, V.T. Romero, G.A. Lare, B. Briggs, A.J. Iverson, D.K. Frayer, D. DeVore, B.Cata, D.B. Holtkamp, M.D. Wilke, N.S.P. King, M.R. Furlanetto, M. Briggs, and M.D. Furnish. Proc. of SPIE - The Int. Soc. for Opt. Eng. **6676** 667607 (2006).
[17] D.H. Dolan, R.W. Lemke, R.D. McBride, M.R. Martin, E. Harding, D.G. Dalton, B.E. Blue, and S.S. Walker. Rev. Sci. Ins. **84** 055102 (2013).
[18] M.G. Mazarakis, W.E. Fowler, K.L. LeChien, F.W. Long, M.K. Matzen, D.H. McDaniel, R.G. McKee, C.L Olson, J.L. Porter, S.T. Rogowski, K.W. Struve, W.A. Stygar, J.R. Woodworth, A.A. Kim, V.A. Sinebryukhov, R.M. Gilgenbach, M.R. Gomez, D.M French, Y.Y. Lau, J.C. Zier, D.M VanDevalde, R.A. Sharpe, and K. Ward. IEEE Trans. Plas. Sci. **38**, 4 (2010)
[19] O. Schnitzer, Phys. Plasmas **21**, 082306 (2015).
[20] V. I. Oreshkin, S. A. Chaikovsky, I. M. Datsko, N. A. Labetskaya, G. A. Mesyats, E. V. Oreshkin, N. A. Ratakhin, and D. V. Rybka, Phys. Plasmas 23, 122107 (2016).

[21] K.C. Yates, B.S. Bauer, S. Fuelling, T.J. Awe, T.M. Hutchinson, V. V. Ivanov, J. Mei, and R. S. Bauer. Physics of Plasmas **26**, 042708 (2019).
[22] T.M. Hutchinson, T.J. Awe, B.S. Bauer, K.C. Yates, E.P. Yu, W.G. Yelton, and S. Fuelling, Phys. Rev. E **97**, 053208 (2018).
[23] M. Evans, M.B. Adams, P.C. Campbell, N.M. Jordan, S.M. Miller, N.B. Ramey, R.V. Shapovalov, J. Young, I. West-Abdallah, J.M. Woolstrum, R.D. McBride, and P.A. Gourdain. Phys. Plasmas. **26** 070704 (2019).
[24] Y. S. Jeong, B. Ratier, A. Moliton, and L. Guyard, Synth. Metals **127**, 189 (2002).
[25] Gorham, W. F. J. Polym. Sci., Part A-1: Polym. Chem. 1966, 4, 3027−3039.
[26] ZEMAX Optical Design Program, ZEMAX Development Corp., 4901 Morena Blvd., Suite 207, San Diego, CA 92117-7320.
[27] B.J. Jensen, D.B. Holtkamp, P.A. Rigg, and D.H. Dolan. J. Appl. Phys. **101**, 013523 (2007)
[28] D.H. Dolan, Tech. Rep. SAND2006–1950, Sandia National Laboratories, 2006
[29] Y. Lie, and P.H. Daum. Journal of Aerosol Sci. **39**, Iss. 11, pg. 974-986 (2008).
[30] D.H. Dolan. Rev. Sci. Ins. **81**, 053905 (2010).
[31] F.J. Harris. Proc. of IEEE **66**, 1 (1978). The choice of no windowing function imports strong 'ringing' into spectrograms associated with the boxcar's comparatively large sidelobes – this complicates analysis and so a Hamming window was chosen.
[32] Typical absolute signal returns were negative $30 - 40\ dBm$, or $0.1 - 1\ \mu W$. Signal returns were profoundly sensitive to optical or target misalignment, as were the presence (or absence) of window reflections.
[33] This may appear an unreasonably low SNR, however, latitude is merited for correlated spectrogram data. For example, consider a series of PSD maxima each only 1σ out of the noise that forms a smooth $v^*(t)$ curve, the statistical likelihood of the curve is significantly better than the individual 1σ for each column. This exact situation is present for spectrograms of PDV data, and the authors justify the ostensibly low SNR in this fashion.
[34] N. Jackson, F. Stam, J. O'Brien, L. Kailas, A. Mathewson, C. O'Murchu. Thin Solid Films **603** p371-376 (2016).
[35] B.J. Kim and E. Meng. Polymers for Adv. Tech. **2016**, 27 564–576 (2015).
[36] J. B. Fortin and T. Lu, Chemical Vapor Deposition Polymerization—The Growth and Properties of Parylene Thin Films (Springer Science, New York, 2004). α is derived from the experimentally measured Parylene-N dielectric constant.
[37] D.C. Swift and R.G. Kraus. Phys. Rev. E **77** 066402 (2008).
[38] Personal Communication, David Young from LLNL: done by scaling the Parylene-C data at density 1.28 g/cm^3 to Parylene-N at 1.11 g/cm^3 and fitted with the QEOS physics model.
[39] S.D. Rothman, A.M. Evans, C.J. Horsfield, P. Graham, and B.R. Thomas. Physics of Plasmas **9**, 1721 (2002).
[40] A.C. Robinson and C.J. Garasi. Computational Physics Communcations 164, 408 (2004).
[41] I. R. Lindemuth, R. E. Siemon, B. S. Bauer, M. A. Angelova, and W. L. Atchison, Phys. Rev. Lett. 105, 195004 (2010).
[42] V.I. Oreshkin, A.S. Zhigalin, A.G. Rousskikh, and R.B. Baksht. Phys. Plasmas. **26** 062710 (2019).
[43] S.F. Garanin, G.G. Ivanova, D.V. Karmishin, and V.N. Sofronov. J. of App. Mech. and Tech. Phys., Vol. **46**, No. 2, pp. 153–159 (2005).
[44] J.E. Franzkowiak, G. Prudhomme, P. Mercier, S. Lauriot, E. Dubreuil, and L. Berthe. Rev. Sci. Ins. **89** 033901 (2018).

[45] A. V. Andriyash, M. V. Astashkin, V. K. Baranov, A. G. Golubinskii, D. A. Irinichev, V. Yu. Khatunkin, A. N. Kondratev, S. E. Kuratov, V. A. Mazanov, D. B. Rogozkin, and S. N. Stepushkin. J. App. Phys. **123** 243102 (2018).
[46] P.A. Gourdain, M.B. Adams, M. Evans, H.R. Hasson, R.V Shapovalov, J.R. Young, and I. West-Abdallah. Phys. Plasmas **26** 042706 (2019).
[47] K. Lipnikov, J. Reynolds, and E.Nelson. J. of Comp. Phys. **247** (2013).
[48] D. Lin, N.C. Angarita-Jaimes, S. Chen, A.H. Greenaway, C.E. Towers, and D.P. Towers. Optics Letters, **33** 9 (2005).
[49] T. J. Awe, E. P. Yu, K. C. Yates, W. G. Yelton, B. S. Bauer, T. M. Hutchinson, S. Fuelling, and B. B. McKenzie, IEEE Trans. Plasma Sci. 45, 584 (2017).

This paper describes objective technical results and analysis. Any subjective views or opinions that might be expressed in the paper do not necessarily represent the views of the U.S. Department of Energy or the United States Government

APPENDIX B. 3D-MHD SIMULATION PAPER DRAFT

Three-dimensional metal deformation and plasma formation driven by current redistribution around resistive inclusions

E. P. Yu,[1,*] T.J. Awe,[1] B. S. Bauer,[2] K.J. Peterson,[1] T.M. Hutchinson,[2]
K. C. Yates,[3] K. R. Cochrane,[1] M. W. Hatch,[3] and A. Klemmer[2]

[1] *Sandia National Laboratories, Albuquerque, New Mexico 87185*
[2] *University of Nevada, Reno, Reno, Nevada 89506*
[3] *University of New Mexico, Albuquerque, New Mexico 87131*

(Dated: September 10, 2019)

Focusing on current-carrying metals driven to megagauss-level magnetic fields, we study how current density **j** redistributes around a resistive inclusion to initiate a complicated feedback loop: **j** both reacts to and alters the electrical conductivity σ, through Joule heating and hydrodynamic expansion, so that **j** and σ are constantly in flux. Using three dimensional (3D) magnetohydrodynamic simulation, we show how a μm-scale inclusion drives the formation of a 10X larger crater in the metal, as well as an exploding plume embedded with an overheated filament. Due to **j** redistribution in the filament, it achieves plasma-like temperatures significantly earlier than an equivalent 1D simulation, highlighting the 3D nature of plasma formation.

PACS numbers: Valid PACS appear here

Introduction – Understanding how intense electrical current flows through conductors is essential to a wide range of applications, from magneto-inertial fusion [1–5] to protoplanetary disk heating [6]. The richness of the problem is embodied in a feedback loop connecting current density **j** and electrical conductivity σ: regions with enhanced **j** experience larger Joule heating, raising the temperature T, which in turn alters σ (owing to $\sigma(T)$ dependence), thus altering **j**. Hence **j** and σ constantly evolve in response to each other. A one-dimensional (1D) example of this feedback is nonlinear magnetic diffusion [7, 18, 27, 36], where **j** diffuses into a metal at an enhanced rate, due to the Joule heating of the outer edge and the associated drop in σ. However, what patterns emerge when the feedback loop is seeded with a three dimensional (3D) perturbation? In order for the feedback to initiate, the Joule heating must raise the temperature sufficiently to alter σ. As discussed in Refs. [18, 36], such a condition is equivalent to a minimum magnetic field strength, which for most metals is well-satisfied for megagauss-level fields.

Another important consequence of the feedback loop is the potential for a Joule heating-driven instability, often referred to as the electrothermal instability (ETI) [8–14]. Assuming vertical current flow, ETI predicts the formation of horizontal, hot bands (striations) in the metal phase where $\mathrm{d}\sigma/dT < 0$. Once the metal heats into the plasma state, where $\mathrm{d}\sigma/dT > 0$, ETI predicts the most unstable mode reorients to form vertical, overheated filaments. Both of these structures have important practical consequences: horizontal striations can limit the performance of applications involving magnetically-accelerated conductors (such as magneto-inertial fusion, flyer plates used for material properties studies, and magnetic flux compression) by seeding the virulent magneto Rayleigh-Taylor instability [MRT] [9, 19], which can shred apart the conductor in flight. Vertical filaments play a vital role in plasma formation, which is a key concern in the design of pulsed-power drivers: plasma formed from the conductor surface of a magnetically-insulated transmission line can cause current loss if it bridges the gap [16, 17]. ETI theory predicts the orientation of the most unstable mode (i.e. horizontal or vertical), but does not address what seeds striation formation, nor how horizontal striations transform into vertical filaments once the metal converts to plasma.

Researchers originally conjectured that surface roughness might seed ETI, but magnetic implosions of horizontally vs vertically-grooved rods showed little qualitative difference in radiography [24]. Recently, Awe et al. [29] observed ETI by measuring visible emission from Al rods, pulsed with 1 MA current. Pre-shot characterization of the rods revealed an abundance of μm-scale resistive inclusions (RI), consisting mostly of Si and Mg. Emission images showed the development of horizontal, bright bands, roughly correlated with the number of RI, followed by the appearance of vertical filaments, thus suggesting the possibility that RI might seed ETI.

In this work, we use 3D magnetohydrodynamic (MHD) simulation to study how **j** redistribution around a RI, embedded in the surface of a metal rod, can seed both the striation and filament form of ETI. The feedback loop entangling **j** and σ allows the RI to transform into a horizontally-oriented striation. Later, the overheated striation explodes, generating an expanding plume and leaving behind a crater 10X the original RI size, thus providing a seed for later MRT development. The plume develops asymmetrically due to **j** redistribution, expanding axially but *focusing* horizontally, thus paving the way for vertical plasma filament formation.

Current flow around a resistive inclusion (RI) – Consider the idealized problem of a non-conducting sphere

*Electronic address: epyu@sandia.gov

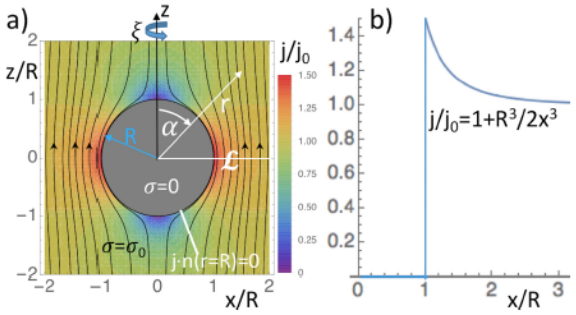

FIG. 1: a) Current flow around a non-conducting sphere. Current density $\mathbf{j}$ flows vertically, as illustrated by the black streamlines, amplifying at the equator, as indicated by the coloring. The visualization plane cuts through the center of the sphere; the full 3D solution is obtained by rotating the 2D pattern about the z axis (i.e. in the ξ direction) b) $j(x)$ taken along the line $\mathcal{L}$, which lies in the equatorial plane.

of radius R, embedded in material of constant conductivity σ_0 (see Fig. 1a). In steady state, charge conservation demands $\nabla \cdot \mathbf{j} = 0$, which when combined with Ohm's law $\mathbf{j} = \sigma_0 \mathbf{E} = -\sigma_0 \nabla \phi$, yields Laplace's equation $\nabla^2 \phi = 0$. Hence, we seek a harmonic function ϕ subject to the boundary conditions $\mathbf{j} \cdot \hat{r}(r = R) = 0$ and $\mathbf{j}(r \to \infty) = j_0 \hat{z}$.

As has been known for some time [25], the above problem is exactly the same as its hydrodynamic counterpart: steady-state, incompressible, inviscid flow (with velocity $\mathbf{v}$) around a sphere. Hence, we can obtain the solution to the electrical problem directly from the well-known hydrodynamic solution (e.g. [34]) simply by substituting $\mathbf{v} \to \mathbf{j}$, to obtain $j_{sphere,r} = j_0 \cos\alpha(1 - \frac{R^3}{r^3}), j_{sphere,\alpha} = -j_0 \sin\alpha(1 + \frac{R^3}{2r^3})$, which reaches its maximum value at the surface of the sphere, along the equator: $j_{sphere}(r = R, \alpha = \pi/2) = \frac{3}{2} j_0$. Note that the maximum $\mathbf{j}$ amplification factor $\frac{3}{2}$ is *independent* of R, justifying that even small μm-scale RI can drive significant perturbation in $\mathbf{j}$. The size of the RI only determines how rapidly j approaches its asymptotic value, as illustrated in Fig. 1b. As will be described in Ref. [23], the hydrodynamic analogy applies not only to resistive objects embedded in the metal, but also deformations of the metal surface, an observation that will prove useful later.

3D MHD Simulation – The $\mathbf{j}_{sphere}$ solution provides the initial $\mathbf{j}$ redistribution around the RI, which then initiates the feedback loop described in the introduction. To study this feedback loop, we use the 3D MHD code Alegra [31]. Specifically, we attempt to qualitatively reproduce features of the experiment described in Ref. [29], which applied a 1 MA pulse (see Fig. 2a) to Al rods of radius $r_0 = 0.5$ mm. We use a SESAME equation of state (EOS) [15], including material strength, to model the Al rod. Electrical and thermal conductivities are provided by the Lee-More-Desjarlais model [32]. The simulation is single temperature and does not account for radiative losses. To keep the (Eulerian) computational domain tractable, we only model a small section of the rod, using the wedge geometry shown in Fig. 2b, with periodic boundary conditions in both the axial and azimuthal directions. As shown in Fig. 2c, on the outer face of the rod, we embed a hemispherical $R = 3\mu$m RI. For simplicity, we model the RI as Al, with reduced electrical ($\sigma/10$) and thermal conductivity ($\kappa/10$). Due to the small RI size, we use fine resolution (0.15 μm) in its vicinity.

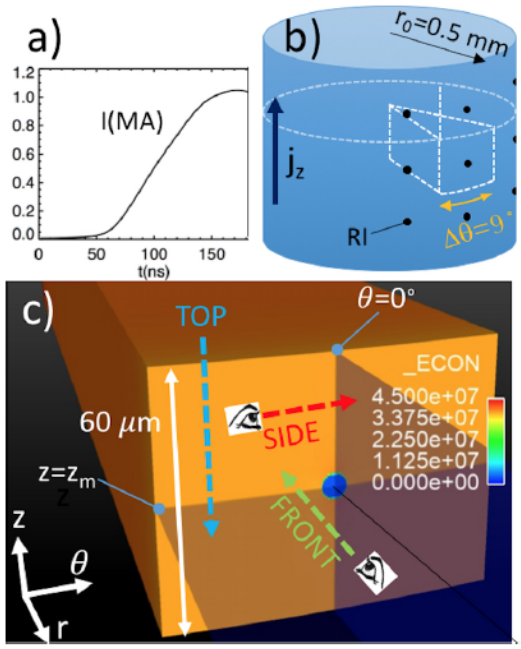

FIG. 2: Computational setup. a) current drive applied to rod. b) Physical scenario treated in 3D MHD simulation: Al rod, with hemispherical resistive inclusions (RI) embedded in the outer face and spaced evenly (we only show 9 of the RI). c) periodic wedge with a single RI, along with visualization planes (top, side, front). All subsequent top views visualize the axial midplane $z = z_m = 30\mu m$.

Striation development –In Fig. 3a-c, we visualize the outer face of the rod at early time, when the rod is still solid. As described earlier, $\mathbf{j}$ bends around the RI, leading to enhanced j at the sides, as well as higher Joule heating ηj^2 and T. In Fig. 3d we show a top view of the RI. As expected from the $\mathbf{j}_{sphere}$ solution, the region of enhanced ηj^2 wraps around the RI's equator.

Once the rod surface melts, hydrodynamic expansion fundamentally alters $\mathbf{j}$ redistribution there. The hotter region to the sides of the RI (see Fig. 3c) expands, resulting in a radial bulge δr at the axial midplane $z = z_m$, as illustrated in Fig. 4a. To understand the resulting $\mathbf{j}$ redistribution, we again use the analogy between hydrody-

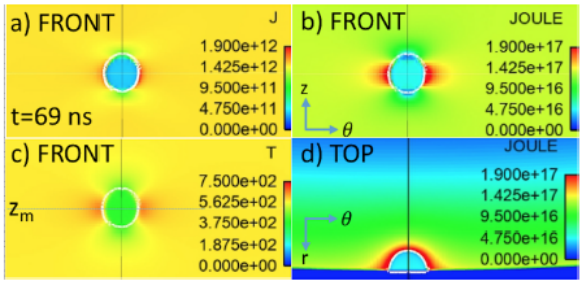

FIG. 3: Flow around a sphere. Outer surface of rod (r=5.006e-4), showing a) j(A/m^2), b) ηj^2(W/m^3), c) $T(K)$. In this figure, and all subsequent figures, the white contours bound the RI. In d), we visualize the RI from the top ($z = z_m$ plane)

namic and electrical current flow, and illustrate in Fig. 4b the solution to flow over a bulge [34]. The increased cross sectional area in the bulge results in reduced j, whereas above and below the bulge, the "bunching" of streamlines, due to j_r, indicates enhanced j. Figure 4c,d confirms this picture: δr drives enhanced $j, \eta j^2$ above/below the bulge, in contrast to the $\mathbf{j}_{sphere}$ solution. The overheated regions eventually transform into a wide, hot strip – the ETI striation – so henceforth we use a subscripted S to denote quantities in the striation. For instance we denote enhanced Joule heating in the striation by $\delta\eta j_S^2 > 0$, as illustrated in Fig. 4d.

Eventually $\delta\eta j_S^2 > 0$ drives $\delta T_S > 0$ (as seen at t=101 in Fig. 5a), so the heated striation begins to expand faster than surrounding metal. However, in contrast to Fig. 4, where expansion resulted in a high-σ bulge pulling $\mathbf{j}$ radially outwards, now the striation is in a region of (ρ, T) space where expansion and heating result in significant reduction in σ (i.e. $\delta\sigma_S < 0$, see Fig. 5b), and consequently $\delta j_S < 0$ (Fig. 5c). As seen in the side view in a plane cutting through the striation (Fig. 5e-g), while the striation bulges outward, σ_S is too low to pull $\mathbf{j}$ outward; rather $\mathbf{j}$ deflects *inward* around the low-σ striation, as sketched by the $\mathbf{j}$ streamline in Fig. 5e.

Qualitatively the flow pattern has evolved yet again, from flow over a bulge to flow over a mound (i.e. the low σ region). In this case, the hydrodynamic solution [34] predicts j focuses at the tip of the mound (Fig. 5h), in agreement with simulation (see arrow in Fig. 5f). The resulting peak in ηj^2 converts high-σ, dense metal behind the mound into hotter, expanded, lower-σ metal, thus effectively deepening the low-σ mound. Recalling that the mound corresponds to the heated, expanded striation, the above process describes how $\mathbf{j}$ redistribution allows the striation to propagate inward, increasing its radial amplitude. Although the striation now corresponds to a region of reduced σ (Fig. 5b) and j (Fig. 5c), it still experiences enhanced ηj^2 (Fig. 5d); the enhancement due to $\delta\eta_S > 0$ overcomes the reduction due to $\delta j_S < 0$. Hence the striation continues to overheat.

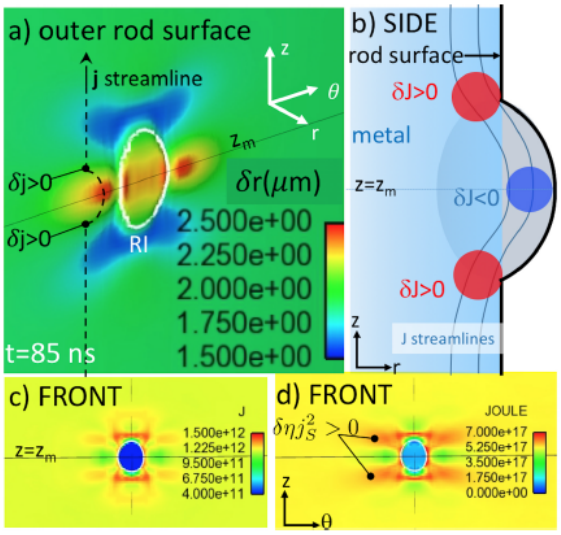

FIG. 4: Flow over a bulge. a) Front face of rod at t = 85 ns, visualized using a ρ =1700 kg/m^3 isosurface, and colored with $\delta r = r - r_0$. The viewing angle is similar to Fig. 2c. b) Cartoon solution for bulge flow: $\mathbf{j}$ bunches at the bulge base resulting in $\delta j > 0$ there. c)-d) j and ηj^2 at outer rod surface r =5.015e-4 m, illustrating transition from $\mathbf{j}_{sphere}$ to bulge flow.

By t=115 ns, the Joule heating pattern seen in Fig. 5d has driven a $\sim$ 1 eV, 40 μm-wide strip, observable in simulated visible emission (Fig. 5i, computed using SPECT3D [35]) and in qualitative agreement with experiment (see Fig. 3 of Ref. [29]). Through the interplay between $\mathbf{j}$ and σ, mediated by Joule heating and hydrodynamic expansion, the hemispherical RI has transformed into the ETI striation. By this time, σ in the striation has dropped sufficiently that $\mathbf{j}$ is forced around its edges, as sketched in Fig. 5j. Hence, the striation no longer experiences enhanced ηj^2; the reduction due to $\delta j_S < 0$ overcomes the increase due to $\delta\eta_S > 0$. However, just as in $\mathbf{j}_{sphere}$ (Fig. 3a), the "bunching" of j at the edges results in $\delta j_{edge} > 0$, as well as $\delta\eta j_{edge}^2 > 0$ (Fig. 5j). In this way, $\mathbf{j}$ redistribution continuously widens the hot striation by burning its edges.

Filament formation – The hottest portions of the metal eventually explode, forming a plasma plume. In this stage, where $\frac{d\sigma}{dT} > 0$, we expect the unstable ETI mode to switch from horizontal striations to vertical filaments. Just as in striation formation, $\mathbf{j}$ redistribution plays a key role.

We have focused on the transformation of the RI from a hemisphere into a striation, but in the immediate vicinity of the RI, the original $\mathbf{j}_{sphere}$ solution is still relevant. To see this, consider t=101 ns: while the striation is already visible on the outer surface (Fig. 5), deeper in the metal, visualized using a top view (Fig. 6a,b), we see the continued influence of $\mathbf{j}_{sphere}$. Recall this solution

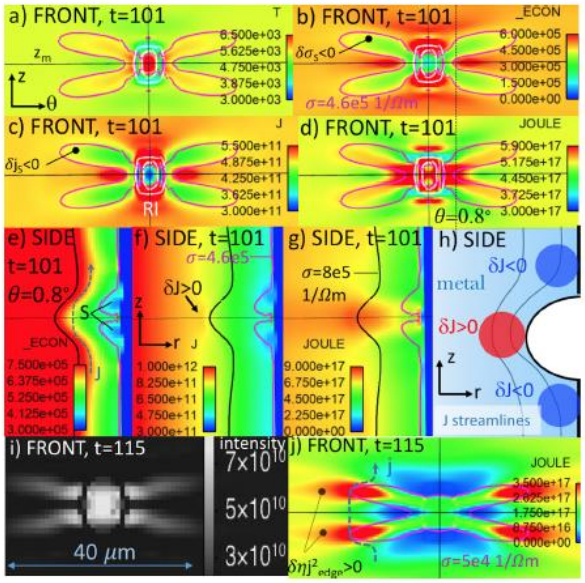

FIG. 5: Striation development. a)-d) Front view of outer face of rod (r =5.085e-4 m) at t=101 ns. The magenta contour roughly bounds the striation. In b), note the location of $\theta = 0.8°$, the viewing plane used in the side views in e)-g). In e), we denote the location of the striation by an "S", and sketch a **j** streamline, deflecting over the low-σ "mound". h) solution for flow over mound. i) simulated visible emission at t=115 ns. Units of intensity are erg/cm^2/s/ster. j) front view of striation at r=5.235e-4 m, including **j** streamline sketch.

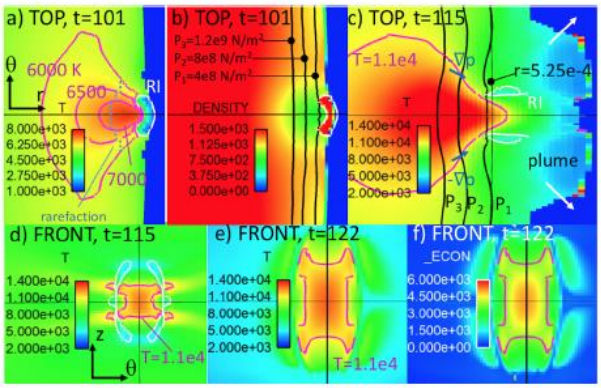

FIG. 6: Filament development a)-b) Top view ($z = z_m$) visualizing the hot spot at t=101 ns. Note the view is rotated relative to Fig. 3f. In a), the dotted curve sketches the depth of the rarefaction wave. c) Top view at t=115 ns. d) front view (r=5.25e-4 m) of the hot spot. In e)-f) we follow the hot spot from d) to r=5.58e-4 m at t=122 ns.

drives enhanced ηj^2 around the equator of the RI, with the most intense heating closest to the RI, as seen at earlier time t=69 ns (Fig. 3b,d). This heating pattern drives highest T closest to the RI, a feature which is seen at later time t=101 ns, in the hot spot behind the RI (Fig. 6a). Note that the hot spot does not correspond to a local increase in pressure; there is a compensating reduction in ρ there (Fig. 6b), resulting in straight pressure contours.

At t=101 ns, the hot spot is about to explode, blowing apart the RI. One might expect the hot spot to expand both axially and azimuthally as it explodes, but in fact it initially *focuses* azimuthally. To understand this, we consider the expansion set up by the profiles in Fig. 6a,b. Because P contours are nearly straight, $-\nabla P$ is radially outward, as is the ensuing expansion. However, the hottest material closest to the RI expands fastest, and the resulting rarefaction penetrates deepest radially there (as sketched by the dotted curve in Fig. 6a), causing the P contours to become concave, as seen at t=115 ns (e.g. see P_2 in Fig. 6c). The pressure gradient $-\nabla P$ now possesses an azimuthally focusing component. Hence, $\mathbf{j}_{sphere}$, which is responsible for T being hottest closest to the RI, is the origin of the focusing effect.

The exploding plume expands azimuthally once it travels far enough away from the rod (see white arrows in Fig. 6c), just as in a "normal" thermal expansion. However, in the vicinity of the hot spot (see magenta contour in Fig. 6c-f), concave P contours drive a focusing flow, similar to the "shaped-charge" effect [37]. Hence, the hot spot expands axially while initially focusing azimuthally. This flow asymmetry transforms the hot spot into a filament, as can be seen by following the hot spot tip from t=115 ns (Fig. 6d) to t=122 ns (Fig. 6e); the spot has elongated axially.

Figure 6f shows the nascent filament has entered the conductivity regime $\frac{d\sigma}{dT} > 0$, and thus satisfies the condition required for the filament form of ETI: $d\sigma > 0 \Rightarrow dj > 0 \Rightarrow d\eta j^2 > 0 \Rightarrow dT > 0$. Just as in striation formation, **j** redistribution plays a vital role in filament formation, concentrating in the hotter filaments and providing the higher Joule heating required to overcome pdV cooling associated with plume expansion. Conversely, comparing Figs. 6d,e, the regions outside the hot spot have *cooled* from t=115 to 122.

As the plasma plume expands, the filament continues to lengthen axially, while the striation in the metal continues to widen and deepen, through **j** redistribution. Hence, the striation and filament form of ETI coexist simultaneously. By t=125 ns, the explosion generated by the overheated striation has left behind a crater $\sim$ 10X the size of the original RI (see Fig. 7c,d), important for later MRT development. Furthermore, the plume spans the axial extent of the simulation domain, and owing to the periodic boundary conditions, **j** reconnects through axially neighboring plumes. At this point, **j** carried in the plume increases sharply (although the fraction of total current carried by the filament remains $< 1\%$), and the resulting Joule heating boosts T in the filaments (compare Fig. 7b and Fig. 6e). In Fig. 7e simulated visible emission shows a bright, vertical filament, in qualitative

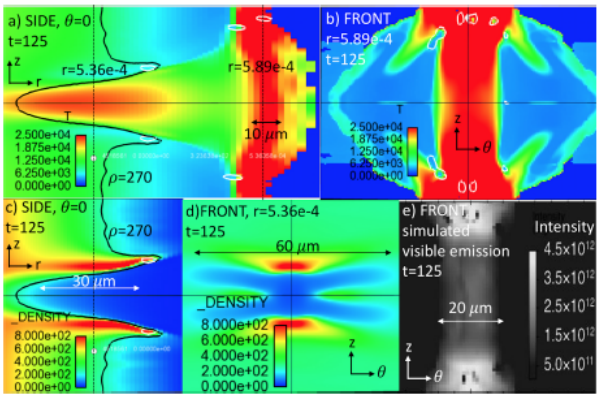

FIG. 7: **j** reconnection through filament at t=125. a-b) visualize the filament from side and front view, respectively. c)-d) visualize the striation-generated crater from side and front. e) simulated visible emission

agreement with experiment (see Fig. 3 in Ref. [29]). Later-time filament dynamics requires radiative losses, not treated in these simulations.

An equivalent 1D simulation, using the same radial resolution as 3D, also demonstrates plasma formation. However, because 1D cannot resolve the enhanced ηj^2 in the filament, the expanding vapor cools more and traverses a different path in EOS space. Consequently, as will be discussed in Ref. [23], in 1D simulations, plasma forms ∼25 ns later than 3D.

The sequence of events described heavily relies on EOS and conductivity tables, emphasizing the need for high-resolution experimental data. We are currently validating these simulations against experiments using ultrapure (i.e. essentially devoid of RI) rods, with pre-machined, large-scale (and thus more easily diagnosable) perturbations. These experiments, which will be described in a future paper, serve as both a strict constraint on material property tables, as well as an extension of our analysis into the *interaction* between multiple perturbations.

Acknowledgments

We benefitted from stimulating discussion with A.Velikovich, D. Ryutov, N. Fisch, J. Chittenden, M. Desjarlais, M. Haines (deceased), D. Yager-Elorriaga, G. Shipley, K. Tomlinson, F. Doss, and R. Vesey. We thank A.C. Robinson for Alegra guidance and I. Golovkin for help with Spect3D. Sandia National Laboratories is a multimission laboratory managed and operated by National Technology and Engineering Solutions of Sandia LLC, a wholly owned subsidiary of Honeywell International Inc. for the U.S. Department of Energy's National Nuclear Security Administration under contract DE-NA0003525.

[1] S. A. Slutz, M. C. Herrmann, R. A. Vesey, A. B. Sefkow, D. B. Sinars, D. C. Rovang, K. J. Peterson, and M. E. Cuneo, Phys. Plasmas **17**, 056303 (2010).
[2] M. R. Gomez, S. A. Slutz, A. B. Sefkow, D. B. Sinars, K. D. Hahn, S. B. Hansen, E. C. Harding, P. F. Knapp, P. F. Schmit, C. A. Jennings, T. J. Awe, M. Geissel, D. C. Rovang, G. A. Chandler, G. W. Cooper, M. E. Cuneo, A. J. Harvey-Thompson, M. C. Herrmann, M. H. Hess, O. Johns, D. C. Lamppa, M. R. Martin, R. D. McBride, K. J. Peterson, J. L. Porter, G. K. Robertson, G. A. Rochau, C. L. Ruiz, M. E. Savage, I. C. Smith, W. A. Stygar, and R. A. Vesey, Phys. Rev. Lett. **113**, 155003 (2014).
[3] A. B. Sefkow, S. A. Slutz, J. M. Koning, M. M. Marinak, K. J. Peterson, D. B. Sinars, and R. A. Vesey, Phys. Plasmas **21**, 072711 (2014).
[4] I. R. Lindemuth, Phys. Plasmas **22**, 122712 (2015).
[5] V. Mokhov, O. Burenkov, A. Buyko, S. Garanin, S. Kuznetsov, V. Mamyshev, A. Startsev, and V. Yakubov, Fusion Eng. Des. **70**, 35 (2004).
[6] A. Hubbard, C. P. McNally, and M. M. Low, Astrophysical Journal **761**, 58 (2012).
[7] S. A. Chaikovsky, V. I. Oreshkin, I. M. Datsko, N. A. Labetskaya, D. V. Rybka, and N. A. Ratakhin, Phys. Plasmas **22**, 112704 (2015).
[8] M. G. Haines, J. Plasma Physics **12**, 1 (1974).
[9] D. D. Ryutov, M. S. Derzon, and M. K. Matzen, Rev. Modern Physics **72**, 167 (2000).
[10] V. I. Oreshkin, Phys. Plasmas **15**, 092103 (2008).
[11] K. J. Peterson, D. B. Sinars, E. P. Yu, M. C. Herrmann, M. E. Cuneo, S. A. Slutz, I. C. Smith, B. W. Atherton, M. D. Knudson, and C. Nakhleh, Phys. Plasmas **19**, 092701 (2012).
[12] J. D. Pecover and J. P. Chittenden, Phys. Plasmas **22**, 102701 (2015).
[13] T. M. Hutchinson, T. J. Awe, B. S. Bauer, K. C. Yates, E. P. Yu, W. G. Yelton, and S. Fuelling, Phys. Rev. E **97**, 053208 (2018).
[14] A. M. Steiner, P. C. Campbell, D. A. Yager-Elorriaga, N. M. Jordan, R. D. McBride, Y. Y. Lau, and R. M. Gilgenbach, IEEE Trans. Plasma Sci. **46**, 3753 (2018).
[15] T. Sjostrom, S. Crockett, and S. Rudin, Phys. Rev. B **94**, 144101 (2016).
[16] E. M. Waisman, M. P. Desjarlais, and M. E. Cuneo, Phys. Rev. ST Accel. Beams **22**, 030402 (2019).
[17] N. D. Hamlin and C. E. Seyler, Phys. Plasmas **25**, 102705 (2018).
[18] V. I. Oreshkin and S. A. Chaikovsky, Phys. Plasmas **19**, 022706 (2012).
[19] E. G. Harris, Phys. Fluids **5**, 1057 (1962).
[20] S. M. Ponomarev, U.S.S.R. Comput. Maths. Math. Phys. **28**, 177 (1988).
[21] R. D. McBride, S. A. Slutz, C. A. Jennings, D. B. Sinars, M. E. Cuneo, M. C. Herrmann, R. W. Lemke, M. R.

Martin, R. A. Vesey, K. J. Peterson, A. B. Sefkow, C. Nakhleh, B. E. Blue, K. Killebrew, D. Schroen, T. J. Rogers, A. Laspe, M. R. Lopez, I. C. Smith, B. W. Atherton, M. Savage, W. A. Stygar, and J. L. Porter, Phys. Rev. Lett. **109**, 135004 (2012).
[22] I. R. Lindemuth, R. E. Siemon, B. S. Bauer, M. A. Angelova, and W. L. Atchison, Phys. Rev. Lett. **105**, 195004 (2010).
[23] E. P. Yu, manuscript in preparation for Phys. Plasmas.
[24] D. B. Sinars, manuscript in preparation for Phys. Plasmas.
[25] H. Lamb, *Hydrodynamics, Sixth Edition* (Dover, New York, 1932), 65.
[26] D. B. Sinars, S. A. Slutz, M. C. Herrmann, R. D. McBride, M. E. Cuneo, C. A. Jennings, J. P. Chittenden, A. L. Velikovich, K. J. Peterson, R. A. Vesey, C. Nakhleh, E. M. Waisman, B. E. Blue, K. Killebrew, D. Schroen, K. Tomlinson, A. D. Edens, M. R. Lopez, I. C. Smith, J. Shores, V. Bigman, G. R. Bennett, B. W. Atherton, M. Savage, W. A. Stygar, G. T. Leifeste, and J. L. Porter, Phys. Plasmas **18**, 056301 (2011).
[27] O. Schnitzer, Phys. Plasmas **21**, 082306 (2014).
[28] R. L. Panton, *Incompressible Flow, Third Edition* (Wiley, New York, 2005).
[29] T. J. Awe, E. P. Yu, K. C. Yates, W. G. Yelton, B. S. Bauer, T. M. Hutchinson, S. Fuelling, and B. B. McKenzie, IEEE Trans. Plasma Sci. **45**, 584 (2017).
[30] See Supplemental Material at $\langle \mathrm{http://\cdots} \rangle$ for the derivations and formulas not included in the main text.
[31] A. C. Robinson and C. J. Garasi, Computer Physics Communications **164**, 408 (2004).
[32] M. P. Desjarlais, J. D. Kress, and L. A. Collins, Phys. Rev. E **66**, 025401(R) (2002).
[33] S. F. Garanin, and S. D. Kuznetsov, J. Appl. Phys. **123**, 133301 (2018).
[34] L. M. Milne-Thomson, *Theoretical Hydrodynamics* (Dover, New York, 1968).
[35] J. J. McFarlane, I. E. Golovkin, P. Wang, P. R. Woodruff, and N. A. Pereyra, High Energy Density Physics **3**, 181 (2007).
[36] H. Knoepfel, *Pulsed High Magnetic Fields* (North-Holland Publishing Company, Amsterdam, 1970).
[37] W. Walters, *Fundamentals of Shaped Charges* (CMC Press, Baltimore, MD, 1998).

This paper describes objective technical results and analysis. Any subjective views or opinions that might be expressed in the paper do not necessarily represent the views of the U.S. Department of Energy or the United States Government

DISTRIBUTION

Email—Internal

Name	Org.	Sandia Email Address
Daniel Sinars	1600	dbsinar@sandia.gov
Michael E. Cuneo	1650	mecuneo@sandia.gov
Mark L. Kiefer	1651	mlkiefe@sandia.gov
Kyle Peterson	1655	kpeters@sandia.gov
Gregory A. Rochau	1680	garocha@sandia.gov
Thomas Mattsson	1684	trmatts@sandia.gov
Brent M. Jones	1688	bmjones@sandia.gov
Edward A. Weinbrecht	1692	eaweinb@sandia.gov
Technical Library	01177	libref@sandia.gov

This page left blank

This page left blank

*tjawe@sandia.gov

[i] E. G. Harris, Phys. Fluids 5, 1057 (1962).
[ii] Y. Y. Lau, J. C. Zier, I. M. Rittersdorf, M. R. Weis, and R. M.Gilgenbach, Phys. Rev. E 83, 066405 (2011).
[iii] S. A. Slutz, M. C. Herrmann, R. A. Vesey, A. B. Sefkow, D. B. Sinars, D. C. Rovang, K. J. Peterson, and M. E. Cuneo, Phys. Plasmas 17, 056303 (2010).
[iv] S. A. Slutz and R. A. Vesey, Phys. Rev. Lett. 108, 025003 (2012).
[v] M. E. Cuneo, M. C. Herrmann, D. B. Sinars, S. A. Slutz, W. A. Stygar, R. A. Vesey, A. B. Sefkow, G. A. Rochau, G. A. Chandler, J. E. Bailey, J. L. Porter, R. D. McBride, D. C. Rovang, M. G. Mazarakis, E. P. Yu, D. C. Lamppa, K. J. Peterson, C. Nakhleh, S. B. Hansen, A. J. Lopez, M. E. Savage, C. A. Jennings, M. R. Martin, R. W. Lemke, B. W. Atherton, I. C. Smith, P. K. Rambo, M. Jones, M. R. Lopez, P. J. Christenson, M. A. Sweeney, B. Jones, L. A. McPherson, E. Harding, M. R. Gomez, P. F. Knapp, T. J. Awe, R. J. Leeper, C. L. Ruiz, G. W. Cooper, K. D. Hahn, J. McKenney, A. C. Owen, G. R. McKee, G. T. Leifeste, D. J. Ampleford, E. M. Waisman, A. Harvey-Thompson, R. J. Kaye, M. H. Hess, S. E. Rosenthal, and M. K. Matzen, IEEE Trans. Plasma Sci. 40, 3222 (2012).
[vi] A.B.Sefkow, S.A. Slutz, J.M. Koning, M.M. Marinak, K.J. Peterson, D.B. Sinars, and R.A. Vesey, Phys. Plasmas **21**, 072711 (2014).
[vii] M. R. Gomez *et al*. Phys. Rev. Lett. **113**, 155003 (2014).
[viii] D.B. Sinars, *et al*. Phys. Plasmas **18**, 056301 (2011).
[ix] R. D. McBride *et al.*, Phys. Rev. Lett. **109**, 135004 (2012).
[x] R. D. McBride, M. R. Martin, R. W. Lemke, J. B. Greenly, C. A. Jennings, D. C. Rovang, D. B. Sinars, M. E. Cuneo, M. C. Herrmann, S. A. Slutz, C. W. Nakhleh, D. D. Ryutov, J.-P. Davis, D. G. Flicker, B. E. Blue, K. Tomlinson, D. Schroen, R. M. Stamm, G. E. Smith, J. K. Moore, T. J. Rogers, G. K. Robertson, R. J. Kamm, I. C. Smith, M. Savage, W. A. Stygar, G. A. Rochau, M. Jones, M. R. Lopez, J. L. Porter, and M. K. Matzen, Phys. Plasmas **20**, 056309 (2013).
[xi] K.J. Peterson, T.J. Awe, E.P. Yu, D.B. Sinars, E.S. Field, M.E. Cuneo, M.C. Herrmann, M. Savage, D. Schroen, K. Tomlinson, and C. Nakhleh, Phys. Rev. Lett. **112**, 135002 (2014)
[xii] T.J. Awe, K.J. Peterson, E.P. Yu, R.D. McBride, D.B. Sinars, M.R. Gomez, C.A. Jennings, M.R. Martin, S.E. Rosenthal, D.G. Schroen, A.B. Sefkow, S.A. Slutz, K. Tomlinson, R.A. Vesey, Phys. Rev. Lett. **116**, 065001 (2016).
[xiii] D. Ryutov,M. Derzon, and M. Matzen, Rev. Mod. Phys. 72, 167 (2000).
[xiv] K. J. Peterson, D. B. Sinars, E. P. Yu,M. C. Herrmann, M. E. Cuneo, S. A. Slutz, I. C. Smith, B.W. Atherton, M. D.
Knudson, and C. Nakhleh, Phys. Plasmas 19, 092701 (2012).
[xv] V. Oreshkin, R. Baksht, N. Ratakhin, A. Shishlov, K. Khishchenko, P. Levashov, and I. Beilis, Phys. Plasmas 11, 4771 (2004).
[xvi] V. Oreshkin, Tech. Phys. Lett. 35, 36 (2009).
[xvii] V. I. Oreshkin, Phys. Plasmas 15, 092103 (2008).
[xviii] A. G. Rousskikh, V. I. Oreshkin, S. A. Chaikovsky, N. A. Labetskaya, A. V. Shishlov, I. I. Beilis, and R. B. Baksht, Phys. Plasmas 15, 102706 (2008).
[xix] K. J. Peterson, E. P. Yu, D. B. Sinars, M. E. Cuneo, S. A. Slutz, J. M. Koning, M. M. Marinak, C. Nakhleh, and M. C. Herrmann, Phys. Plasmas 20, 056305 (2013).
[xx] J.D. Pecover and J.P. Chittenden, Phys. Plasmas **22**, 102701 (2015).
[xxi] K. J. Peterson, D. B. Sinars, E. P. Yu,M. C. Herrmann, M. E. Cuneo, S. A. Slutz, I. C. Smith, B.W. Atherton, M. D.
Knudson, and C. Nakhleh, Phys. Plasmas 19, 092701 (2012).
[xxii] T.M. Hutchinson, T.J. Awe, B.S. Bauer, K.C. Yates, E.P. Yu, W.G. Yelton, and S. Fuelling, Phys. Rev. E **97**, 053208 (2018).
[xxiii] T. J. Awe, E. P. Yu, K. C. Yates, W. G. Yelton, B. S. Bauer, T. M. Hutchinson, S. Fuelling, and B. B. McKenzie, IEEE Trans. Plasma Sci. 45, 584 (2017).
[xxiv] A. C. Robinson, *et al*., in Proceedings of the 46th AIAA Aerospace Sciences Meeting and Exhibit, Reno, NV, 7–10 January 2008, Paper No. AIAA-2008-1235, see http://arc.aiaa.org/doi/abs/10.2514/6.2008-1235
[xxv] K.J. Peterson, T.J. Awe, E.P. Yu, D.B. Sinars, E.S. Field, M.E. Cuneo, M.C. Herrmann, M. Savage, D. Schroen, K. Tomlinson, and C. Nakhleh, Phys. Rev. Lett. **112**, 135002 (2014)

Sandia National Laboratories is a multimission laboratory managed and operated by National Technology & Engineering Solutions of Sandia, LLC, a wholly owned subsidiary of Honeywell International Inc. for the U.S. Department of Energy's National Nuclear Security Administration under contract DE-NA0003525.

[xxvi] T.J. Awe, K.J. Peterson, E.P. Yu, R.D. McBride, D.B. Sinars, M.R. Gomez, C.A. Jennings, M.R. Martin, S.E. Rosenthal, D.G. Schroen, A.B. Sefkow, S.A. Slutz, K. Tomlinson, R.A. Vesey, Phys. Rev. Lett. **116**, 065001 (2016).
[xxvii] P. Rahimi and C.A Ward, Int. J. of Thermodynamics, **8**, 1-14 (2005).
[xxviii] D.M. Murphy and T. Koop, Q. J. R. Meteorol. Soc. **131**, 1539-1565 (2005).
[xxix] B.J. Kim and E. Meng. Polymers for Adv. Tech. **2016**, 27 564–576 (2015).
[xxx] R. Castaneda and J. Garcia-Sucerquia, Applied Optics **57**, A12 (2018).
[xxxi] G. Hass, J. of the Optical Soc. of America. **39**, 532 (1949).
[xxxii] http://gwyddion.net/
[xxxiii] V. I. Oreshkin, Phys. Plasmas 15, 092103 (2008).
[xxxiv] D. Ryutov,M. Derzon, and M. Matzen, Rev. Mod. Phys. **72**, 167 (2000).

[xxxv] K. J. Peterson, D. B. Sinars, E. P. Yu,M. C. Herrmann, M. E. Cuneo, S. A. Slutz, I. C. Smith, B.W. Atherton, M. D. Knudson, and C. Nakhleh, Phys. Plasmas 19, 092701 (2012).

[xxxvi] V. Oreshkin, R. Baksht, N. Ratakhin, A. Shishlov, K. Khishchenko, P. Levashov, and I. Beilis, Phys. Plasmas 11, 4771 (2004).

[xxxvii] V. Oreshkin, Tech. Phys. Lett. 35, 36 (2009).

[xxxviii] V. I. Oreshkin, Phys. Plasmas 15, 092103 (2008).

[xxxix] A. G. Rousskikh, V. I. Oreshkin, S. A. Chaikovsky, N. A. Labetskaya, A. V. Shishlov, I. I. Beilis, and R. B. Baksht, Phys. Plasmas 15, 102706 (2008).

[xl] K. J. Peterson, E. P. Yu, D. B. Sinars, M. E. Cuneo, S. A. Slutz, J. M. Koning, M. M. Marinak, C. Nakhleh, and M. C. Herrmann, Phys. Plasmas 20, 056305 (2013).

[xli] J.D. Pecover and J.P. Chittenden, Phys. Plasmas 22, 102701 (2015).

Sandia National Laboratories is a multimission laboratory managed and operated by National Technology & Engineering Solutions of Sandia LLC, a wholly owned subsidiary of Honeywell International Inc. for the U.S. Department of Energy's National Nuclear Security Administration under contract DE-NA0003525.